DISS. ETH NO. 21102

Reactive Hot Gas Filter
for Biomass Gasification

A dissertation submitted to

ETH ZURICH

for the degree of

Doctor of Sciences

presented by

Urs Rhyner

Dipl. Ing. ETH

born 30th of March 1978

citizen of Schönenberg ZH

accepted on the recommendation of

Prof. Dr. Alexander Wokaun

Prof. Dr. Javier Pérez-Ramírez

Dr. Serge M.A. Biollaz

Dr. Tilman J. Schildhauer

2013

for Anja

Acknowledgements

II

Summary

Renewable energies are supposed to cover a substantial part of the future energy supply. Efficient biomass conversion processes have to be developed regarding environmental impact and costs. An efficient and effective gas cleaning of producer gas from thermo-chemical conversion of biomass is needed to protect downstream equipment. Particulate matter, tars and contaminants reduce the performance of downstream equipment such as catalysts, internal combustion engines or gas turbines. It has been shown by process modeling, that hot gas cleaning (HGC) as compared to cold gas cleaning (scrubbers) allows significant efficiency improvements by avoiding cooling and reheating of the producer gas [1]. Sulfur is known as poison for catalysts containing Ni, Cu, Co or Fe. The removal of sulfur species is therefore crucial for any process applying catalysts such as methanation, liquid fuel synthesis or fuel cells.

A hot gas cleaning process is suggested including a hot gas filter (HGF) unit and a catalytic reformer to decompose sulfur containing hydrocarbons. Preconditions for the HGC process as suggested in this study are a stable operation of a hot gas filter with ash and soot from biomass gasification and the decomposition of sulfur containing hydrocarbons to H_2S by a catalytic reformer enabling a desulfurization by state of the art sorption materials.

Hot gas cleaning technologies are essential to increase the efficiency of biomass conversion systems. To prove the progress being made in hot gas filter (HGF) development, long duration tests are important. With more than 1800 h time on stream, the concept of HGF operating at 450 °C with filter elements installed in horizontal position and a coupled pressure pulse (CPP) recleaning system was proved to be working for dust produced by gasification of woody biomass. Sustainable filtration could be demonstrated regarding pressure drop over the filter candle wall and filter end for more than 1000 h.

Dynamic pressure measurements are introduced as powerful tool to detect filter failures at early stage. Filter failures such as leakages, blockages and permeability reductions can be detected during back pressure recleaning pulses. High frequency sensors enable the recording of the recleaning pulse. Patchy cleaning and depth filtration can be detected much faster with dynamic pressure measurements than with conventional differential pressure measurements. Parameters derived from dynamic pressure data were monitored over time and compared with refer-

ence data to detect filter failures. The method of dynamic pressure measurements complements conventional pressure difference measurements.

One of the final goals is an HGF operating at 850 °C which enables the filtration of product gases at exit temperatures of e.g. allothermal gasifiers. The application of CPP recleaning systems permits the filtration of sticky dusts at stable conditions as shown in this report. The good results of these studies confirm the potential of this filter design and therefore a next generation HGF is planned operating at 850 °C.

A physical model describing the pressure evolvement in different filter sectors during back pressure pulses generated by coupled pressure pulse (CPP) technology was developed. The CPP recleaning model was developed based on mass conservation, steady state assumptions and ideal gas conditions. Knowing the volumes of the filter sectors, pressures can be determined according to the calculated gas flows and gas accumulations. Model and experimental results were compared showing an average model accuracy of 93 % for pressure maxima measured in the recleaning sector. Experiments were conducted with grain ceramic filter elements at ambient temperature and at 450 °C. Flush tank pressures varied between 250 hPa and 1000 hPa. The model was kept as generic as possible allowing the modeling of different CPP filter set-ups and calculations for scale-up considerations. The model capabilities to reproduce pressure evolvements depending on different filter materials and filter end configurations were tested. Comparing model results of new filters with operational data of used filter elements allows recognizing filter failures such as leakages, permeability reduction and blockages.

The simulation results of the CPP recleaning model showed that the model is a valuable tool that is able to support up-scaling and filter design considerations of CPP HGF systems. An overall accuracy of 93 % for model results compared with experimental results allows the dimensioning of a HGF. Deviations of the pressure maximum in the recleaning sector by 10 % can be compensated without high financial impacts e.g. by adjusting the pressure in the flush tank, the valve opening time or the size of the dynamic pressure switch.

A 400 cpsi noble metal catalyst was used to test the conversion of tars and sulfur containing hydrocarbons in the presence of steam, hydrogen sulfide and ethene. In order to reproduce producer gas from biomass gasification, higher molecular hydrocarbons (toluene, naphthalene, phenanthrene, pyrene) and sulfur containing hydrocarbons (thiophene, benzothiophene, dibenzothiophene) were added to a syngas. The syngas consisted of H_2, CH_4, H_2O, CO, CO_2 and N_2. The catalyst was

operated at temperatures between 620 °C and 750 °C and at gas hourly space velocity (GHSV) of 9'000 h^{-1} and 18'000 h^{-1}.

Conversions of sulfur containing hydrocarbons (41 % to 99.6 %) were on average higher than conversions of sulfur free tars (0 % to 47 %). High temperature, low GHSV, low steam and sulfur content favored high conversions of tars and sulfur tars. As the catalyst was able to decompose sulfur tars under operating conditions close to a real wood gasification plant, it is possible to use it for hot gas cleaning in any process that includes sulfur sensitive catalysts such as fuel cells, liquid fuel synthesis or methanation processes. In such processes, H_2S produced by the reforming catalyst from sulfur tars can be captured downstream of the reformer in a metal oxide bed such as ZnO.

Based on the experimental results, parameters estimation was conducted to determine activation energies, heat of adsorption and pre-exponential factors. Applied kinetics for the commercially available noble metal catalyst could be established. First order kinetics could be developed for tars and sulfur tars as well as for ethene. The formation of ethane and benzene was assumed to be at constant rate depending on the decomposition of ethene and toluene respectively. Reaction rate laws of steam reforming of methane and water gas shift could be determined including equilibrium term and adsorption of sulfur. Simulation results at operating temperatures of 850 °C showed higher conversions rates for sulfur free tars, ethene and methane while the temperature dependence of sulfur tars was limited.

A reactive hot gas filter is the integration of a catalytic reformer into the HGF vessel and the combination with sorption materials applied upstream or in the HGF. Simulation results of the catalyst were used to evaluate different possibilities regarding the integration of catalytic material into HGF units with vertical and horizontal filter design. The options of catalytic active filter elements, additional catalytic foam at the inside of the filter element and a monolith at the exit of the filter vessel are feasible assuming the same catalyst material as applied in the reforming catalyst used in this study. These three options can be applied independently of the horizontal or vertical filter design.

Zusammenfassung

Erneuerbare Energien sollen einen substantiellen Anteil der zukünftigen Energieversorgung ausmachen. Um dieses Ziel zu erreichen, müssen effizienten Verfahren zur energetischen Biomassenutzung bezüglich Umweltbelastung und Kosten entwickelt werden. Eine effiziente und effektive Gasreinigung von Produktgas aus thermochemischen Umwandlungsprozessen von Biomasse wird benötigt, um nachgeschaltete Prozesseinheiten zu schützen. Staub, Teere und andere Verunreinigungen reduzieren die Leistung von nachgeschalteten Prozesseinheiten, wie Katalysatoren, Verbrennungsmotoren oder Gasturbinen. Prozessmodellierungen haben gezeigt, dass die heisse Gasreinigung im Vergleich zur kalten Gasreinigung (Wäscher) signifikante Effizienzsteigerungen ermöglicht, weil das Abkühlen und wieder Aufheizen des Produktgases vermieden werden kann [1]. Schwefel ist ein bekanntes Gift für Katalysatoren, welche Ni, Cu, Co oder Fe enthalten. Das Entfernen von Schwefelspezies vom Produktgas ist deshalb sehr wichtig für Prozesse, welche schwefelempfindliche Katalysatoren verwenden, wie die Methanisierung, die Synthese von flüssigen Treibstoffen oder Brennstoffzellen.

Ein Heissgasreinigungsprozess wird vorgeschlagen bestehend aus einem Heissgasfilter (HGF) und einem katalytischen Reformer für den Abbau von schwefelhaltigen Kohlenwasserstoffen. Voraussetzungen für den Heissgasreinigungsprozess, wie er in dieser Studie vorgeschlagen wird, sind ein stabiler Betrieb eines Heissgasfilters mit Asche und Russ aus einer Biomassevergasungsanlage und der Abbau von schwefelhaltigen Kohlenwasserstoffen zu H_2S mittels eines katalytischen Reformers, um die Entschweflung mit einem konventionellen Sorptionsmittel zu ermöglichen.

Heissgasreinigungstechnologien sind wesentlich für die Effizienzsteigerung der Umwandlung von Biomasse zu anderen Energieträgern. Um die Fortschritte in der Heissgasfilterentwicklung aufzuzeigen, sind Langzeitversuche von grosser Bedeutung. Mit mehr als 1800 h Betrieb mit Staub von Produktgas aus der Vergasung von Holz, konnte die Funktionstauglichkeit eines Heissgasfilters mit angekoppelter Druckimpulsabreinigung (CPP) bewiesen werden, welcher bei 450 °C und mit horizontal installierten Filterkerzen betrieben wurde. Stabiler Filterbetrieb, bezogen auf den Druckabfall über die Filterkerzenwand und das Filterende, konnte für mehr als 1000 h gezeigt werden.

Dynamische Druckmessungen wurden als leistungsfähiges Hilfsmittel zur frühzeitigen Detektion von Filterversagen vorgestellt. Filterversagen, wie Leckagen, Blo-

ckaden und Permeabilitätsreduktionen, können während Druckimpulsabreinigungen detektiert werden. Hochauflösende Drucksensoren ermöglichen das Aufzeichnen von Druckimpulsen. Unvollständige Filterflächenabreinigung (patchy cleaning) und Tiefenfiltration können schneller erkannt werden mit dynamischen Druckmessungen als mit standardmässigen Druckdifferenzmessungen. Von dynamischen Druckmessungen abgeleitete Parameter werden über die Zeit aufgezeichnet und mit Referenzdaten verglichen, um Filterversagen aufzudecken. Die Methode der dynamischen Druckmessungen ergänzt konventionelle Druckdifferenzmessungen.

Eines der Endziele ist ein Heissgasfilter, welcher bei 850 °C betrieben werden kann, was die Filtration von Produktgas bei Ausgangstemperaturen von z.B. allothermen Vergasern ermöglicht. Der Einsatz der angekoppelten Druckimpulsabreinigung (CPP) ermöglicht die stabile Filtration von klebrigen Stäuben, wie in diesem Bericht aufgezeigt wird. Die vielversprechenden Resultate dieser Studie bestätigen das Potential dieses Filteraufbaus. Aus diesem Grund wird ein weiterer Heissgasfilter geplant, welcher bei 850 C betrieben werden kann.

Ein physikalisches Modell wurde entwickelt zur Beschreibung von angekoppelter Druckimpulsabreininung (CPP) generierten Druckverläufen in verschiedenen Filtersektoren. Das Modell der Druckverläufe, generiert von angekoppelter Druckimpulsabreinigung, wurde entwickelt, basierend auf dem Prinzip der Massenerhaltung, dem Vorhandensein von stationären Zuständen und dem idealen Gasgesetz. Wenn die Volumen der Filtersektoren bekannt sind, können die entsprechenden Drücke anhand der Gasflüsse und Gasakkumulierungen berechnet werden. Modell- und Versuchsdaten wurden verglichen, wobei eine durchschnittliche Genauigkeit von 93 %, bezogen auf die maximalen Drücke im Abreinigungssektor, bestimmt werden konnte. Versuche wurden mit kornkeramischen Filterelementen bei Raumtemperatur und bei 450 °C durchgeführt. Der Abreinigungsdruck variierte zwischen 250 hPa und 1000 hPa. Das Modell wurde so allgemeingültig wie möglich gehalten, damit Modellierungen von verschiedenen Filteraufbauten mit angekoppelter Druckimpulsabreinigung und Berechnungen zur Hochskalierung von solchen Filtern gemacht werden können. Die Fähigkeit des Modells Druckverläufe, abhängig von verschiedenen Filtermaterialien und Filterabschlüssen, korrekt wiederzugeben wurde getestet. Den Vergleich von Modelldaten von neuen Filterkerzen mit Versuchsdaten von gebrauchten Filterkerzen erlaubt das Erkennen von Filterversagen wie Leckagen, Blockaden und reduzierter Permeabilität.

Simulationen mit dem Filtermodell haben gezeigt, dass das Modell ein wertvolles Instrument ist für die Unterstützung von Hockskalierungs- und Filteraufbauüberle-

gungen von Heissgasfiltern mit angekoppelter Druckimpulsabreinigung. Eine durchschnittliche Genauigkeit von 93 % des Filtermodells im Vergleich mit Versuchsdaten erlaubt eine gute Dimensionierung eines Heissgasfilters. Abweichungen des Druckmaximums im Abreinigungssektor von 10 % können kompensiert werden ohne grosse finanzielle Folgen, z.B. durch Anpassen des Abreinigungsdruckes, der Ventilöffnungszeit oder der Grösse des dynamischen Druckschalters.

Ein 400 cpsi Edelmetallkatalysator wurde verwendet, um den Umsatz von Teeren und schwefelhaltigen Kohlenwasserstoffen in Anwesenheit von Dampf, Schwefelwasserstoff und Ethen zu bestimmen. Um Produktgas aus der Biomassevergasung zu reproduzieren, wurden höhermolekulare Kohlenwasserstoffe (Toluol, Naphthalin, Phenanthren, Pyren) und schwefelhaltige Kohlenwasserstoffe (Thiophen, Benzothiophen, Dibenzothiophen) einem Synthesegas beigemischt. Das Synthesegas bestand aus H_2, CH_4, H_2O, CO, CO_2 und N_2. Der Katalysator wurde bei Temperaturen zwischen 620 °C und 750 °C betrieben und bei Raumgeschwindigkeiten (gas hourly space velocity, GHSV) von 9'000 h^{-1} und 18'000 h^{-1}.

Umsätze von schwefelhaltigen Kohlenwasserstoffen (41 % bis 99.6 %) waren im Durchschnitt höher als die Umsätze von schwefelfreien Teeren (0 % to 47 %). Hohe Temperaturen, tiefe GHSV, tiefer Dampf- und Schwefelgehalt bewirkten hohe Umsätze von schwefelhaltigen und schwefelfreien Teeren. Der Katalysator kann unter Betriebsbedingungen, die vergleichbar sind mit jenen von richtigen Holzvergaseranlagen, schwefelhaltige Teere abbauen. Daher kann er für die Heissgasreinigung in Prozessketten mit schwefelsensitiven Katalysatoren, wie Brennstoffzellen, Methanisierung oder Synthese von Flüssigtreibstoffen eingesetzt werden. In solchen Prozessketten kann Schwefelwasserstoff, welcher vom Reformerkatalysator aus schwefelhaltigen Teeren erzeugt wurde, mit einem dem Reformerkatalysator nachgeschalteten, metalloxidischen Festbett (z.B. ZnO) abgeschieden werden.

Basierend auf den Versuchsdaten wurde eine Parameterschätzung durchgeführt, um Aktivierungsenergien, Adsorptionsenthalpien und Vorfaktoren für den kommerziell erhältlichen Edelmetallkatalysator zu bestimmen. Eine Kinetik erster Ordnung konnte für schwefelhaltige und schwefelfreie Teere und für Ethen formuliert werden. Die Bildung von Ethan und Benzol wurde als proportional zur Abbaurate von Ethen, respektive Toluol, angenommen. Für die Dampfreformierung von Methan und der Wassergas-Shift-Reaktion konnten Reaktionsgeschwindigkeitsgesetze gemäss einem Langmuir-Hinshelwood-Ansatz bestimmt werden inklusive Gleichgewichtsterm und Schwefeladsorptionsterm. Die auf dieser Gebrauchskinetik basierende Simulation eines Monolithen bei Betriebstemperaturen von 850 °C

zeige höhere Umsätze für schwefelfreie Teere, Ethen und Methan, während die Temperaturabhängigkeit von schwefelhaltigen Teeren gering war.

Ein reaktiver Heissgasfilter entspricht der Integration eines Reformerkatalysators im Filtergehäuse kombiniert mit Sorptionsmittel, welche dem Heissgasfilter vorgeschaltet dazugegeben werden. Die Resultate von Simulationen des Reformerkatalysators wurden verwendet, um verschiedene Integrationsmöglichkeiten des Katalysatormaterials in Heissgasfilter mit horizontal oder vertikal installierten Filterkerzen zu prüfen. Technisch machbare Integrationsmöglichkeiten sind katalytisch aktive Filterkerzen, zusätzliche Schaumzylinder angebracht im inneren der Filterkerzen und ein Monolith am Ausgang des Filtergehäuses, angenommen dasselbe katalytisch aktive Material wird verwendet wie für den Reformerkatalysator in dieser Studie. Diese drei Optionen können unabhängig von horizontal oder vertikal installierten Filterelementen angewendet werden.

Table of content

1   Introduction

1.1   Biomass derived energy

The awareness of limited fossil resources and the impact of CO_2 emissions on global warming support investments in renewable energies. CO_2 emissions target levels are defined by sovereign states on a voluntary basis in order to limit climate change to acceptable levels. Due to a neutral CO_2 balance, biomass became an integral part of energy policies. The EU defined the 2020 target which means a 20 % reduction in greenhouse gas emissions compared to 1990 levels, 20 % reduction in primary energy use through increased energy efficiency and 20 % share of renewable energies in the overall energy mix with a minimum of 10 % of renewable energy in transportation sector, all implemented by the year 2020 [2].

The nuclear disaster of Fukushima Dai-ichi on the 11th of March 2011, when a major earthquake followed by a 15 m tsunami disabled the power supply and cooling system of three nuclear reactors, re-launched fundamental debates about risks of nuclear power plants. Driven by political initiatives and pressure from citizens, the renewable energy sector received new financial support to accelerate the increase of the share of renewable energy in the electric power production. Among other countries, both the cabinet and parliament of Switzerland decided four months after March 2011 to phase out nuclear power. In legal terms, the decision is essentially a declaration of intent. A ban on the construction of new nuclear power plants is contingent upon revising either nuclear energy legislation or the Swiss constitution. A binding legal decision is to be made in 2015. A new energy strategy 2050 is under development suggesting how to compensate for the 38 % share of electricity produced by nuclear power plants by increased energy efficiency, the expansion of hydropower and use of new renewable energy, and, where necessary, on fossil-fuel-based electricity production (combined heat and power (CHP) plants, gas-fired combined cycle power plants) and imports [3].

1.1.1   Biomass energy in Switzerland

In 2011, 19.4 % of final energy consumption of Switzerland was derived from renewable sources (including wood and hydro-power). 4.34 % out of the 19.4 % of final energy consumption was derived from biomass (wood and biogas) [4]. 56 % is the fraction of renewable energy of the electricity production in Switzerland in 2011. 54 % was produced by hydroelectric power generation and 2 % by new re-

newables. Most of the 2 % new renewables was generated by waste incineration and sewage plants. Not more than 0.26 % of the total electricity production in Switzerland was derived from wind, solar and biomass (1'600 GWh) [3]. The new energy strategy 2050 suggests a potential in electricity production of new renewables of more than 24'000 GWh by 2050 based on a study from the consultant Prognos [5]. Electricity derived from gasification of biomass is excluded from the Prognos study and therefore from the new energy strategy 2050. It is argued that the scarce biomass has to be used for the production of fuels used in the transportation sector. In 2011, 7'786 GWh of final energy was produced by wood of which 344 GWh was electricity [6].

In Swiss energy studies, generating electricity out of wood is generally referred to wood combustion combined with steam production and steam turbine. The potential of wood gasification and electricity production by gas engine, gas turbine or fuel cells is usually neglected [7, 8]. The so called "Energie-Trialog" mentions the competing energy conversion of biomass to heat, electricity and fuels and suggests a partition of 40 % of biomass for electricity production, 30 % for heat and 30 % for fuels [8].

1.1.2   High efficient energy production from biomass
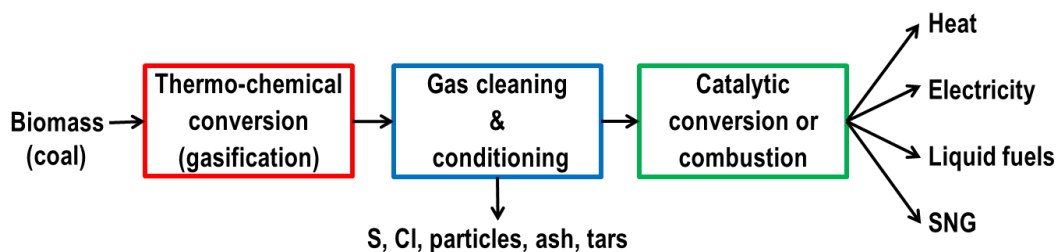
Figure 1.1:   *Generic conversion process from biomass (coal) by thermo-chemical conversion, gas cleaning and conditioning and catalytic conversion or combustion to heat, electricity, liquid fuels or SNG.*

Key energy studies predict electricity to become more relevant in the total energy mix of Switzerland by 2050 [3, 5, 7, 8]. For that reason, the high efficient electricity production of biomass integrated fuel cell (B-IGFC) systems should be considered. High temperature fuel cells e.g. solid oxide fuel cells (SOFC) in combination with biomass gasification is a promising approach to reach high electrical efficiencies. The main technical challenge is the adjustment of the three main system components thermo-chemical conversion (gasification), gas cleaning and conditioning and catalytic conversion (fuel cell or methanation). A generic conversion process from biomass or coal to energy by gasification is shown in Figure 1.1.

Figure 1.2 shows high electrical efficiencies for fuel cell and gas engine based systems for biomass inputs up to 10 MW$_{th}$. Small scale CHP plants up to 10 MW thermal biomass input would suit the decentralized structure of Switzerland. Using wood merely for heat production seems like wasting resources. Instead, producing biomass derived synthetic natural gas (bio-SNG) by methanation would enable the storage of chemical energy of wood gas helping to solve the energy storage problem. A well established distribution network for natural gas already exists in Switzerland. As needed, bio-SNG can be used as fuel in vehicles, for efficient electricity production with fuel cells or for heat production.
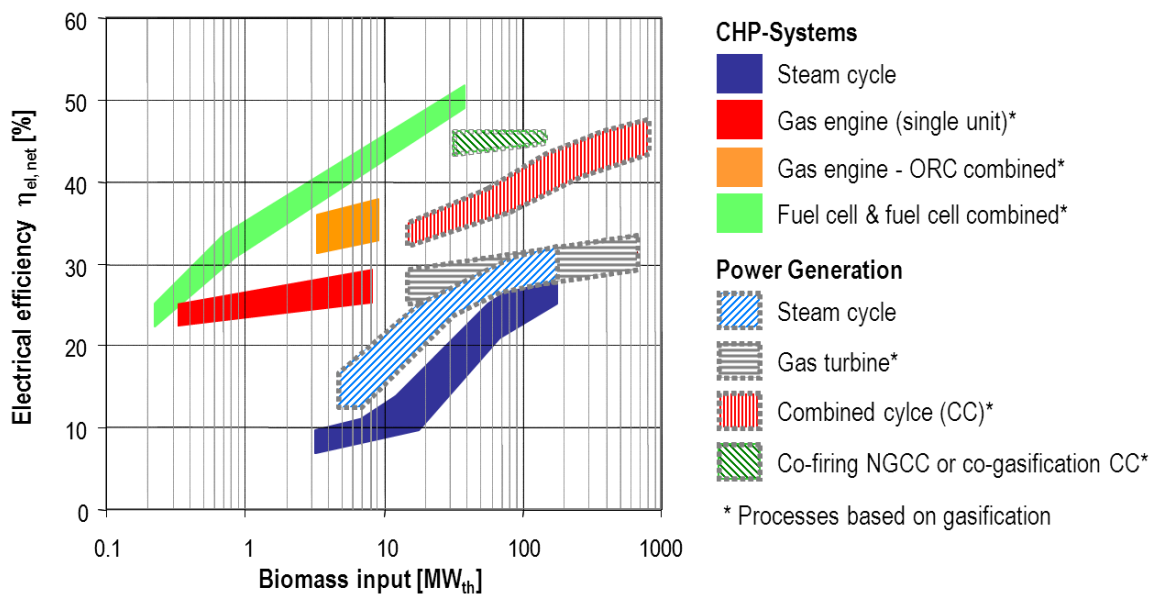
Figure 1.2: *Electrical efficiencies based on plant size for different energy conversion processes [9], ORC = organic Rankine cycle, NGCC = natural gas combined cycle, CC = combined cycle*

1.1.3   Gas cleaning of biomass derived producer gases

Thermo-chemical conversion of biomass by gasification produces mainly gases such as H_2, H_2O, CO, CO_2 and C_xH_y but also carbon rich particulate matter. Impurities such as tars, sulfur compounds, alkali-, halide-, nitrogenous compounds and trace elements are also present in biomass derived producer gases (chapter 2.3). Particulate matter, tars and contaminants reduce the performance of downstream equipment such as catalysts, internal combustion engines or turbines. Efficient and effective gas cleaning is needed to protect downstream equipment. A filtration unit is needed to separate the particulate matter from the product gas protecting downstream process units from fouling. High dust load and sticky ash particles from biomass gasification are challenging conditions for filtration units. Sulfur is known as poison for catalysts containing Ni, Cu, Co or Fe. The removal of sulfur

species is therefore crucial for any process applying catalysts such as methanation, liquid fuel synthesis or fuel cells.

Figure 1.3 shows three different cases of gas cleaning processes at different temperature levels for B-IGFC processes. The electro-chemical conversion of the producer gas to electricity by a fuel cell (SOFC) is shown as an example but the gas cleaning process is also valid for other conversion processes involving catalysts such as methanation or liquid fuel synthesis.

The low temperature case represents the state of the art gas cleaning. Exit temperatures of e.g. fluidized bed gasifiers (see chapter 2.2) can be as high as 850 °C. The low temperature gas cleaning requires cooling of the producer gas below 400 °C in order to fulfill the temperature limits of the filtration system. Downstream of the filter unit, tars and steam will condensate in quenching columns (scrubber) operated at temperatures as low as 10 °C. Sulfur species will be captured in cold absorbers such as scrubbers (e.g. Selexol, Rectisol) or in fixed beds (active carbon, metal oxide). Depending on the material used for the fixed bed desulfurization, the temperature has to be increased. Downstream of the desulfurization, steam has to be added again in case of fuel cells as conversion unit and the temperature needs to be increased again to the required gas inlet temperature of the SOFC.
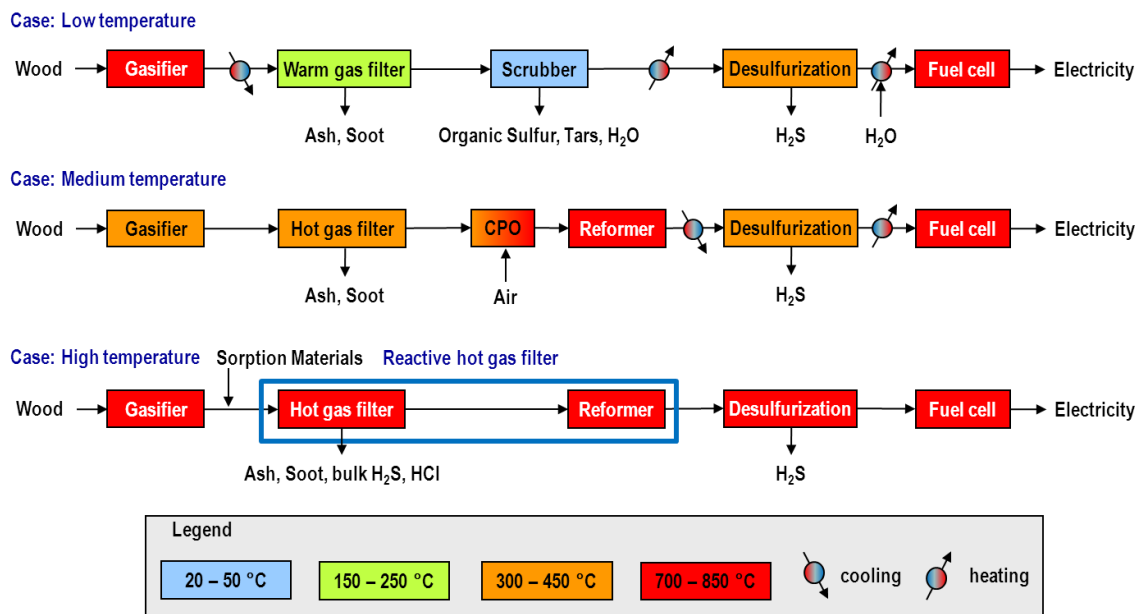
Figure 1.3: Gas cleaning process at low, medium and high temperature for B-IGFC systems or other conversion processes such as methanation of liquid fuel synthesis

The medium temperature case shows the B-IGFC process chain as implemented at Paul Scherrer Institut (PSI) at small pilot scale with a thermal input up to 12 kW (chapter 3.1). The exit temperature of e.g. an updraft gasifier can have the same

exit temperature as the HGF operating at 450 °C. Therefore a cooling of the producer gas upstream of the HGF unit is not needed. Downstream of the HGF the producer gas is heated by catalytic partial oxidation (CPO) to reach the required temperature of the reformer catalyst. A reformer catalyst can be applied to convert tars and sulfur containing hydrocarbons to lower molecular hydrocarbons, CO, CO_2, H_2, H_2O and H_2S. The desulfurization can be done by the removal of H_2S by sorption materials. If ZnO is used as sorption material, temperature has to be below 600 °C (chapter 2.7). No steam needs to be added as compared to the low temperature case because process temperatures stayed above the condensation temperature of water.

The high temperature case is the suggested process chain to be further investigated. The whole process chain operates at the exit temperature of the gasifier. No cooling or reheating of the producer gas is needed. The HGF operates at temperatures up to 850 °C. Concepts to integrate the reformer catalyst in the HGF unit, operating at the same temperature as the HGF, are presented in chapter 2.7. The integration of the reformer catalyst avoids heat losses due to the connection between the operating units. In addition, high temperature sorption materials can be applied upstream of the HGF to remove contaminants such as H_2S and HCl. The combination of sorption materials upstream of a HGF and a reformer catalyst is called reactive hot gas filter (Figure 1.4).
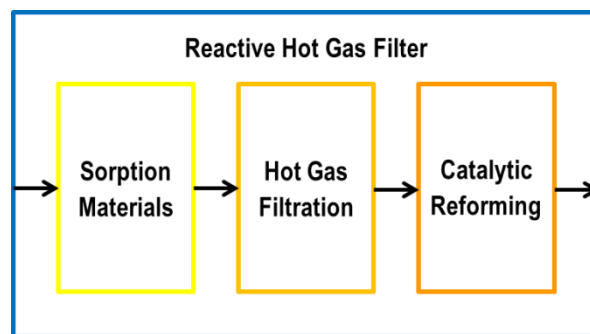
Figure 1.4: *Concept of a reactive hot gas filter combining sorption materials, hot gas filtration and catalytic reforming*

The two cases, medium and high temperature, represent hot gas cleaning (HGC) processes. The single process steps of the B-IGFC process chain are explained in chapter 2 including hot gas cleaning steps.

1.2 Motivation

Hot gas cleaning (HGC) of producer gas derived from biomass gasification is a very promising technology that offers significant efficiency gains in the conversion

process from biomass to electricity, synthetic natural gas (SNG) or liquid fuels. Reactive hot gas filtration is assumed to have the potential of an efficient and economical attractive process. It has been shown by process modeling, that HGC allows significant efficiency improvements by avoiding cooling and reheating of the producer gas [1].

Hot gas filtration temperatures stay above the condensation temperature of tars and water. This has several advantages. Processing tars above their dew points prevents fouling of equipment due to tar condensation. Because condensation in quenching columns can be avoided by HGC, depending on the gasification process, no steam needs to be added to the producer gas again. Steam content is needed downstream of the filter unit for steam reforming or to prevent soot formation in catalytic process units (e.g. fuel cell). In addition, contaminated liquid of quenching columns can be avoided which improves energy efficiency and reduces environmental impact and costs.

HGF prevents exposing heat exchangers to particle loaded producer gas because the hot gas can be filtered at exit temperatures of gasifiers. High exit temperatures of gasifiers enable the application of high temperature sorption materials upstream or inside of a hot gas filter to reduce the sulfur and alkali content of the producer gas [10]. High temperatures are needed e.g. to catalytically convert sulfur containing hydrocarbons (sulfur tars) and sulfur free tars to lower molecular hydrocarbons and H_2S. Hydrogen sulfide can be adsorbed by a fixed bed of metal oxides completing the desulfurization of the producer gas. Catalysts can be used downstream of a hot gas filter protected from particulate matter. In a dust free environment, catalyst structures, e.g. monolith channels, can be smaller allowing more compact process units.

1.3 Objectives

Investigation on a reactive HGF system consisting of HGF and catalytic reformer for process chain optimization.

- proof of concept of HGF operated at 450 °C with CPP recleaning system and horizontal filter design for gasification of biomass
- development of a physical model to simulate pressure evolvements during back pressure pulses of CPP recleaning systems

- investigation on capabilities of a reformer catalyst to decompose sulfur containing hydrocarbons under conditions as close to real producer gas derived by wood gasification as possible
- development of applied kinetics of the catalyst to be investigated supporting upscale and design considerations
- evaluation of integration possibilities of the catalytic reformer into the HGF unit

Preconditions for the HGC process as suggested in this study are a stable operation of a hot gas filter with ash and soot from biomass gasification and the decomposition of sulfur containing hydrocarbons to H_2S by a catalytic reformer enabling a desulfurization by sorption materials.

1.4 Methodology

Hot gas filter

- Conducting long duration tests with a warm gas filter operated at 450 °C with ash and soot derived from updraft wood gasifier
- Evaluating the informative value of dynamic pressure sensors during operation of the HGF
- Developing a physical CPP filter model to better understand filter condition and to optimize filter operation

Reformer catalyst

- Evaluating the catalyst capabilities to decompose tars and sulfur containing hydrocarbons
- Developing applied kinetics based on experimental results by parameter estimation and definition of reaction rate laws

Reactive hot gas filter

- Defining integration possibilities of the catalytic reformer into the HGF unit and calculating the size of the catalytic reformer based on simulation results from applied kinetics

1.5   Catalyst specifications

The catalyst was provided under conditions of confidentiality. The supplier cannot be named. The composition of the noble metal catalyst is unknown to the author and it was not allowed to be investigated. Accordingly, any catalyst specifications such as preparation, surface area, washcoat thickness, void fraction, average pore size or tortuosity are unknown.

1.6   Organization of the thesis

Chapter 2 describes the process units of a B-IGFC process chain including contaminants that are found in biomass derived producer gas. After an introduction to biomass conversion processes (chapter 2.1), the chapters are organized according to the process flow. Chapter 2.2 explains the categorization of different gasifier technologies and mentions the most important concepts. Contaminants and according removal options are listed in chapter 2.3. Sorption materials that can be applied in reactive HGF systems upstream of the HGF unit are mentioned in chapter 2.4. The longest part of chapter 2 is needed to introduce the concept of hot gas filtration in chapter 2.5. Jet pulse and CPP recleaning systems are explained, different filter designs, pressure measurement methods and the goal of the physical filter model. Chapter 2.6 gives a brief introduction to the catalytic reformer unit followed by chapter 2.7 about the H_2S polishing step which has to guarantee the desulfurization of the producer gas. The last unit in the B-IGFC process chain is the electro-chemical conversion. The concept of fuel cells and SOFC in particular is introduced in chapter 2.9

Chapter 2.7 describes integration possibilities of catalytic reformers into the HGF unit. Integration possibilities are shown for horizontal and vertical filter design. Examples of two power plants are mentioned where a CPO catalyst was placed upstream of the HGF unit in a high dust environment.

Chapter 3 covers the investigated HGF unit including the physical CPP filter model. The experimental set-up is explained and the method of dynamic pressure measurements. Long duration tests are presented and the value of dynamic pressure measurements during filter operation. The CPP filter model is introduced including comparisons of experimental and model results. Different filter simulations are presented.

Chapter 4 presents the tested reformer catalyst including set-up of the test rig and the analytical equipment. Conversion rates as determined by experimental results are presented. Derived from experimental results, applied kinetics were developed including parameter estimation, parity and residual plots. The model was used to simulate conversion rates at a temperature of 850 °C. Included in chapter 4 are the results of integration possibilities regarding reformer catalyst and HGF.

Chapter 5 concludes about the findings of the thesis and the answers regarding the objectives. Outlook and recommendations for future work are presented as well. In the annex, complementary information regarding filter and catalyst model can be found.

2 Technology overview

Chapter 2 describes the process units of a B-IGFC process chain including contaminants that are found in biomass derived producer gas. After an introduction to biomass conversion processes, the chapters are organized according to the process flow.

2.1 Energy conversion of biomass
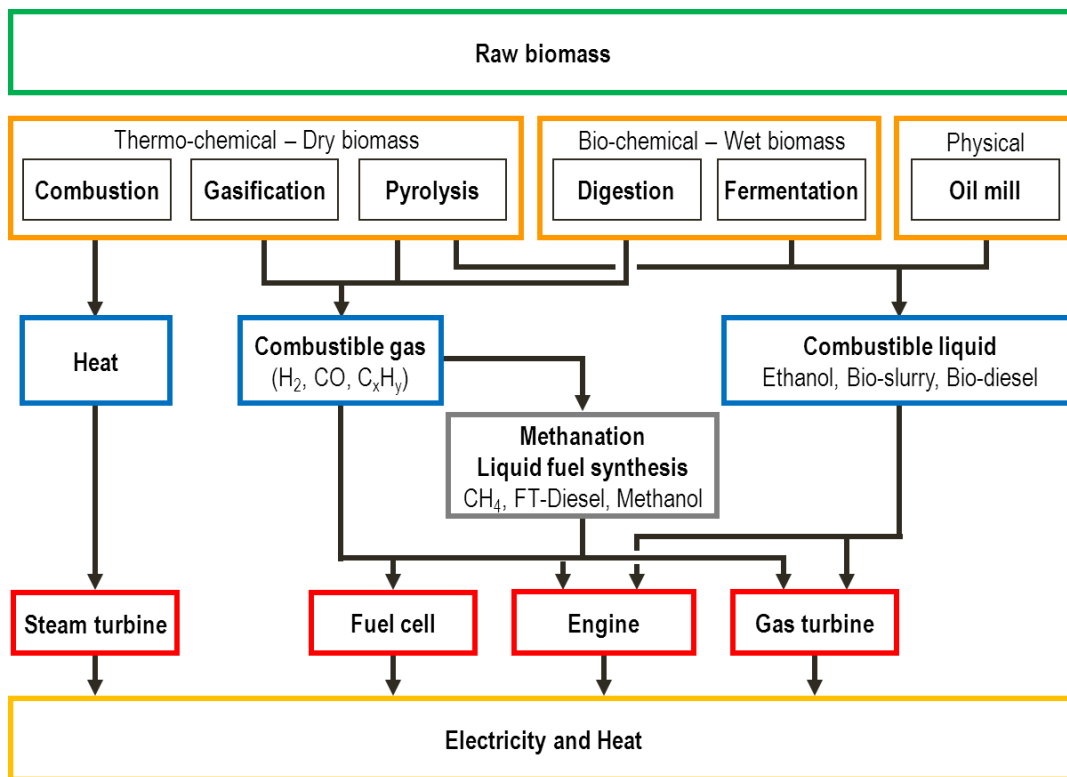
Figure 2.1: *Conversion processes from raw biomass to electricity and heat*

Different energy conversion options exist depending on the kind of biomass, the preferred intermediary product and the final conversion process. Physical extraction is used for e.g. rapeseed to produce plant oil which can be further chemically modified to produce rapeseed methyl ester (RME) also called bio-diesel. Bio-chemical conversion is used for wet biomass. Fermentation is used to produce e.g. ethanol out of sugar cane and digestion to produce methane (biogas) out of e.g. mixed manure. First generation biofuels are produced by physical and bio-chemical conversion processes.

The high content of lignin in woody biomass favors thermo-chemical conversion processes such as combustion, pyrolysis or gasification. Combustion is conducted

at temperatures of 800 °C to 1300 °C at air-to-fuel ratios higher than 1 providing oxygen at excess conditions. The combustion of wood converts the chemically bound energy to thermal energy only. Other than heat, the thermal energy can be used to produce steam which can be used to produce electricity by steam turbines. Gasification takes place at temperatures of 700 °C to 900 °C at air-to-fuel ratios below 1 producing combustible gas. Pyrolysis is conducted at temperatures between 400 °C to 700 °C at an air-to-fuel ratio of zero producing gas, char and bio-slurry depending on the pyrolysis technology applied.

After gas cleaning and conditioning, combustible gases from pyrolysis and gasification can be used for heat and electricity production by gas engines, gas turbines or fuel cells. Thermo-chemical conversion in combination with catalysts is used to produce second generation biofuels such as bio-SNG and liquid fuels. Combustible gas and liquid enable the storage and the distribution of biomass derived energy. Eq. 2.1 and Eq. 2.2 show the basic methanation and Fischer-Tropsch reactions producing methane and alkanes respectively.

$$3H_2 + CO \leftrightarrow CH_4 + H_2O \qquad -\Delta H_R = 206 \text{ kJ } mol^{-1} \qquad \text{Eq. 2.1}$$

$$(2n + 1)H_2 + nCO \rightarrow C_nH_{2n+2} + nH_2O \qquad \text{Eq. 2.2}$$
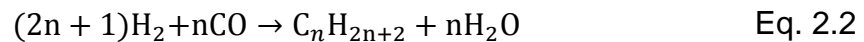
This thesis focuses on gasification of woody biomass for electricity production though other dry biomass can be used such as grass, straw and other ligneous biomass. The reactive hot gas filter, as proposed in this study, is used primarily to treat combustible gases from gasification of biomass.

2.2   Thermochemical conversion of woody biomass

Many different gasifier technologies were developed for small and big scale applications. The kind of the biomass feedstock, the required gas quality for downstream processes and the required power will lead to the preferred gasifier technology [11-13]. Categorization of gasifier technologies can be based on the arrangement of the four sub-processes drying, pyrolysis, gasification and combustion or on the way heat is provided to the system. If part of the feedstock is burned by the gasification agent, the heat is provided directly to the system (auto-thermal). Gasification agent can be air or oxygen. Additionally steam can be added to act as thermal moderator and as reactant in steam reforming processes. If the heat required for gasification is produced outside of the gasification reactor the system is heated indirectly (allothermal).

In case of allothermal gasification, the heat exchange to the gasification reactor can be conducted by hot bed material or by heat pipes. The fast internal circulating fluidized bed (FICFB) gasifier of Repotec in Güssing with a thermal input of 8 MW is an example for an allothermal gasifier where hot bed material is transferred to the gasification reactor [15]. The heat pipe reformers (HPR) of hse energies [16] and agnion [17] in Neufahrn and Pfaffenhofen are examples of allothermal gasifiers applying heat pipes for the heat exchange to the gasification reactor.

Using air as gasification agent increases the volume fraction of nitrogen up to 60 % and decreases the energy density of the producer gas and the partial pressure of potential reactants such as CO and H_2. The application of oxygen as gasification medium requires an additional oxygen-producing plant which increases costs and energy consumption.

Categorizing gasifier technologies by the arrangement of the four sub-processes, fixed bed, moving bed and entrained flow gasifiers can be discerned. Fixed bed gasifiers can further be classified as updraft (counter-current) and downdraft (co-current) gasification reactors. Updraft gasifiers generate a tar rich producer gas with exit temperatures up to 300 °C because the gasification agent is introduced at the bottom of the gasifier and the biomass on the top. If biomass and gasification agent are introduced in co-current direction, the producer gas has to pass the oxidation zone generating a producer gas with low tar content and exit temperatures up to 900 °C. Fixed bed gasifiers are used for smaller scale gasification reactors with thermal inputs up to 20 MW as compared to moving bed gasification reactors.

Moving bed gasifiers consist of fluidized beds (FB). Depending on the flow velocity of the gasification agent it is either a stationary (bubbling) (BFB) or a circulating fluidized bed (CFB). The bed material can consist of silica or alumina based materials. Catalytically active material can be added in addition. Fluidized beds provide good heat transfer to the biomass particles increasing conversion efficiencies. Moving bed gasification reactors are built for thermal inputs up to 200 MW.

Entrained flow gasifiers use powders (e.g. coal) or slurries (e.g. bio-slurry) as feedstock. They are operated at high temperatures up to 2000 °C with oxygen as gasification agent. Entrained flow gasifiers for biomass are often combined with pyrolysis reactors. A recent example of an entrained flow gasification process combined with a fast pyrolysis reactor is the biomass to liquid (bioliq®) plant in Karlsruhe using straw as feedstock [10].

2.3   Contaminants

Depending on the kind of biomass feedstock and gasifier technology, different amounts and compounds of contaminants and trace elements are present in the producer gas [18-20]. Seven groups of impurities can be discerned:

1. Particulate matter
2. Tars
3. Sulfur compounds
4. Halides
5. Alkali
6. Nitrogen containing compounds
7. Others

Except filter units, any equipment downstream of the gasifier can tolerate only a certain degree of particulate matter without failure or loss of performance due to blockages. Especially porous layers with the same pore sizes as the particles (micron- to submicron) but also gas turbines get damaged by particulate matter. Particulate matter can consist of ash and soot from the biomass feedstock but also of bed material and catalytically active material applied in the gasifier. A hot gas filter operated at the exit temperature of the gasifier as first process unit after the gasifier will avoid problems of particulate matter for downstream equipment. Grain ceramic filter candles provide filtration grades for gases of 0.5 µm and lower and filtration efficiencies up to 99.999 % [22]. Hot gas filtration is described in chapter 2.5.

Tars can cause damage to equipment due to condensation, soot formation or inhibition of catalytically active centers or sorption material. The amount of tar in the producer gas strongly depends on the gasifier technology, the operating temperature, the steam to carbon ratio and the application of catalysts in the gasifier. Depending on the energy conversion system, tars can be considered as fuel. High temperature tar removal options include non-catalytic (non-catalytic partial oxidation, plasma) and catalytic solutions. Catalytic material can be applied in-situ as bed material or in addition to bed material. Natural minerals such as dolomite, olivine, clay minerals and ferrous metal oxides or artificially modified materials such as chars, fluid catalytic cracking (FCC) catalysts, alkali metal carbonates, activated alumina and transition metals can be used for in situ application. Downstream of the gasifier bed, e.g. catalytically active monoliths can be used for tar cracking or reforming. The catalytic materials can be similar to materials used for the in-situ tar decomposition and in addition metal (Ni, Fe, Co, Mo) and noble metal (Pt, Pd, Rh,

Ru) based catalysts can be applied. More information regarding Ni-based and noble metal based catalysts can be found in chapter 2.6.

Sulfur is known as poison for catalysts containing Ni, Cu, Co or Fe as used in methanation, liquid fuel synthesis and fuel cells. The most abundant compound is H_2S followed by COS. Sulfur containing hydrocarbons are often neglected though the sum of them can build a substantial fraction of the total sulfur concentration. Sulfur tars found in producer gases are mercaptans, thioethers, disulfides, thiophenes, benzothiophenes and dibenzothiophenes [23]. In wood, the sulfur content is higher in the bark than in the core of the trunks. For that reason, the sulfur content of producer gas from wood pellets is lower, because bark is not used to produce pellets, than from wood chips. So far only H_2S can be removed from the product gas to sub-ppm levels by sorption beds but no other sulfur compounds such as sulfur tars. Therefore other sulfur species than H_2S have to be converted to H_2S to enable desulfurization of the producer gas. Bulk desulfurization of H_2S can be done by sorption materials added to the gasifier (in-situ) or upstream of the HGF unit. Ca-based sorption materials such as limestone or dolomite are used for bulk desulfurization. Downstream of the HGF unit, after bulk desulfurization, metal oxide beds can be implemented to reduce the H_2S concentration to sub-ppm levels. More information about the conversion of sulfur containing hydrocarbons can be found in chapter 4 and about sorption of H_2S in chapter 2.4 and 2.7.

Halides are mainly represented by HCl in biomass producer gases and to a minor extend by HF and HBr. Halides are known to cause high temperature corrosion and catalyst poisoning. They can be removed from the producer gas by sorption materials as presented in the next chapter 2.4.

Alkali metal compounds cause corrosion to turbine blades or heat exchangers and damage to catalysts. Sodium (Na) and potassium (K) are the main alkali elements in producer gas from biomass. Alkali salts evaporate at temperatures above 800 °C and can be removed by filtration at temperatures below 600 °C. At higher temperatures, sorption materials can be used to remove Alkali compounds from the producer gas as presented in the next chapter 2.4.

Nitrogen containing compounds are ammonia (NH_3) and hydrogen cyanide (HCN) but also organic compounds such as e.g. pyridine have to be considered. At high temperatures, as present in gas engines and turbines, nitrogen oxides (NO_x) can be formed that has to be removed from the exhaust gas. Strict legal limits and difficulties to remove nitrogen oxides in the exhaust gas make the removal prior to the combustion the preferred solution. Ammonia can adsorb on catalyst active sites reducing catalyst activity but can also be considered as fuel in high tempera-

ture SOFC. If ammonia needs to be removed from the producer gas, its good solubility in water makes wet scrubbers an efficient solution though at low temperatures. Regarding hot gas cleaning, only catalytic decomposition to N_2 and H_2 is possible with similar catalysts used for tar decomposition such as dolomites, nickel- and iron-based catalysts.

Other impurities such as trace elements can be found in biomass derived producer gases. Trace elements originate from feedstock but also from components of different process units. Some impurities such as Mg, Ca, Pb and V are known to cause depositions and corrosion to gas turbines. Trace elements such as As, and P are reported to cause severe damage to SOFC, Cd caused significant performance loss, Zn, Hg, Sb degraded the cell power density to a lesser extent [24-28]. It is expected that trace elements will have negative long term effects on other catalysts as well. Sorption material can be used to remove some of the trace elements though further investigations are needed. In chapter 2.4, char and celatom are described as possible sorption materials.

2.4   Sorption materials upstream of HGF

Sorption materials can be added to the producer gas directly in the gasifier or upstream of the HGF unit. Reactions can take place in the gasifier, during the flight of the particle in direction HGF and in the filter cake once the sorption particle reached the filter element. Adding sorption materials to the producer gas stream will decrease the temperature of the producer gas, increase the amount of particulate matter and change the characteristics of the filter cake. Sorption materials upstream of the HGF can be used to remove H_2S, alkali, halide and trace elements. Optimization is needed regarding costs, removal efficiency and increased lifetime of downstream equipment due to the absence of impurities. Costs include the sorption material and feeding system, the heat reduction and increased filtration intensity.

The sorption capacity of the filter cake consisting of very fine fly ash generated during gasification is not to underestimate providing a large amount of high surface area material. It appears to be an excellent sorbent on which metal and contaminant compound vapours can condense and then be captured by particulate collection devices [24, 29].I t is also found that Cd, Se, As, Pb and Zn may be removed to some extent by fly ash sorption [24]. Char has been investigated as catalyst for tar decomposition [30, 31].

Calcium based sorbents such as naturally available dolomite and limestone but also calcium acetate or calcium magnesium acetate are used for bulk H_2S removal (Eq. 2.3, Eq. 2.4). Calcined limestone and dolomites are the most often used solids for HCl capture in flue gas from coal combustion plants [19]. CaO and MgO react easily with HCl forming $CaCl_2$ and $MgCl_2$ with melting points of 774 °C and 695 °C, respectively [32, 33]. Sodium and potassium compounds are also capable of reducing HCl concentration (Eq. 2.5). Nahcolite is another naturally available option for HCl removal (Eq. 2.6). Nahcolite is a cheap, natural mineral, having a cost of about $50/ton, and sorbent regeneration is not necessary. This approach to halide removal has been demonstrated at a pilot scale by Siemens [29]. Trona can be used to remove H_2S and HCl. With trona sorbents, HCl was reduced to a 40 ppbV level at 600 °C from initially 20 ppmV [34, 35]. H_2S captures was investigated at 600 °C and 800 °C resulting in 1.8 ppmV and 1.0 ppmV respectively with corresponding H_2S in the raw syngas of 100 ppmV and 200 ppmV respectively [34, 35].

$$CaCO_3 + H_2S \rightarrow CaS + H_2O + CO_2 \qquad \text{Eq. 2.3}$$

$$CaO + H_2S \rightarrow CaS + H_2O \qquad \text{Eq. 2.4}$$

$$2NaCl + Al_2O_3 + H_2O \rightarrow 2NaAlO_2 + 2HCl \qquad \text{Eq. 2.5}$$

$$NaHCO_3 + HCl \rightarrow NaCl + H_2O + CO_2 \qquad \text{Eq. 2.6}$$
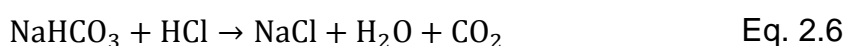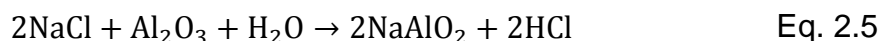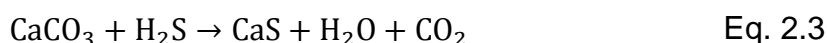
Dou et al. [18, 32] tested alkali metal removal capabilities of second-grade alumina, bauxite, kaoline, acidic white clay and activated alumina in a fixed bed reactor at 840 °C with coal derived gas. Al_2O_3 showed the highest adsorption efficiency. Aravind et al. [20] found that at temperatures above 800 °C physisorption is favoured and the potential re-emission of HCl by chemisorption is significantly reduced. Tran et al. conducted tests with kaolin in a fixed bed reactor and reported good efficiencies for the removal of KCl [36]. Turn et al. report good physical adsorption and chemisorption of Na and K by bauxite but no effect for Cl [37].

Celatom is a granular, calcined, diatomaceous earth and represents a low cost, high temperature sorbent often used for a variety of applications requiring high stability and sorption capacity. It is an alumino-silicate material and a rather effective polishing sorbent for As, Se and Zn [24]. CaO and CuO on activated carbon are other sorbents suitable for the capture of arsenic [24, 38].

Table 2.1 lists sorption materials including tested temperature, pressure and contaminants.

Sorbent	Tested Temp. [°C]	Tested Pressure [bar]	Literature	Observation
CaO	650	1, 5	[24]	H_2S, As
Calcium carbonat ($CaCO_3$)	600 - 800	1	[34, 39]	H_2S, HCl
Celatom (SiO_2)	650	1, 5	[24]	As, Se, Zn
Nahcolite ($NaHCO_3$)	430 - 600	1	[29]	H_2S, HCl
Trona (Na_2CO_3, $NaHCO_3$ $2H_2O$)	430 - 600	1	[10, 29, 35, 39]	H_2S, HCl
Na_2CO_3	450 - 500	1	[10]	H_2S, HCl
Na_2O	450 - 500	1	[10]	H_2S, HCl
K_2CO_3	450 - 500	1	[10]	H_2S, HCl
CuO/C	30 - 140	52	[10]	As
Dolomite ($CaMg(CO_3)_2$)	650 - 1050	1	[18, 19]	H_2S
Limestone ($CaCO_3$)	500 - 1050	1 - 20	[19]	H_2S
Calcium acetate $Ca(CH_3COO)_2$	600 - 1050	1	[19]	H_2S
Calcium magnesium acetate $Ca_xMg_y(CH_3COO)_{2(x+y)}$	800 - 1000	1	[19]	H_2S
Al_2O_3	840	1	[32]	NaCl, KCl

Table 2.1: Sorption materials overview

Combined removal of H_2S and HCl by the same sorption material is preferred. Further investigations are needed regarding the use of sorption material or a combination of sorption materials in the gasifier, upstream of the HGF or as fixed bed downstream of the HGF unit.

2.5   Hot gas filtration (HGF)

According to VDI guideline, hot gas filtration is defined as filtration at temperatures higher than 260 °C [40]. Conventional bag filters show high performance and efficiency up to temperatures of 200 °C to 370 °C but ceramic and some metallic filter elements can be used at temperatures above 400 °C. High-temperature filtration (400 °C to 800 °C) with ceramic filter candles offers a wide potential for the optimi-

zation of high-temperature processes, e.g. fouling and erosion of downstream components could be avoided.

High dust load and sticky ash particles from biomass gasification are challenging conditions for HGF. High content of ash and soot particles ask for regular cleaning of the filter elements. The filter elements are cleaned from filter cake by back pressure pulses. Cleaning the filter pores and filter surface by back pressure pulses has to guarantee stable filter operation. A stable operation of the filter equals a constant pressure drop over the HGF unit. Still, cleaning pulses should be as few as possible and at the lowest pressure difference possible in order to protect downstream equipment from pressure pulses and to save costs for energy and recleaning medium.

Different parameters such as recleaning pressure, recleaning gas volume, time interval between the cleaning pulses and filtration velocity have to be optimized to enable a stable HGF operation. Filtration velocity (m s^{-1}) equals the gas flow of raw gas (m^3 s^{-1}) divided by total filter area (m^2). It has been observed that the maximum pressure in the filter sector to be recleaned and the gradient of the pressure build-up during a back pressure pulse are the most important parameter to ensure the performance of the filter element recleaning [41, 42]. The pressure increase velocity (pressure gradient) is a function of the kind of recleaning system, type of filter elements, filtration velocity, filter design and recleaning intensity. The recleaning intensity equals the pressure difference of the filter candle inside to the raw gas sector.

For cost saving and filter performance reasons, it is crucial to understand the filtration and recleaning mechanisms as detailed as possible. Dynamic pressure measurements help to detect filter failures early. The following filter failures reduce filter performance and increase operational costs: leakages, blockages, filter candle fracture, valve malfunctioning, filter area reduction (patchy cleaning), and filter pore size reduction (depth filtration). The main causes for filter failure are the design of filter unit, type of filter material, filter candle wall thickness and strength, thermal stress and residual ash deposition [43]. Correct filter operating parameters such as flush tank pressure, valve opening time and recleaning interval, can avoid accelerated filter area reduction and filter pore size reduction. The knowledge about resistance of filter material, ash and particle properties, dust load, filtration velocity and filter design permits finding the correct filter operating parameters.

2.5.1   Coupled pressure pulse and jet pulse recleaning systems

Up to now, conventional high-temperature filtration units cannot ensure long-term stable operation with dust from biomass conversion for temperatures above 450 °C. One of the main reasons is the limitation of the jet-pulse recleaning system. The newly developed coupled pressure pulse (CPP) recleaning system overcomes these limitations. As shown in Figure 2.2, CPP system enables higher recleaning intensities at lower recleaning pressures compared to conventional jet-pulse systems [44].
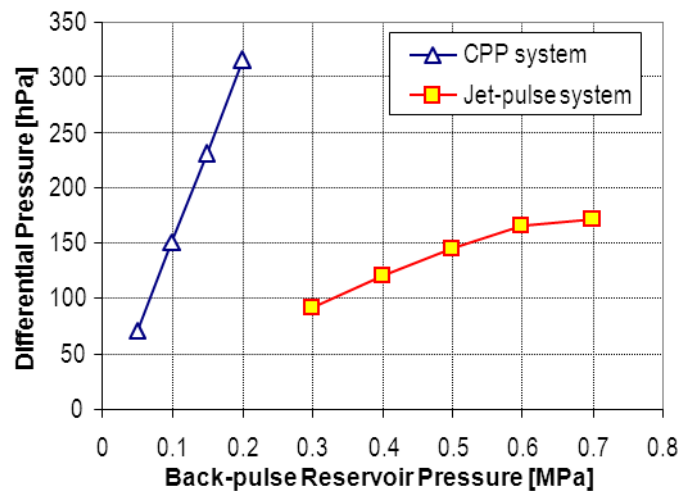
Figure 2.2:   *Comparison of recleaning intensity reached by jet pulse and coupled pressure pulse (CPP) recleaning systems [45]*

Jet pulse technology applies a high pressure, high speed gas jet directed to a bundle of filter candles. Different nozzle designs and venturi ejectors are used to optimize the gas flow of the jet. The kinetic energy of the jet has to be transformed to static pressure along the filter candle. After deceleration of the jet, static pressure is recovered and recleaning back pressure pulse is generated. Lower recleaning intensities are measured at the entrance of the filter candle applying jet pulse technology (Figure 2.3). Not the whole recleaning sector is equally set under pressure as compared to CPP technology.

CPP technology applies a high volume gas flow setting the whole recleaning sector under overpressure. There is no gas jet and gas velocities stay below the speed of sound (Ma < 1). The recleaning back pressure pulse is directly coupled to the recleaning compartment (Figure 2.3). The volume of the flush tank, the diameter of the high speed valves and the connection to the recleaning sector have to be large enough to enable a fast pressure increase of the whole recleaning sector. The pressure in the flush tank can be set at 200 hPa to 1'000 hPa above the pres-

sure in the raw gas sector which is enough to reach high recleaning intensities as compared to jet pulse (Figure 2.2).
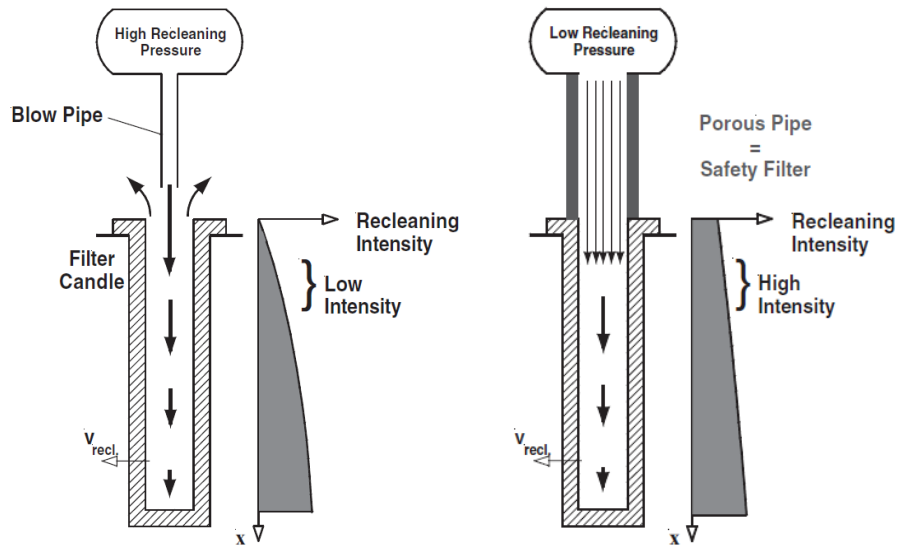
Figure 2.3: *Drawing of jet pulse and coupled pressure pulse (CPP) recleaning systems [46]*

2.5.2 Vertical and horizontal filter designs

Conventional filter designs install filter elements in vertical position. The filter elements are fixed on one side on the separation plate dividing raw gas and clean gas sector. The length of the filter elements in vertical filter design can reach up to 3 m [47]. Higher recleaning intensities of the CPP technology compared to conventional jet pulse technology allow horizontal positioning of the filter candles because the recleaning intensity is expected to be high enough to clean the ash lying on the top of the filter candles.
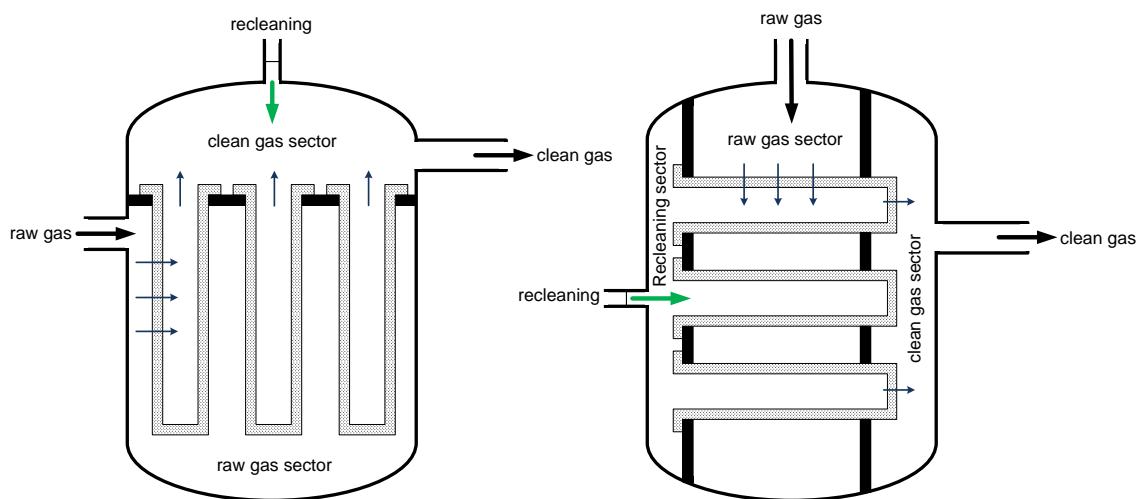
Figure 2.4: *Vertical and horizontal filter design showing raw gas and clean gas sector and for the horizontal filter design an additional recleaning sector*

Filter elements applied in horizontal filter designs are shorter than in vertical designs. Filter elements of length 30 cm and 50 cm are installed in known horizontal filter designs. Longer filter elements could be installed depending on the filtration capacity that is needed. The filter candles are fixed on both sides of the raw gas sector creating a clean gas sector and an additional recleaning sector (Figure 2.4). Fixing ceramic filter candles on two sides increases the mechanical stability tremendously. Implementing a filter design with filter candles of length 0.5 m and both filter ends fixed, the mechanical stability is of no concern.
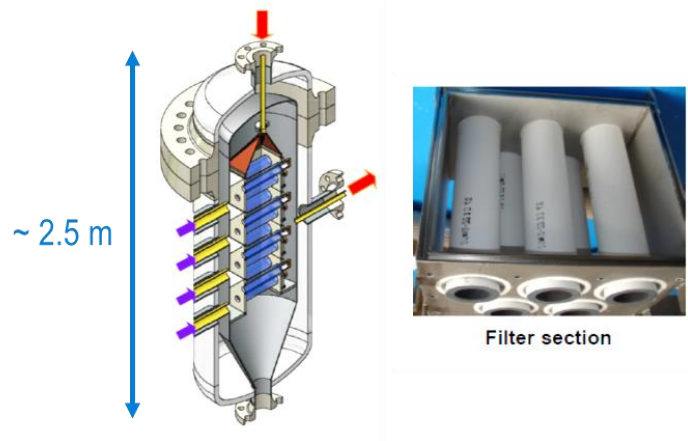
Figure 2.5: *2 MW horizontal filter design with coupled pressure pulse (CPP) recleaning system and one building module [48]*
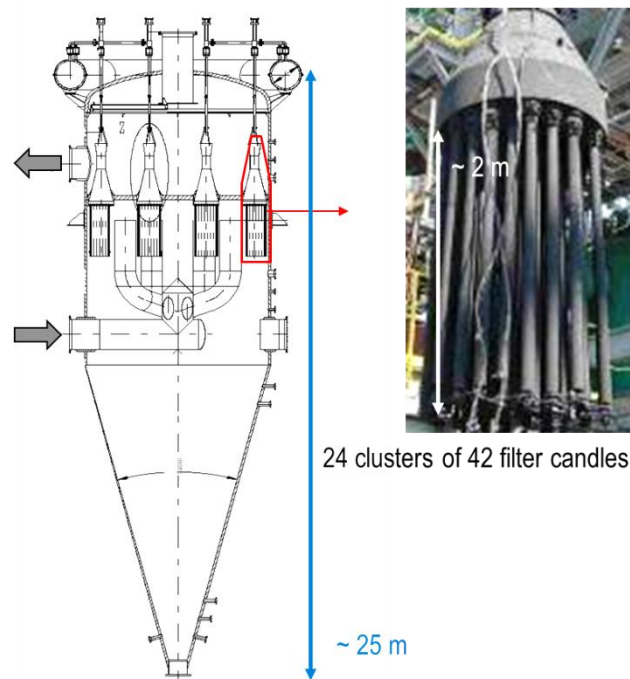
Figure 2.6: *10 MW vertical filter design from Pall with 24 clusters consisting of 42 filters of 2 m length [48]*

The modular design of the HGF with short and horizontal filter candles as shown in Figure 2.5 supports scale up capabilities. First scale up studies show filter volume savings up to 1/3 compared to conventional HGF designs with jet pulse technology

and long filter elements in vertical position [48]. A main reason is the directed particle flow from the top of the filter vessel as implemented in horizontal filter design. Vertical filter designs demand a raw gas sector that is big enough for particles to decelerate and fall down to the bottom of the filter vessel.

There are different examples of filter designs with filter elements in horizontal position though the standard position is vertical and fixed on one side [47]. The combination of HGF and CPP was successfully installed at different scales of pilot plants for several biomass conversion processes [49-51]. A hot gas filter applying CPP recleaning technology with filter elements in horizontal position is installed at Paul Scherrer Institut (PSI) and was used for the studies presented in this thesis. The HGF is used to clean product gas produced by a wood pellets gasifier. The design of the filter was developed in cooperation with the Karlsruhe Institute of Technology (KIT).

2.5.3 Pressure measurements of filters

Pressure measurements enable the observation of stable filtration processes and allow controlling the effectiveness of the chosen set of filter operating parameters. Constant pressure drop over the filter unit is an indication of a stable filtration process. Constantly increasing pressure drops indicate unsustainable filtration and operating parameters have to be adjusted accordingly. The earlier unstable filtration can be detected the better are the chances of directing the filtration process to sustainable operation. Once the filter condition reached a critical level which is shown in high pressure drop, it is likely that a stable filter operation cannot be recovered anymore (see chapters 3.2.1 and 3.2.2).

Pressure difference sensors are the standard method to control filtration operation. Resolutions up to 1 Hz are used to follow the build-up of pressure difference over the filter candle wall. Once a certain pressure difference is reached, the back pressure recleaning pulse is triggered. Since the recleaning of the filter candles by a recleaning pulse takes less than one second, it is impossible to measure pressure changes with standard pressure sensors which are able to measure with a frequency up to 1 Hz.

The method of dynamic pressure measurements used in this study records pressure changes during recleaning pulses with a frequency of 1'000 Hz. This enables the evaluation of recleaning intensities such as pressure increase velocity and pressure maximum reached inside the filter candle. Depending on the location and the number of sensors that are installed, it is possible to measure the actual valve

opening time and pressure maxima in other sectors. Measurements can be conducted during commissioning and operation in hot and cold filter state. The comparison of measurements with a reference point permits conclusions about the filter state.

Dynamic pressure measurements proved to be a powerful tool to measure pressure changes at rates of several thousand Hz. Most of the research covers pressure distribution along filter elements. While some focus on the pressure over the filter element only [52-54], others add information regarding the pressure within the filter wall [55], the gas and particle flow in the whole filter vessel [56-59], the inhomogeneity of the filter permeability [60], the filter cake growth and compression [61-74], the detachment of the filter cake [75-77] and filter failure [78].

2.5.4 Filter model for CPP recleaning systems

A CPP filter model was developed helping to understand recleaning efficiencies and filter failures. The filter model calculates the pressure evolvements over time in different filter sectors. The emphasis was on the correct simulation of the maximum pressure in the sector to be recleaned. The model supports calculations for the scale-up of HGF units.

So far, no model was presented to calculate pressure development during back pressure pulses generated by CPP technology. Regarding CPP technology, pressure drop simulations were presented focusing on safety filter operation and broken filter candles [79, 80]. Most of filter models implement jet pulse recleaning technology. Jet pulse models ask for the implementation of energy conservation equations due to the high speed of the jet where kinetic energy has to be transformed to static pressure.

Standard jet pulse filters use long filter candles up to 3 m. Therefore it is necessary to consider the pressure drop along the filter elements. The horizontal filter design applies filter elements as short as 0.5 m. For that reason, pressure drop along the filter element can be neglected. Due to the low gas velocities and the short filter elements of the horizontal filter design with CPP technology, a filter model based on mass conservation was developed assuming steady state conditions within a discrete time interval (dt).

2.6 Catalytic conversion

The ability of the catalyst to decompose sulfur containing hydrocarbons is a precondition for the proposed process chain applying HGC in combination with a metal oxide bed to remove H_2S. The conversion of sulfur free tars has second priority. The catalyst activity regarding water gas shift (WGS) reaction and steam reforming of methane (SRM) has minor relevance regarding the desulfurization step. Tars and methane in the producer gas are unproblematic to some extent in case solid oxide fuel cells (SOFC) are used for electricity production. Tars can be considered as fuel and methane is used for internal cooling of the fuel cell [81].

Several studies cover the performance of catalytic conversion of tars in biomass gasification fuel gases [82-94]. Ni based catalysts show high activities but are prone to sulfur poisoning below 900 °C. Therefore, the performance of noble metal catalysts below 900 °C in the presence of sulfur is of special interest. Lower operating temperatures will better suit exit temperatures of biomass gasifiers. Additional heating of the producer gas to reach temperature around 900 °C can be avoided.

Rönkkönen et al. investigated ZrO_2 based catalysts in the temperature range of 600 °C to 900 °C and report naphthalene conversion rates around 80 % with high O_2 concentration in the gas and temperatures of 900 °C indicating that the main reactions in naphthalene decomposition on ZrO_2 are oxidations [95]. The performance of Rh, Ru, Pt, and Pd on modified commercial zirconia support (m-ZrO_2) regarding naphthalene, toluene and ammonia decomposition was compared to a benchmark Ni/m-ZrO_2 catalyst in the presence of H_2S in recent studies. Rh/m-ZrO_2 was found to be the most promising catalyst.

Furusawa from University of Tokyo in Japan compared Co/MgO and Ni/MgO catalysts for steam reforming of naphthalene as a model compound of tar derived from biomass gasification [96]. Although the catalytic performance showed that Co/MgO catalyst had higher activity (conversion: 23 %, 3 h) than any kind of Ni/MgO catalyst tested in that study, the conversion rate is very low. In the latest studies from Furusawa et al. they studied the influence of support on the catalytic performances of Pt and Ni based catalysts for the steam reforming of naphthalene and benzene as model tar compounds of biomass gasification. They concluded that Pt/Al_2O_3 showed the highest and most stable activity of the tested catalyst supports at 800 °C [97].

Cui et al. [98] looked at permanent gas species, tar compounds, sulphur compounds, and ammonia produced from a bench-scale (1 kg h^{-1}) fluidized-bed biomass gasifier. Two commercial Ni-based catalysts and one commercial ZnO sorbent were evaluated under varied conditions by quantifying contaminants from the gasification reactor inlet and outlet.

There are several groups working with catalytic active filter elements (chapter 2.7). Nacken et al. [85, 86, 99] worked with silicon carbide-based filter elements catalytically activated with Ni. Naphthalene conversion rate up to 66 % is reported in an environment with 100 ppm H_2S. Rapagnà et al. applied activated filter elements in the free board of a lab-scale fluidized-bed gasification reactor [87, 100, 101]. At temperatures up to 840 °C a tar conversion rate of 58 % is reported. Simeone et al. [50, 51] tested ceramic hot gas filter elements with mullite membrane coating and integrated Ni-based catalyst with a dust free model gas. A Naphthalene conversion rate of 99.4 % was measured at 850 °C and 30 vol% H_2O with 2.5 g m_n^{-3} of Naphthalene. Experiments with higher steam content showed higher conversion rates.

Prof. José Corella's group from University Complutense of Madrid in Spain published four articles about high dust catalytic hot gas cleaning with monoliths in biomass gasification in fluidized beds reporting 1.) their effectiveness for tar elimination [102], 2.) modelling of the monolithic reactor [103], 3.) their effectiveness for ammonia elimination [104] and 4.) performance of an advanced, second-generation, two-layers-based monolithic reactor [105]. As conclusion of the fourth paper, Toledo et al. write that Ni-based catalysts are not the definitive answer to the problem and that non-nickel-based monoliths working at even lower temperatures would be welcomed.

Steam, tars and sulfur species have to be considered to simulate realistic producer gas. Sulfur in the form of H_2S was often considered in the studies mentioned before because sulfur free producer gases will hardly exist. It is important to consider steam content when evaluating performances of tar reforming catalysts since gasifiers using steam as gasification agent create producers gases with steam contents up to 50 vol% [106]. Most of the studies use merely toluene and naphthalene as model compounds. Sulfur containing hydrocarbons were usually not considered. The lack of appropriate analytical equipment and methods could be one reason for neglecting hydrocarbons containing more than one benzene ring and sulfur. The variety of sulfur containing hydrocarbons found in biomass gasifier gas was shown by Rechulski et al [23]. Up to 41 different sulfur tars could be detected. The most abundant were thiophenes, followed by benzothiophenes and diben-

zothiophenes. The amount of sulfur containing hydrocarbons in biomass producer gases can be above acceptable tolerance levels of the catalytic process.

2.7   Reactive hot gas filter

Integrated concepts of HGF and reformer catalyst promise cost and energy savings due to the reduction of operating units, the decrease of temperature losses between operating units, the compact design and straight forward process units. If integrated concepts with the tested catalyst would be possible and feasible has to be evaluated in this study. The performance of HGF and reformer catalyst has to be well understood to permit the combination of the two process units

So far the limiting factor was the maximum temperature of the hot gas filter (400 °C), hence the reformer or CPO was operated upstream of the filter with high dust load. In order to lower the risk of particle and soot deposition in monoliths, monoliths with low cell densities (cpsi) were selected. With the recent development of hot gas filter designs and of ceramic filter elements that can be used up to 850 °C, it is possible to install reformer/CPO in a low dust environment at very high temperatures.

There are two examples in Europe where catalytic tar reforming is applied at industrial size combined heat and power (CHP) plants: Kokemäki in Finland (Figure 2.7) and Skive in Denmark (Figure 2.8). Both reformers are operated at high dust load. At the time of basic engineering of these plants (around 2003), no hot gas filtration technique in the range of 400 °C to 800 °C was available. For this reason, the reformers were built in massive size being able to scope with the high particle load. The sizes of the reformers were almost as big as the gasifiers themselves. The two plants differ in the gasifier and reformer technology as shown in Table 2.2.

Site of installation	Gasifier technology	Reformer technology
Skive (Dk)	Autothermal Fluidized Bed	Steam Reformer
Kokemäki (Fin)	Updraft Fixed Bed	Catalytic Partial Oxidation

Table 2.2: Gasifier and reformer technology of Skive and Kokemäki plant

Only little information about the experience from the two plants is published. Kurkela et al. published the final activity report of the BIGPower project which is the Kokemäki plant [107]. Rönkkönen et al. was involved in the same project [95, 108, 109]. Only workshops presentations are available about the Skive plant [110, 111]. It is stated that noble metal reformers show very promising results compared

to Ni-based catalysts with tar conversion rates higher than 93 % at temperatures of 850 °C. It also says that overall costs of such processes need to be reduced by simplification and new innovations [110]. The other presentation states that the monoliths tar removal capabilities of 50 % to 70 % at operating temperatures between 850 °C and 930 °C is not satisfactory. A photograph showing the monolith with most of the channels covered heavily with dust explains the problem of tar reforming in a high dust environment [111].
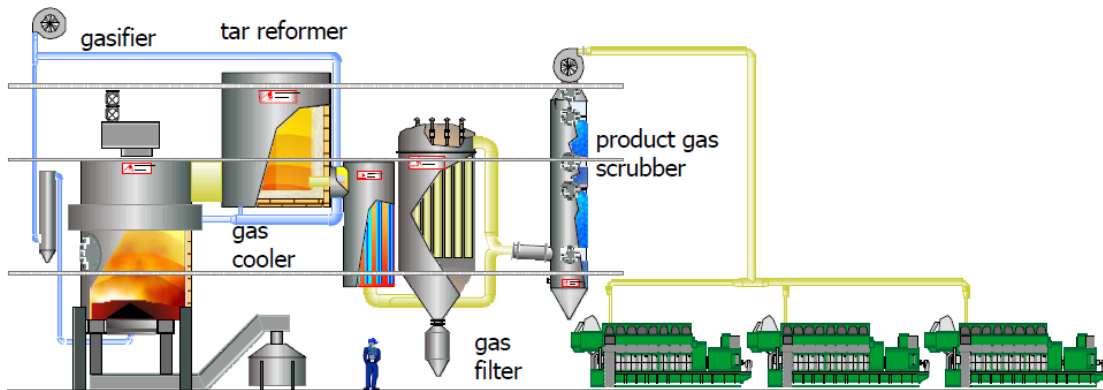
Figure 2.7: *CHP plant Kokemäki (Finland): updraft fixed bed gasifier with catalytic partial oxidation (CPO) for tar reforming [107]*
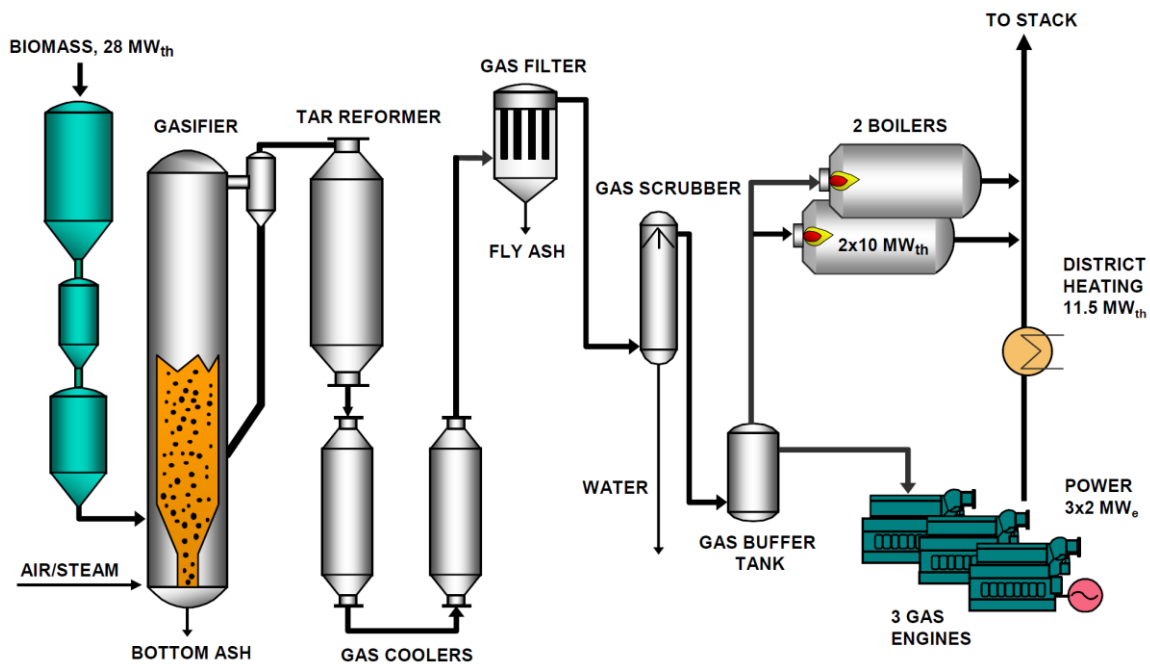
Figure 2.8: *CHP plant Skive (Denmark): autothermal fluidized bed gasifier with steam reformation for tar reforming [111]*

Options to integrate the reforming catalyst in the HGF are shown in Figure 2.9. Filter designs with filter elements mounted in horizontal or vertical position were considered. Integration options of the vertical filter design are the application of catalytic active filter elements [99, 112], mounting an additional catalytic active foam cylinder at the inside of the filter element [86, 113] or placing a monolith at

the exit of the filter vessel. Because the back pressure pulse used for recleaning the filter elements is conducted from the opposite side of the clean gas filter exit, additional integration options arise for the horizontal filter design. A monolith or foam cylinder can be placed at the clean gas exit of the filter candle, where the cleaned producer gas leaves the filter element to the clean gas side [114]. Several criteria have to be considered selecting monolith or foam structures. First, the structures have to offer sufficient surface for the catalyst layer. Second, they have to support a low pressure drop from the inside of the filter candle to the clean gas sector during filtration. Third, they need to evoke a high enough recleaning pressure during back pressure pulses that are needed to clean the filter elements from dust layer at the outside of the filter candle.

catalyst material
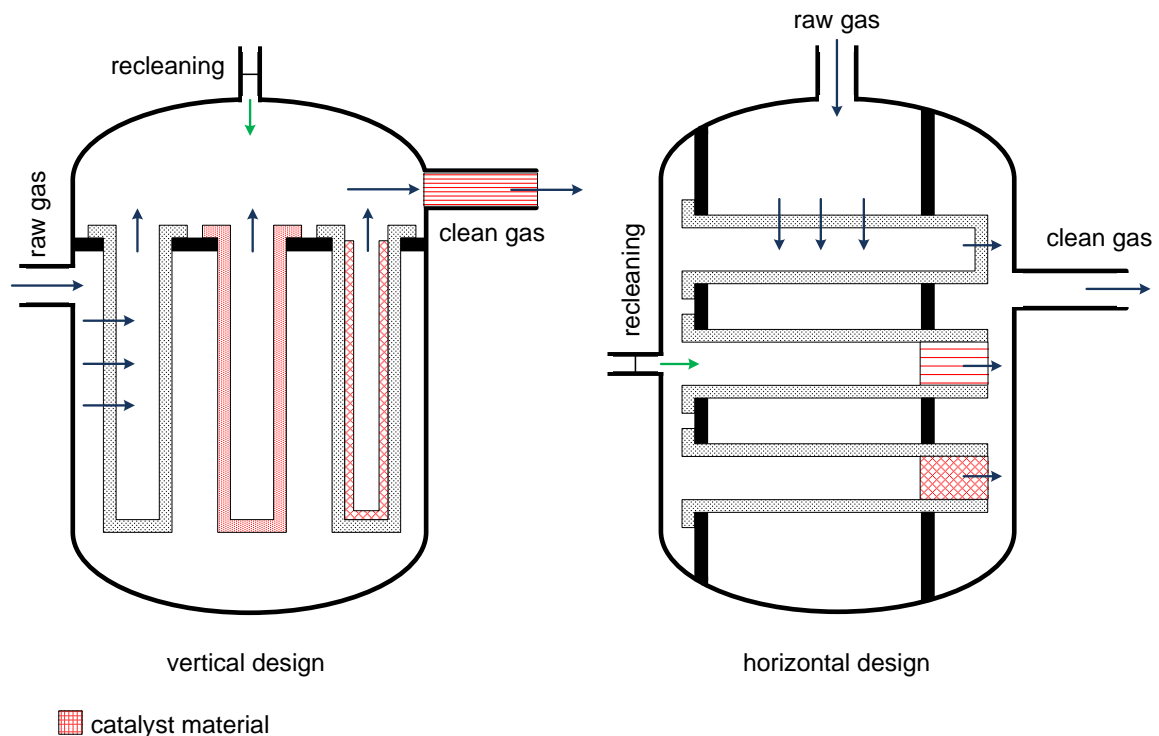
Figure 2.9: *Reactive hot gas filter: Integration possibilities of catalysts in vertical and horizontal filter designs*

The company Pall Filtersystems (M. Nacken and S. Heidenreich) is involved with in situ catalytic ceramic filters for tar reforming since many years together with the Universities of Teramo and L'Aquila in Italy as well as with the Vrije Universiteit Brussel in Belgium and Delft University of Technology in Netherlands [85, 86, 99, 115].

Rapagnà et al. applied catalytic active filter elements placed in the free board of a lab-scale fluidized-bed gasification reactor [87, 100, 101]. These investigations are part of the terminated EU project UNIQUE [116] aiming at integrating the fluidized

bed steam gasification of biomass and the hot gas cleaning and conditioning system into one single gasification reactor vessel.

In the framework of the terminated EU project CHRISGAS [117], ceramic hot gas filter elements with mullite membrane coating and integrated Ni-based catalyst were tested with a dust free model gas by Simeone et al. [118, 119].

2.8 H_2S polishing

After bulk removal of H_2S as presented in chapter 2.4 and the decomposition of sulfur containing hydrocarbons as presented in chapter 2.6, the remaining H_2S can be captured by a fixed bed sorption unit. Metal oxides are commonly used for H_2S removal to sub-ppm levels (Eq. 2.7).

$$\mathrm{Me_xO_y + xH_2S + (\mathit{y} - \mathit{x})H_2 \rightarrow xMeS + yH_2O}$$ Eq. 2.7

ZnO is a very good sorption material for H_2S removal because it shows the most favorable sulfidation thermodynamics. However, vaporization of elemental zinc at temperatures above 600 °C is a draw back. For that reason, zinc ferrite ($ZnFe_2O_4$) and zinc titanate ($ZnTiO_3$) are considered as alternatives where zinc titanate shows the better removal efficiencies at temperature up to 900 °C (Eq. 2.8) [20]. There are also copper-, iron-, manganese- and cerium based metal oxide sorption materials for H_2S removal. Besides calcium based sorbents, zinc titanate shows the highest operating temperatures. An overview about sorption materials for H_2S removal can be found in Meng et al. [19].

$$\mathrm{Zn_2TiO_4 + 2H_2S \rightarrow 2ZnS + TiO_2 + 2H_2O}$$ Eq. 2.8
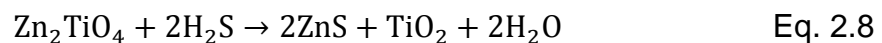
2.9   Fuel cells

Fuel cells are high efficient electro-chemical converters producing electricity and heat free of Carnot-limitations with electrical efficiencies up to 70 % [120]. An ion conducting electrolyte separates cathode and anode. Ions are built by the help of catalytic active material. Electrons moving from ionization to deionization build the current. Depending on the fuel cell technology, only H_2 can be used as fuel or in addition CO and CH_4. Oxygen or air is used as oxidant depending on the kind of fuel cell. Low temperature fuel cells operating at 50 °C to 90 °C are polymer elec-

trolyte membrane fuel cells (PEMFC) and alkaline fuel cells (AFC). New developments enable the operation of high temperature PEMFC up to 180 °C which eliminates the sensitivity to the catalyst poison CO [121]. Phosphoric acid fuel cells (PAFC) are mid temperature fuel cells operating at 160 °C to 220 °C. High temperature fuel cells are molten carbonate fuel cells (MCFC) operating at 600 °C to 660 °C and solid oxide fuel cells (SOFC) operating at 600 °C to 1000 °C. The high temperatures of MCFC and SOFC enable internal reforming of hydrocarbons, decrease the sensitivity to catalyst poisons such as H_2S or HCl but also decrease the life time of the cell components. To increase the life time of the expensive fuel cell stack, developments go in direction of lower operating temperatures.

The fuel flexibility and the capability of internal reforming of hydrocarbons make the MCFC and SOFC attractive solutions for the combination with biomass derived fuel gases. A 1200 h long duration test with an updraft wood gasifier as presented in chapter 3.1.1 and an SOFC from HEXIS [122] was successfully conducted at PSI [123].
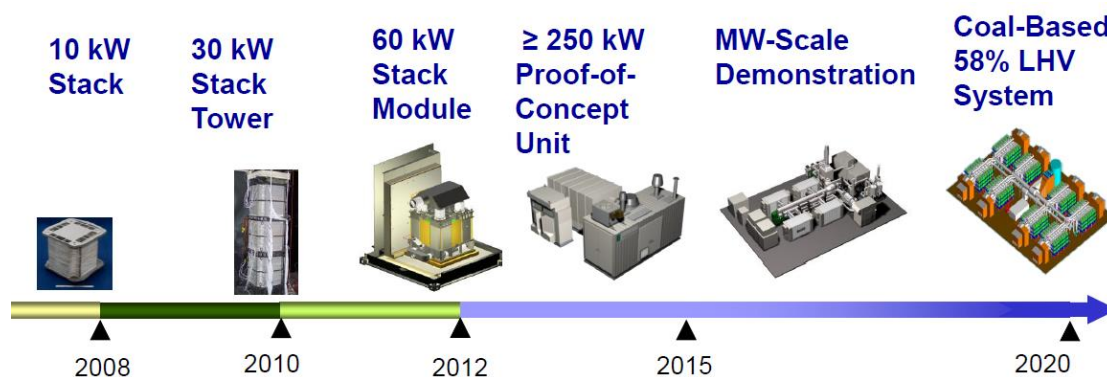
Figure 2.10: SECA program plan from Fuel Cell Energy and Versa Power Systems [126]

An extensive research initiative regarding SOFC was started in 1999 by the U.S. department of energy (DOE) through the national energy technology laboratory (NETL) in the USA called solid state energy conversion alliance (SECA). Together with industry, the main technology barriers regarding SOFC market entry shall be tackled. Stringent and ambitious mile stone completion limits were set in order to guarantee further financing by the U.S. DOE. The clear and well documented objectives enable a convenient observation of the ongoing developments [124]. SECA defined the following mission statement: "Enable the generation of efficient, cost-effective electricity from domestic coal with near-zero atmospheric emissions of CO_2 and air pollutants (99 % CO_2 capture) and minimal use of water in central power generation applications" [125]. Fuel flexibility including natural gas and biogas are considered. SECA defined cost goals of 700 USD kW^{-1} for the power block and 175 USD kW^{-1} for the stack. So far, the projections are within the cost targets.
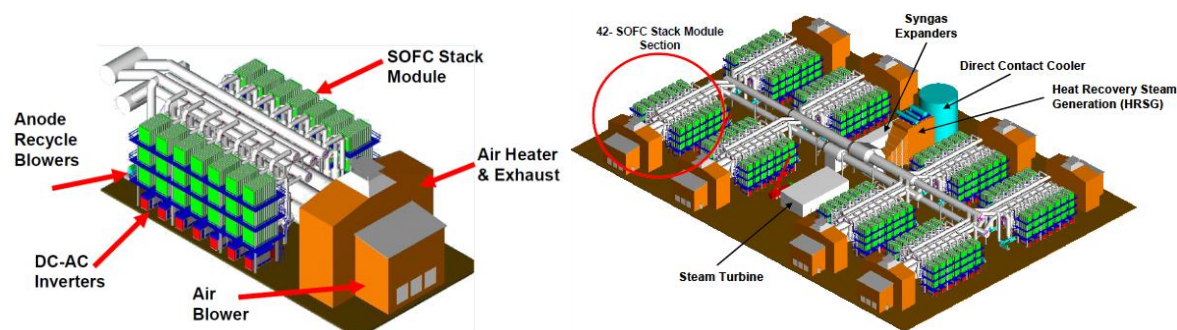
Figure 2.11: *Concept of a 670 MW nominal AC peak power output IGFC plant from Fuel Cell Energy and Versa Power Systems [126]*

Figure 2.10 shows the SECA program plan. A 30 kW stack was tested over 1500 h with a peak power of 25.2 kW and a steady state average power degradation rate of 0.9 % per 1000 h which is well below the SECA target of 2 % per 1000 h [126]. A study of an integrated gasification fuel cell (IGFC) plant with a peak power output of 670 MW nominal AC was conducted including 8 sections of 42 SOFC module clusters with a total of 336 SOFC stack modules as shown in Figure 2.11. The SOFC cluster design takes advantage of modularity of fuel cells using repeated arrangements of grouped components. The program plan in Figure 2.10 shows the integrated gasification fuel cell (IGFC) power plant in the year 2020.

Besides the improvements of stability, performance and costs of the fuel cell materials, the research focuses on the impact of impurities on the catalyst materials [25, 127-132]. To what extent tars derived from biomass producer gases can be regarded as fuel in B-IGFC systems is not completely answered yet [123, 133-136]. Connected to that question is the risk of soot formation in B-IGFC systems [137].

There are a few examples of B-IGFC system installed with SOFCs [138]. Table 2.3 summarizes the locations, gasifiers and literature references.

Location	Country	Gasifier	Literature
Biomassekraftwerk Güssing	Austria	FICFB	[139]
Paul Scherrer Institut	Switzerland	Updraft fixed bed	[81, 123]
Technical University Munich	Germany	HPR	[140, 141]
Danish Technical University	Denmark	two-stage downdraft	[142]
Delft University of Technology	Netherlands	CFB	[134]

Table 2.3: *Installed B-IGFC systems with SOFC*

3 Hot gas filtration

Long duration tests of the HGF with CPP recleaning system operated at 450 °C in combination with an updraft wood gasifier are presented in this chapter. The method of dynamic pressure measurements is introduced and the resulting advantages are explained. A physical filter model for CPP recleaning systems including simulation results is presented.

3.1 Experimental set-up

Figure 3.1: B-IGFC set-up at PSI

3.1.1 Wood gasifier

An updraft wood gasifier produced the fuel gas. Wood pellets were used as biomass input. The gasifier was operated at ambient pressure. The gasification medium was a mixture of air and superheated steam at 650 °C (15 vol%). The thermal input varied between 6.6 kW to 11.2 kW producing 3.25 m_n^3 h^{-1} to 5.8 m_n^3 h^{-1} of fuel gas containing 6 g m_n^{-3} of particulate matter. The amount of particulate matter in the producer gas was determined by the amount of soot and ash that was separated by the hot gas filter. The dust load of 6 g m_n^{-3} was low compared to systems operated under pressure or dust loads containing heavy bed material from the

gasifier. Producer gas composition was measured by a micro gas chromatograph (μGC) and is shown in Table 3.1.

	H_2	CO	CO_2	CH_4	C_2H_x	N_2
vol% (dtf)	11.5	12.5	14.5	2.5	1.0	58.0

Table 3.1: *Gas composition of updraft wood gasifier, average values on dry and tar free (dtf) basis*

The gasifier based on countercurrent fixed bed technology produced up to 100 g m_n^{-3} of tars based on carbon mass balance assuming an empirical tar formula of $CH_{1.34}O_{0.81}$ [143]. The heating value of the empirical tar formula (518 kJ mol^{-1}) was calculated based on the enthalpy of formation. The energy content of the "empirical tars" was approximately one third of the energy content of the producer gas.

The temperature of the producer gas at the exit of the gasifier was 700 °C to 750 °C which is high for an updraft gasifier. This operation mode allowed to have a stable operation of the gasifier/hot gas filter system and to reach an inlet temperature of the filter of 450 °C.

3.1.2 Hot gas filter

Figure 3.2 shows the HGF unit consisting of a filter vessel containing six ceramic filter elements, a flush tank (gas pressure vessel), two high speed valves and an ash discharge. An auger cleans the bottom of the filter vessel from ash. Two baffle plates direct the soot to the auger. Filter vessel and flush tank were kept at temperatures of 450 °C with electrical heating during filter operation with wood gas. The filter unit was operated at ambient pressure. Pressure in the flush tank varied between 250 hPa to 1'000 hPa. The HGF unit was fully automated and could be operated continuously.

Two high speed sliding gate valves (Schubert & Salzer, type 8023) separated the flush tank from the recleaning sectors. The valves opened after a fixed time interval to clean the filter candles from ash cake by blowing pre-heated nitrogen from the inside of the candles into the raw gas area (back-pressure pulse). The valve opening time was set by an electrical signal lasting for 25 ms to 200 ms. The actual valve opening time differs from the set electrical signal due to delays and friction. A description of the actual valve opening time can be found in chapter 3.1.3.1.

Temperature and pressure sensors were placed in the flush tank, inside the filter candle in recleaning sector 1, in the compartment of recleaning sector 2, in the raw

gas sector and in the clean gas sector. The sensors were connected with 8 mm tubes with lengths of 15 cm to 20 cm to the sectors in order to avoid temperatures higher than room temperature. A lance of diameter 8 mm connected sensor 1 and recleaning sector 1. The lance was positioned at the inside of the filter element at half of the filter candle length. Sensor 2 was connected with a lance of same diameter with recleaning sector 2. The lance was positioned in the recleaning compartment in front of the filter candle entrance in sector 2 and did not enter any filter candle.
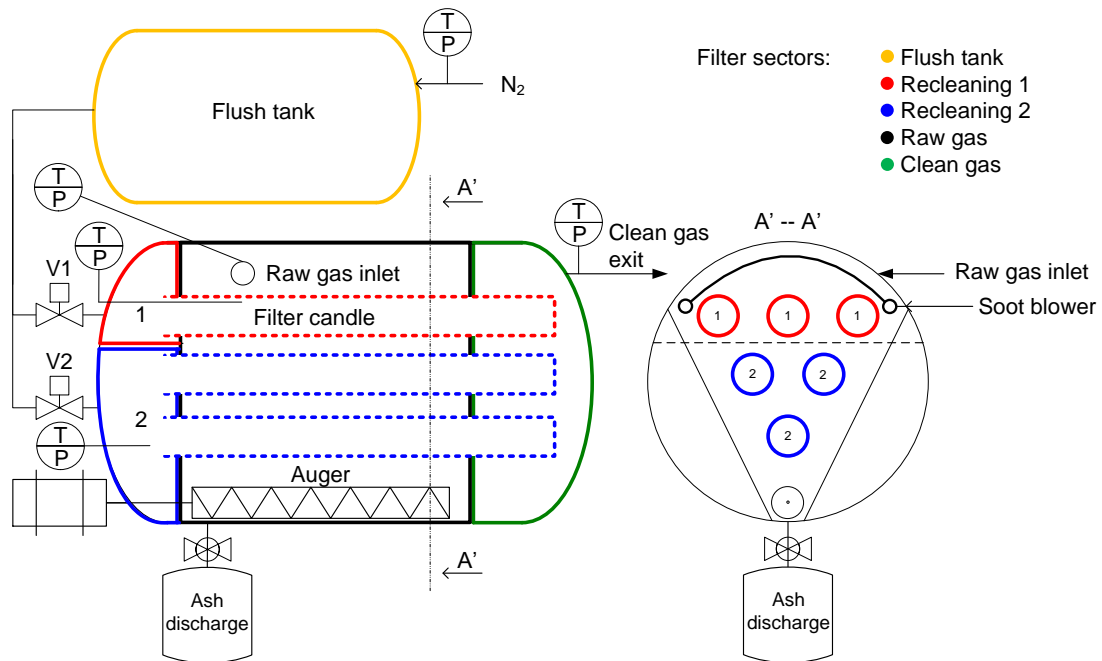
Figure 3.2: *Experimental set up of HGF unit as installed at PSI showing flush tank, filter vessel with six ceramic filter elements in horizontal position divided into two sectors, two high speed valves, soot blowers on both sides of the filter vessel, two baffle plates and ash discharge*

Pressure sensors, used to measure pressures during filtration operation, had a resolution up to 1 Hz and were provided from Jumo (type 40.1001) and Bürkert (type 8320). Fluctuations of the pressure sensors were in the range of ± 2 hPa. Pressure drops were calculated as difference of two pressure sensor measurements. Therefore pressure drop base lines varied by ± 4 hPa.

Pressure sensors used for dynamic pressure measurements during back pressure pulses were low pressure quartz transducers (Kistler, type 7261). The resolution was set at 1'000 Hz. The Kistler sensors were used in combination with Kistler charge meter (type 5015A) and National Instruments data acquisition board (type NI-PCI 6281).

Permanent nitrogen back flush from the sensors to the filter vessel avoided condensation and particle penetration into sensor connections. The influence of nitrogen back flush on the dynamic pressure signals was tested but no influence could be detected.

Table 3.2 shows the volume of each sector, lengths and diameters of the piping.

Sector	Volumes [l]	Tubes	Diameter [cm]	Length [m]
Flush tank	63.3	Flush tank to recleaning sector	4.2	1.0
Recleaning sector 1	4.4	Inlet raw gas	2.4	1.2
Recleaning sector 2	6.6	Exit clean gas	2.4	2.1
Raw gas sector	29.0			
Clean gas sector	11.3			

Table 3.2: Volumes of filter sectors, tube lengths and diameters

A maximum of six filter elements could be installed. The six filter positions were divided into two recleaning sectors consisting of three filter positions each (Figure 3.2). The recleaning sectors were separated by a metal plate which was spot-welded to the filter vessel. Due to the round shape of the separation plate it was difficult to fix it gas tight. The sealing between recleaning sectors will always be difficult to construct. In practice, there will most probably always be a leakage between recleaning sectors.

Filter elements in the recleaning sectors were cleaned consecutively with fixed time intervals of 3 min to 15 min. The duration of the interval should be long enough to establish a filter cake on filter surface. If the interval is too long, there is the risk that the recleaning intensity is not high enough to detach the filter cake from the filter surface. Recleaning intensity is defined as pressure in the activated recleaning sector minus pressure in the raw gas sector.

Fiber ceramic (TENMAT CS 1150) and two types of grain ceramic (Pall DS 3-20 and Pall DS 10-20) filter materials were used for dynamic pressure measurements. For the long duration tests presented in this thesis, only grain ceramic filter candles were used. The filter candles were installed in horizontal position mounted on both sides.

The filter elements had total length of 47.5 cm whereby 2.0 cm was located in the recleaning sector, 36.6 cm was exposed to the raw gas and 8.0 cm of the filter end was located in the clean gas sector. Two times 0.6 cm were covered by filter wall and fixation. Corresponding filter properties can be found in Table 3.3. The length of the filter elements of 0.5 m was much shorter than in conventional HGF systems

where the filter elements are as long as 1.5 m to 3 m, positioned vertically and fixed on one side only [47] (chapter 2.5). Filter area in the raw gas chamber was 4044 cm^2. Depending on the thermal input and the amount of gasification agent, filtration velocity varied between 0.6 cm s^{-1} and 1.1 cm s^{-1}.

Company		Pall		TENMAT
Ceramic material		grain		fiber
Filter candle type		DS 3-20	DS 10-20	CS 1150
Filtration Grade for Gases	[μm]	< 0.3	0.3	< 1.0
Support Material		SL 20 (SiC)		SiC, mineral fibres
Membrane Type		DIA 03	DIA 10	-
Membrane Material		Mullite Grains		-
Porosity Support Material	[%]	38		85-95
Specific Permeability (air, 20 °C)	[10^{-13} m^2]	15	55	250
T_{max} Reducing Atmosphere	[°C]	600		< 1000
Dimensions (d_i / d_o)	[mm]	40 / 60		

Table 3.3: *Ceramic filter candle properties of Pall DS 3-20, Pall DS 10-20 [21] and TENMAT CS 1150 [144]*

The closed filter end in the clean gas sector was used as safety filter element or contained a dynamic pressure switch. If the filter candle end consisted of filter material, the producer gas had to pass two filter membranes from the raw gas to the inside of the filter candle and again to the clean gas side. Therefore, the filter membrane building the second particle barrier is called safety filter (Figure 3.3). The dynamic pressure switch was realized with a metal plate installed at the filter end instead of the safety filter membrane. The metal plate contained a 5 mm hole in the middle to assure low pressure drops over the filter end during filtration while still enabling high pressure maxima inside the recleaning sector during back pressure pulses (Figure 3.4).

Figure 3.3: *Filter elements with closed filter end acting as safety filter*

Figure 3.4: *Filter elements with dynamic pressure switch*

Recleaning filter elements after short time intervals, such as 3 min to 6 min, is a stress test for filters. In practice, filter elements would be cleaned whenever a certain pressure drop is reached. Each time the filter cake is removed from the filter element, fine particles can penetrate into the pores of the filter element and depth filtration occurs which increases the pressure difference of the filter candles irreversibly. For that reason, lifetime of filter elements will increase if recleaning intervals are long enough for a filter cake build-up.

Remaining patches of ash on the filter surface reduce the filter area and support the growth of bigger ash deposits which could lead to so called "bridge building". Bridge building is the connection of surfaces by ash and soot depositions. The compact filter design increases the risk of bridge building. Preceding experiments showed bridge building between filter vessel walls and filter elements and between filter elements in the raw gas inlet area which was located in the upper half of the filter vessel. The lower half of the filter vessel was free of any bigger ash deposits. Therefore a defective ash discharge could be excluded as reason for bridge building.

In order to avoid bridge building, soot blowers were installed on both sides of the filter vessel blowing nitrogen in the space between the filter candles and filter walls. After the initial commissioning phase, where the soot blowers were operated manually, the soot blowers were activated at fixed time intervals of 1 h at pressures of 1 MPa. To reach higher recleaning intensities, the pressure of the flush tank was increased to 0.1 MPa every 6 h for a period of 20 min which corresponds to three back pressure pulses for each recleaning sector if the recleaning interval was set at 6 min.

Filter candle regeneration procedures were applied during 15 min to 30 min shut down periods of the gasifier. During the time when the gasification process was stopped, the filter was regenerated with steam and air. The flow of steam and air at temperatures of 450 °C was able to clean the pores of the filter candles. After regeneration, the pressure drop over the filter candle walls decreased to initial values as shown later in chapter 3.2.3 and 3.3.2.

3.1.3 Dynamic pressure measurements

3.1.3.1 Method of dynamic pressure measurements

Due to the evolution of a jet pulse inside the filter candle and the according conversion of kinetic energy to pressure energy, it is crucial to measure the differential pressure along the whole filter candle length [76, 77]. The differential pressure in-

creases along the filter candles towards the end. Applying dynamic measurements to a HGF set-up with jet pulse recleaning system requires a connection of the dynamic pressure sensor to the inside of the filter candle since the pressure in the compartment of the recleaning sector is not representative for pressures reached inside the filter candles. If only one sensor would be placed inside the filter candle, a representative location has to be evaluated taking into consideration the development of the recleaning intensity along the filter candle.

In case of CPP recleaning systems, the pressure increase in filter candles and in recleaning sectors should be similar due to the minimal kinetic energy contained in the high volume gas flow. For that reason it was enough to install only one sensor in the compartment of the recleaning sector to measure the recleaning intensity representatively. This makes the method of dynamic pressure measurements particularly attractive for CPP recleaning systems. Due to short filter candles (0.5 m) of the horizontal HGF design, a change in recleaning intensity over the filter candle length was neglected.
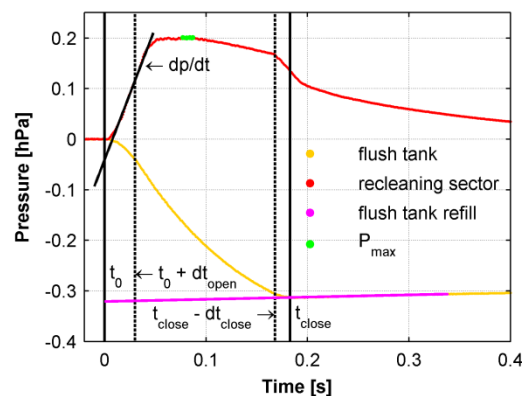
Figure 3.5: *Dynamic pressure signal with derived parameters*

Pressure maximum, pressure increase velocity and opening time were the parameters derived from dynamic pressure signals (Figure 3.5). The average of the five highest values measured in a sector during recleaning corresponded to the according pressure maximum of a sector. The pressure increase velocity (dp/dt) corresponded to the pressure increase measured 10 ms after t_0 during an interval of 25 ms. The beginning of the valve opening process t_0 was defined as $t_0 = 0$ s. t_0 was detected as the point in time when the pressure decrease in the flush tank reached 350 hPa s^{-1} for the first time calculated during a period of 10 ms. The beginning of the ex post t_0 detection started 0.5 s prior to the point in time when the pressure maxima in the recleaning sector was reached. Data before were neglected. The time when the valve was completely closed (t_{close}) was defined as the point in time when the flush tank pressure dropped below the extrapolation of the flush tank pressure increase during refill. To calculate the flush tank pressure in-

crease during refill, the time of pressure minima reached in the flush tank (t_{Pmin}) was needed. Eq. 3.1 to Eq. 3.3 show the calculation of the flush tank pressure increase. Figure 3.6 explains the opening time and delays due to mechanical constraints of the sliding gate valve. The actual opening time was defined as the time measured from t_0 to t_{close}.

$$\frac{dp_{ft}}{dt} = \frac{P(t_1) - P(t_2)}{t_1 - t_2}$$ Eq. 3.1

$$t_1 = t_{P_{min}} + \left(t_{P_{min}} - t_0\right)$$ Eq. 3.2

$$t_2 = t_{P_{min}} + 4 * \left(t_{P_{min}} - t_0\right)$$ Eq. 3.3

The time needed by the valve to open the sliding gate completely (dt_{open}) was determined to be 30 ms and the time to close completely (dt_{close}) 15 ms. Dynamic pressure signals were analyzed visually to determine dt_{open} and dt_{close}. dt_{open} corresponds to the time from t_0 up to the time when a constant flush tank pressure decrease was reached. The valve started to close when the constant flush tank pressure decrease started to decelerate and was completely closed at t_{close}.
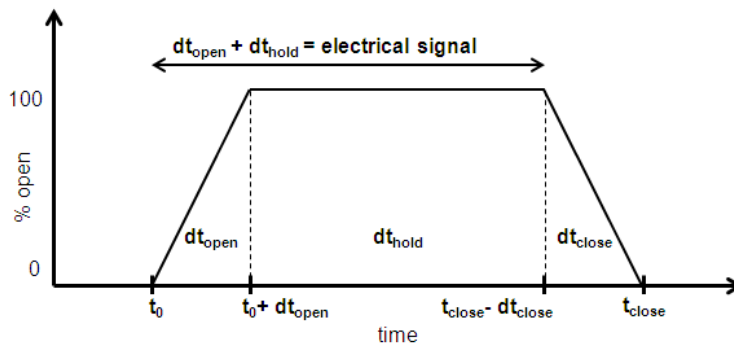
Figure 3.6: Definition of opening time, the actual opening time was defined as the time measured from t_0 to t_{close}

The visual analysis was done for several measurements and different operating conditions. Since dt_{open} and dt_{close} were independent of the flash tank pressure, operating temperature and the electronic opening time that was set, the same average values were used for all evaluations.

The maximum pressure reached in the activated recleaning sector was chosen as most relevant parameter because it is the basis to calculate the recleaning intensity. The maximum pressure could be determined easily without the need of additional parameters and was therefore a robust quantity. To compare experimental with model results it was suggested to compare the pressure maxima in the acti-

vated recleaning sector. Considering the pressure maxima only is not enough. The pressure development over time has to be considered as well as the pressure minima measured in the flush tank. The pressure increase velocity (dp/dt) has to be in the same order of magnitude since this increase is relevant for the recleaning intensity of the back pressure pulse. The flush tank minima has to be as close to the experimental result as possible because this is the precondition to reproduce the pressure development correctly. The pressure minima were the average of the five lowest values measured in the flush tank.

3.1.3.2 Experimental conditions of dynamic pressure measurements

The tests were done with (online) and without (offline) nitrogen or air flow through the filter to simulate product gas flow. Gas flows of 8.5 m^3 h^{-1} and 17 m^3 h^{-1} corresponded to HGF operation with wood gas at thermal inputs of 6.6 kW and 13.2 kW.

The results of measurements taken from new filter candles that have never been in contact with dust were taken as reference points. Once the filter candles were exposed to dust from producer gas, filter pores and filter surface could be irreversibly changed. The actual state of the filter could only be estimated by the help of pressure measurements, but no well-defined filter conditions can be claimed anymore.

Extensive testing was conducted with new filter elements of type Pall DS 10-20. Six filter candles were installed and the end of the filter element consisted of dynamic pressure switches. 203 dynamic pressure measurements were executed in cold and hot state of the filter before the filter was operated with producer gas. These measurements built the data basis for the comparison of experimental and model results (chapter 3.4.4). More than 3'000 back pressure recleaning pulses were recorded thereafter during the 230 h HGF long duration test. Measurements with the same recleaning parameters as the reference conditions were repeated after the 230 h experiment to compare the results with the new filter elements.

Dynamic pressure measurements with two other filter types were conducted. Filter elements of type Pall DS 3-20 with safety filter end were tested. Six filter elements were installed but the filter elements were not new but cleaned mechanically. New TENMAT filter elements with safety filter end were tested but only one filter element per recleaning sector was installed instead of three.

3.2 Results of long duration HGF tests

Three long term tests of 230 h, 450 h and 1150 h were conducted to confirm the long term stability of the HGF unit operated at 450 °C applying CPP recleaning system and ceramic filter candles installed in horizontal position.

3.2.1 450 h long duration test (DS 3-20, with safety filter)

Figure 3.7 summarizes the test results and the operation parameters of the 450 h long duration test. The installed filter candles Pall DS 3-20 were not new but the filter surface was cleaned mechanically. Therefore, the condition of the filter candles at the beginning of the test was not well defined as compared to new filter candles. The changes in pressure drop over time on stream can still be referenced to the condition at the beginning of the test. During the 450 h campaign the thermal input was kept constant at 6.6 kW (1.4 kg of wood pellets per hour) which corresponds to a filtration velocity of 0.6 cm s^{-1}. The recleaning frequency varied between 3 min to 12 min intervals and the recleaning pressure between 200 hPa to 1'000 hPa. The electronic valve opening time was set at 100 ms and was increased only twice to 200 ms. These parameters were varied to find the optimal operating parameters allowing a constant pressure drop over the HGF. The time interval of the soot blower cleaning pulses was shortened from 60 min to 15 min after realizing that the pressure drop of the HGF increased constantly. Additionally the valve opening time of the soot blower was increased from 300 ms to 750 ms. No filter candle regenerations were conducted.

The pressure difference from the raw gas side to the inside of the filter candle is shown by dp Filter wall. dp Filter end was the pressure difference over the closed end of the filter (safety filter end), from the recleaning sector to the clean gas sector. The total pressure drop over the filter was the sum of dp Filter wall and dp Filter end.

Figure 3.7 shows that the pressure difference over the HGF increased constantly from the beginning of the test to the end after 450 h. The pressure drop over the filter candle wall increased at a higher rate after 170 h on stream. There is no clear reason for that increase. One explanation is the coverage of filter surface by sticky patches that could be removed once the cleaning intensity was increased by higher pressure in the flush tank (190 h on stream). The recleaning intervals were extended from 6 min to 12 min after 240 h on stream. The longer intervals lead to a higher rate of pressure increase starting at 290 h on stream. Stable filter operation was impossible from that time onwards. The pressure difference over the HGF

increased at a higher rate up to 200 hPa during the last 24 h of the test. For that reason it was decided to stop the test. Table 3.4 shows the pressure difference of the HGF at different points in time. From the beginning of the campaign to the end, the pressure difference over the HGF increased by a factor of five.
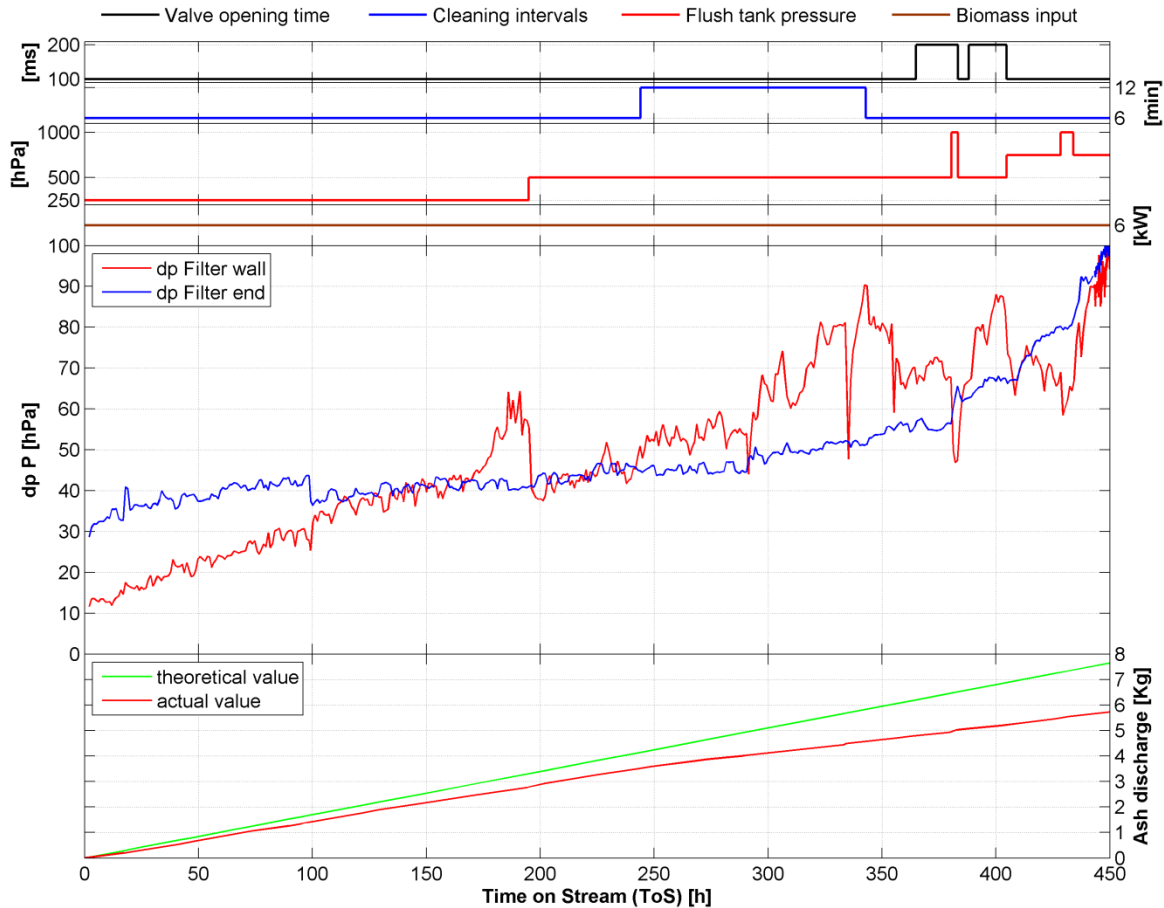
Figure 3.7: *Pressure differences of the 450 h long duration test showing different recleaning parameters and ash discharge. The pressure drop over the HGF unit increases constantly*

Time on stream	[h]	0	120	225	380	450
dp HGF	[hPa]	40	79	94	125	207

Table 3.4: *Total pressure difference over the HGF unit at different operation times during the 450 h test for thermal input of 6.6 kW. From the beginning to the end of the test the pressure difference increased by 167 hPa*

Figure 3.7 shows a constant increase of the pressure difference over the safety filter (dp Filter end). This increase between the inside of the filter candle and the clean gas sector leads to the conclusion that fine particles penetrated constantly from the raw gas side through the filter membrane to the inside of the filter candle where they accumulated causing a continuous increase of the pressure difference. The rate of pressure increase accelerated from 300 h on stream onwards. Assuming bridge building between the filter elements starting at 290 h on stream, accumulated soot and ash material between the filter candles could be the reason for a

higher transportation rate of fine particles to the inside of the filter candle. It is also possible that particles entered the recleaning sector from the raw gas sector by a leakage at the filter mount. From the recleaning area they were blown into the inside of the filter candle by back pressure pulses. Fine dust material was found at the inside of the filter candles after the filter candles were dismounted.

At the bottom of Figure 3.7, the cumulative amount of ash is shown. The theoretical values represented the calculated amount of ash that was expected to be separated by the filter. The sum of ash collected from the HGF is shown in the actual ash discharge values. The delta between the theoretical and actual value increased constantly which leads to the conclusion that there was no stable operation of the HGF. Starting at the time on stream of 250 h (beginning of 12 min recleaning intervals), the rate of ash accumulated inside the filter vessel increased.

When the filter vessel was opened after the campaign, it was observed that the whole filter vessel was filled with soot and ash. Strong bridges of soot and ash were built between the filter candles. The reason for the bridge building is not clear. Recleaning intensities that were too low could have caused patchy cleaning. Remaining patches of ash on the filter surface could be the beginning of bigger ash deposits. Longer intervals of 12 min support the growth of ash deposits if recleaning intensities are too low. However, a filter load of 9.6 g m^{-2}, corresponding to a thermal input of 6.6 kW and recleaning interval of 12 min, should not be too high.

3.2.2   1'150 h long duration test (DS 10-20, with safety filter)

New ceramic filter elements Pall DS 10-20 were installed for this long duration test. Figure 3.8 summarizes the test results and the operation parameters of the 1'150 h long duration test. The thermal input varied between 6.6 kW to 11.2 kW (filtration velocity 0.6 cm s^{-1} to 1.1 cm s^{-1}) during the 1'150 h campaign. Different cleaning intervals from 3 min to 6 min and cleaning pressures from 250 hPa to 1'000 hPa were tested to find sustainable operating parameters. The electronic valve opening time was kept constant at 100 ms. The flush tank pressure was increased to 1'000 hPa every 6 h for three recleaning cycles. The soot blower cleaning parameters were kept constant at intervals of 6 h, at valve opening times of 500 ms and at a pressure of 1 MPa during the campaign.

The pressure drop over the HGF increased at a lower rate during the 1'150 h test compared to the 450 h test. Looking at periods where the gasifier was operated with a thermal input of 6.6 kW it can be seen that the pressure drop over the HGF

unit increased by 58 hPa from 40 hPa to 98 hPa (Table 3.5). However, the increase was smaller than in the previous 450 h test (Table 3.4). From 0 h to 700 h on stream, the pressure drop over the HGF increased by 20 hPa only from 40 hPa to 60 hPa for thermal inputs of 6.6 kW corresponding to filtration velocity of 0.6 cm s^{-1}. Stable operation of the HGF could hardly be reached at thermal inputs higher than 6.6 kW and the pressure drop increased constantly. The increase of the recleaning frequency from 6 min to 3 min at 270 h on stream did not stabilize the pressure drop over the filter candle at thermal input of 11.2 kW.

Figure 3.8: *Pressure differences of the 1'150 h long duration test showing different recleaning parameters and ash discharge. For the same thermal input of 6.6 kW the pressure drop over the HGF increases by 20 hPa only in the period from 0 h to 700 h time on stream*

Time on stream	[h]	0	120	225	380	540	700	970	1130
dp HGF	[hPa]	40	46	77	57	56	60	83	98

Table 3.5: *Total pressure difference over the HGF unit at different operation times during the 1'150 h test for thermal input of 6.6 kW. From the beginning to the end of the test the pressure difference increased by 58 hPa*

The pressure difference over the filter candle decreased after regeneration procedures were conducted. The time on stream when regeneration procedures were conducted are shown in Figure 3.8 in the second graph from the bottom. The in-

fluence of regenerations can be observed best on time on stream of 50 h, 180 h, 260 h, 310 h, 460 h and 870 h.

At thermal input of 6.6 kW, pressure difference over the safety filter increased by 25 hPa only during the long duration test. This was a small increase compared to the 450 h test in Figure 3.7 where the pressure difference over the safety filter increased by 70 hPa. Therefore it was concluded that fine particles did not penetrate to the inside of the filter candle. The pressure drop over the safety filter stayed at constant level for the same thermal inputs.

At 810 h time on stream, an operational failure occurred when the ball valve of the ash discharge was not reopened. Therefore soot and ash particles were accumulated in the filter vessel for more than 48 h while raw gas kept flowing into the filter vessel. The actual values of the ash discharge showed the increase of the delta between theoretical and actual values. The delta was small and constant up to the time on stream of 800 h.

Due to this operational failure, the filter vessel was filled with dust which caused bridge building of soot and ash particles between the filter candles that could not be removed or regenerated anymore. From that time onwards, operation with stable pressure drop over the HGF was not possible anymore. For that reason it was decided to stop the test after 1'150 h on stream.

When the filter vessel was opened after the campaign, it could be confirmed that strong bridge building of soot and ash particles took place between the filter candles and the wall of the filter vessel.

3.2.3   230 hours long duration test (DS 10-20, with dynamic pressure switch)

To decrease the pressure drop over the HGF unit, dynamic pressure switches were installed at the filter end instead of safety filters. New filter candles of the same material (Pall DS 10-20) as used during the 1'150 h test were installed. Figure 3.9 shows the results of the 230 h test.

The electronic valve opening time varied between 25 ms and 100 ms. Tests presented in chapter 3.3.1 showed that an electronic valve opening time of 100 ms was enough to reach maximum recleaning intensities at flush tank pressures up to 1'000 hPa. The cleaning intervals were not set smaller than 6 min and were 15 min at maximum duration. The flush tank pressure was set to 500 hPa during most parts of the long duration test and was increased to 750 hPa and 1'000 hPa

during short periods only. Thermal input was kept constant throughout the 230 h experiment at 6.6 kW. The thermal input was interrupted only for regeneration procedures. The flush tank pressure was increased to 1'000 hPa every 6 h for three recleaning cycles of each sector. The soot blower cleaning parameters were kept constant at intervals of 6 h, at valve opening times of 500 ms and at pressure of 1 MPa for the whole long duration test.

The pressure drop over the filter end remained stable between 0 hPa and 5 hPa. Since the end of the filter candle contained the dynamic pressure switch, a very low and stable pressure drop was expected. The deviation in the data came from fluctuations of the pressure sensors as described in chapter 3.1.2.
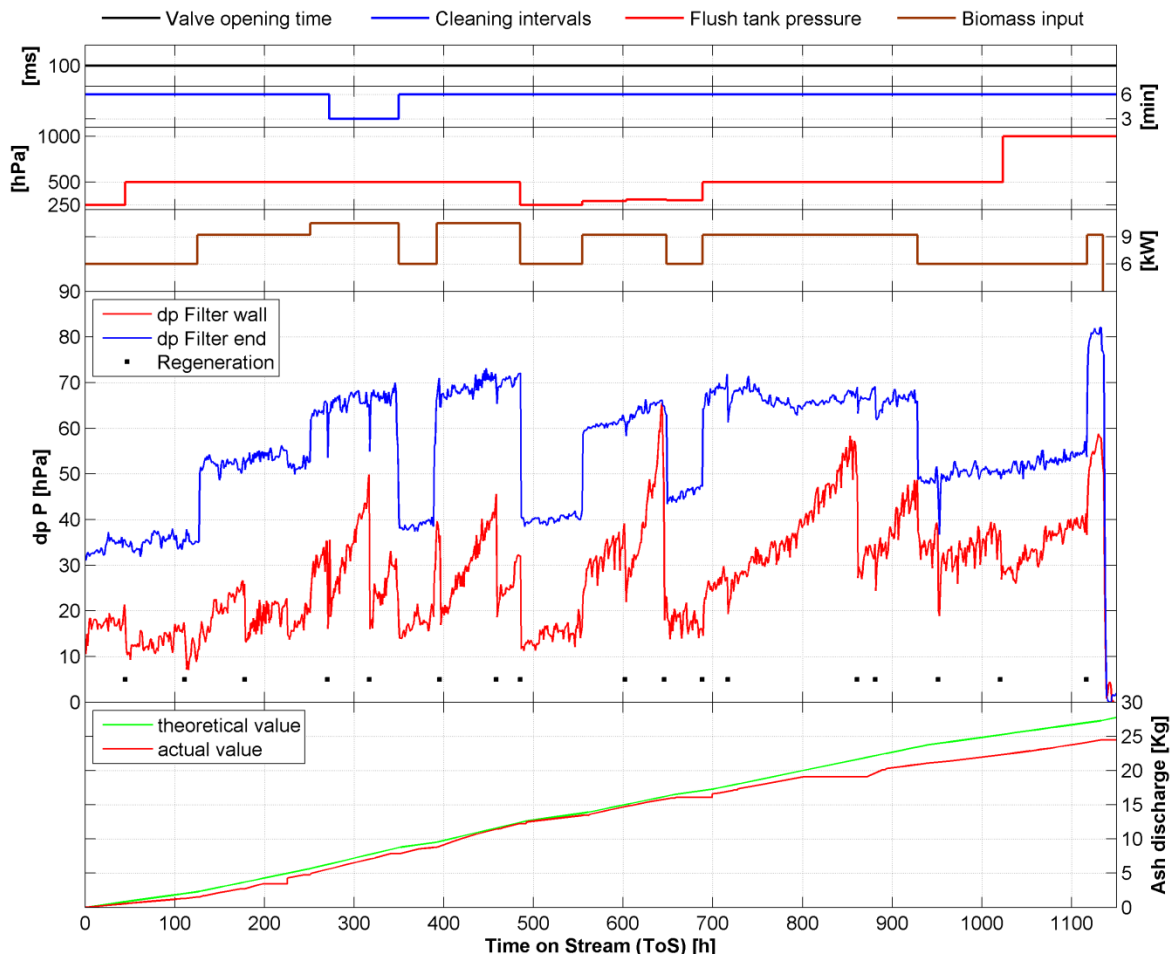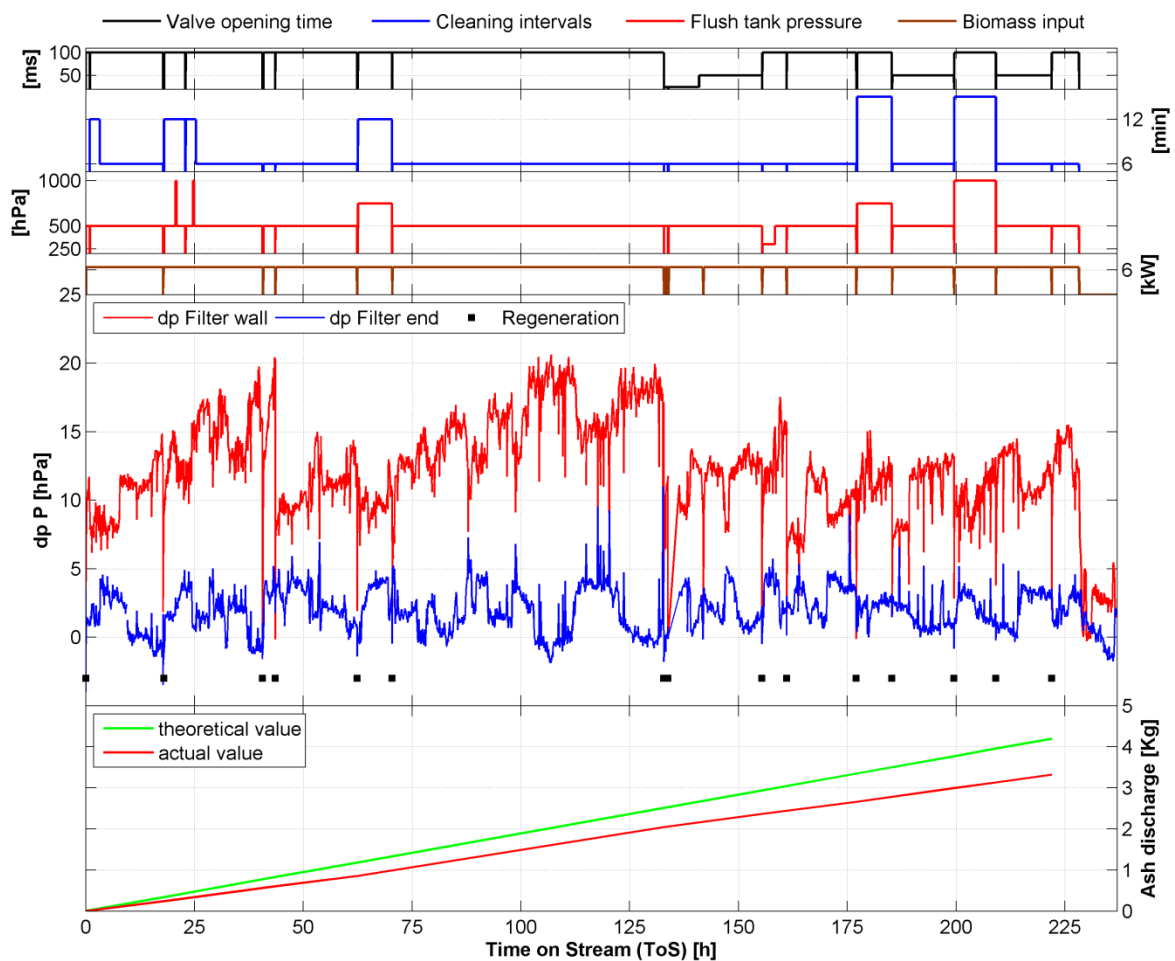

Figure 3.9: *Pressure differences of the 230 h long duration test showing different recleaning parameters and ash discharge. For the same thermal input of 6.6 kW the pressure drop over the HGF increased by 6 hPa only in the period from 0 h to 230 h time on stream*

Time on stream	[h]	0	120	225
dp HGF	[hPa]	9	18	15

Table 3.6: *Total pressure difference over the HGF unit at different operation times during the 230 h test for thermal input of 6.6 kW. From the beginning to the end of the test the pressure difference increased by 6 hPa*

The pressure drop over the filter candle wall varied between 7 hPa and 20 hPa. One can recognize that the differential pressure over the filter candle wall increased constantly between regenerations. The pressure drop decreased after regeneration to a level comparable to the level at the beginning of the experiment. From the beginning to the end of the test the pressure difference increased by 6 hPa for operation conditions of 6 kW thermal input (Table 3.6). The difference between the theoretical ash discharge value and the actual value was expected to increase until the empty space behind the two baffle plates was filled with ash. For future test, the space behind the baffle plates should be filled with inert and thermally stable material.

Pressure drop over the filter candle wall was measured at time on stream 133 h as shown in Figure 3.10. Before regeneration, a pressure drop of almost 18 hPa was measured. During regeneration with steam and air, the pressure drop decreased from over 13 hPa to 8 hPa within 1 h. Once the gasifier was started again and stable wood gas operation was established, a pressure drop below 10 hPa was measured. The regeneration caused a pressure drop reduction around 8 hPa.
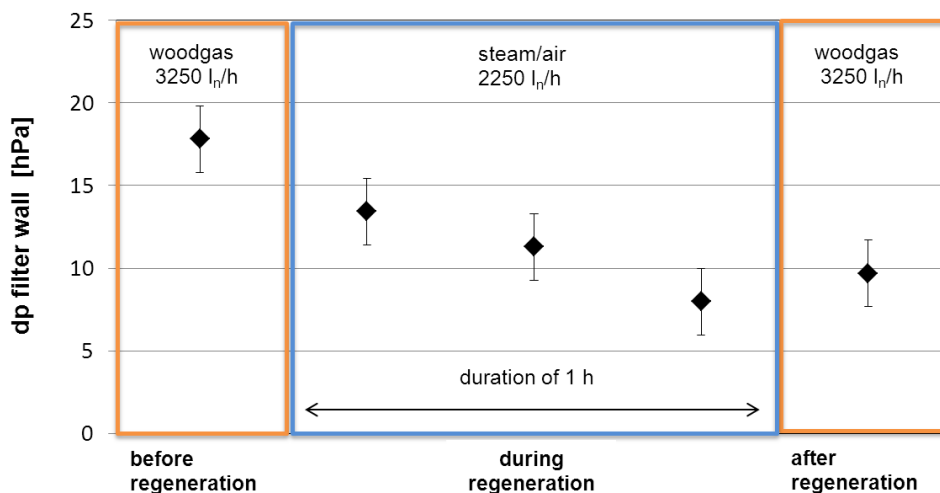
Figure 3.10: *Pressure drop measured at time on stream 133 h over the filter wall before, during and after regeneration with steam and air*

3.3 Results of dynamic pressure measurements

3.3.1 HGF commissioning with dynamic pressure measurements

Figure 3.11 shows dynamic pressure signals of a new filter candle at ambient temperature. The flush tank pressure decreased fast, once the high speed valve was opened and stopped at a lower pressure level, when the valve closed. The pressure in recleaning sector 1 increased the fastest because high speed valve 1

was opened. Therefore the recleaning sector was directly coupled to the flush tank. The right end of the filter candle directing in the clean gas sector was limited by the 5 mm opening in the metal plate and the pressure in the clean gas sector increased at slowest rate.
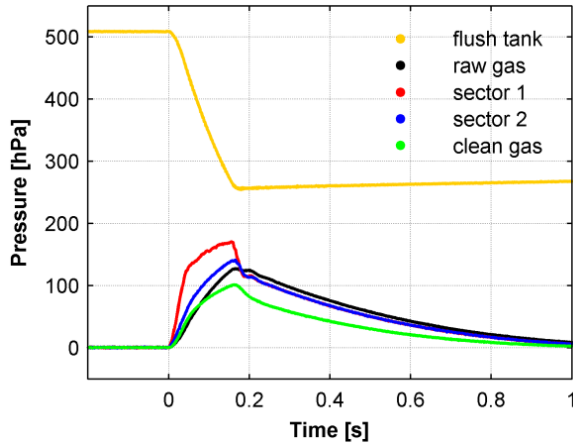
Figure 3.11: Dynamic pressure signals of new filter elements; filter state: new filters (Pall DS 10-20), filter end: dynamic pressure switch, filter temperature: ambient, filter gas flow: none, flush tank pressure: 500 hPa, valve opening time set: 100 ms, activated valve: sector 1

Apparently there was a considerable gas leakage between recleaning sector 1 and 2. For that reason the pressure in recleaning sector 2 increased faster than the pressure in the raw gas. If there would be no leakage between recleaning sector 1 and sector 2, the pressure in sector 2 would increase due to an overpressure in the raw gas sector and therefore at a slower rate than the pressure in the raw gas. The leakage between recleaning sector 1 and 2 made it impossible to clean the filter cake from one sector only. Due to the leakage, both sectors were recleaned at the same time with every back pressure pulse which corresponded to a reduction of the recleaning intervals by a factor of two. So far, no reasonable solution was found to fix the leakage between the recleaning sectors.

Evaluating the flush tank pressure signal allowed to measure the actual opening time which was longer than the electrical signal that triggers the high speed valve. Table 3.7 shows standard deviations of opening times of high speed valve 1 and 2. The results show that the electrical signal lasted most probably longer then the set time. The reason for the delay of the electrical signal has to be investigated. The influence of the opening time on the maximum pressure reached inside the filter candle is shown in Figure 3.12.

Figure 3.12 shows the dependence of the pressure maximum measured inside the filter candle of recleaning sector 1 on the actual valve opening time. Measured valve opening times higher than 75 ms were enough to reach the pressure maximum for flush tank pressures of 250 hPa and 500 hPa. At a flush tank pressure of 1'000 hPa, valve opening times of at least 100 ms were needed to reach the pressure maximum. If the valve opening time was longer than needed to reach the

pressure maximum, recleaning gas flow could be saved by choosing shorter valve opening times. A positive influence of gas flow from the inside of the filter candle to the raw gas sector, after the pressure maximum was reached, could not be observed during the tests presented here. Therefore optimal valve opening times would save operating costs due to smaller recleaning gas volumes without losing recleaning intensity.

Valve opening time set	[ms]	25		50		100		200	
Recleaning Sector		1	2	1	2	1	2	1	2
Number of measurements		5	5	6	6	33	34	6	8
Opening time measured									
Average	[ms]	79.0	79.8	111.9	106.8	176.5	173.9	283.5	272.9
Standard deviation	[ms]	6.6	5.4	4.6	9.1	7.1	10.2	4.4	8.7
P_{max} recleaning sector									
Average	[hPa]	142.3	152.6	150.1	158.6	151.8	161.3	151.8	161.2
Standard deviation	[hPa]	3.1	2.4	1.0	1.3	0.5	0.4	0.4	0.4

Table 3.7: *Valve opening time set, valve opening time measured and P_{max} recleaning sectors with standard deviations. Filter state: used grain ceramic filter candles with dynamic pressure switch after 230 h time on stream and after regeneration, filter temperature: ambient, flush tank pressure: 500 hPa, filter gas flow: none*

Standard deviations of pressure maxima measured in the recleaning sectors are shown in Table 3.7. Set opening times of 25 ms had the highest standard deviations because the opening time was too short to enable well reproducible results. Higher P_{max} were measured in recleaning sector 2. During operation, the opposite could be observed as shown in Figure 3.15 in chapter 3.3.2.
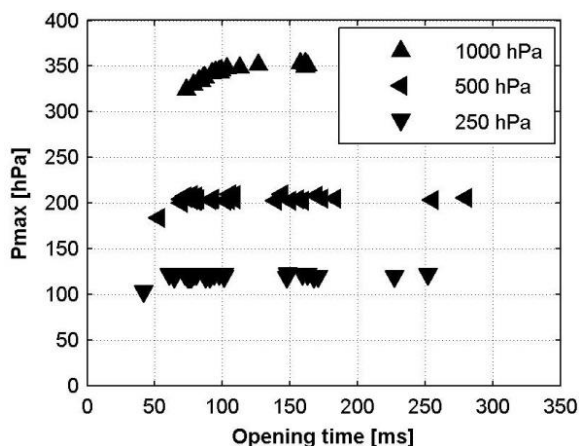
Figure 3.12: *Pressure maxima measured inside the filter candle in dependence of the actual valve opening time; filter state: new filters (Pall DS 10-20), filter end: dynamic pressure switch, filter temperature: 450 °C, filter gas flow: none, valve opening time set: 25 ms to 200 ms activated valve: sector 1*

Comparisons of dynamic pressure signals of high speed valve 1 and 2 activated can be seen in Figure 3.13. The measurements were taken at the beginning of the 230 h experiment (ToS 8.5 h). Five measurements are shown when valve1 was activated and five measurements when valve 2 was activated. The results show no difference in pressure increase velocity or maximum pressure in the recleaning

sectors. Only variance in the actual valve opening time can be observed which leads to slightly different pressure decrease behaviors.

No considerable influence of gas flow through the filter (offline and online mode) on the pressure increase velocity or pressure maxima could be observed. On average, the maximum pressure in the recleaning sectors was 4 hPa higher in the online mode (air flow of 17 m^3 h^{-1}). This difference decreased with decreasing gas flow through the filter vessel. During wood gas operation the gas flow was 8.5 m^3 h^{-1}.
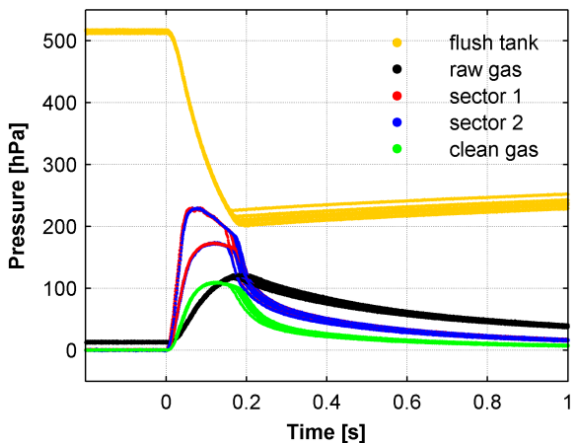
Figure 3.13: *Comparison of dynamic pressure signals of recleaning sector 1 and 2, five measurements of each sector; filter state: used filters 8.5 h ToS (Pall DS 10-20), filter end: dynamic pressure switch, filter temperature: 450 °C, filter gas flow: 8.5 m^3 h^{-1} (wood gas), flush tank pressure: 500 hPa, valve opening time set: 100 ms, activated valve: sector 1 and 2*
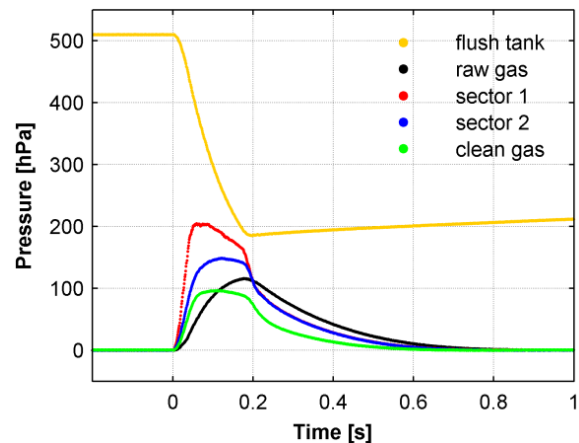
Figure 3.14: *Dynamic pressure signals at 450 °C; filter state: new filter candles (Pall DS 10-20), filter end: dynamic pressure switch, filter temperature: 450 °C, filter gas flow: none, flush tank pressure: 500 hPa, valve opening time set: 100 ms, activated valve: sector 1*

The influence of the gas temperature on pressure maxima is shown in Figure 3.14. The dynamic pressure signals were measured at a filter temperature of 450 °C. Due to a higher gas viscosity, the gas flow through the filter membrane was smaller and the maximum pressure in the recleaning sector was reached faster than at lower temperature. Once the maximum pressure inside the filter candle was reached, the pressure decreased in accordance with the decrease of the pressure in the flush tank. The pressure in the flush tank decreased faster and stopped at lower pressure at 450 °C than at ambient temperature because the density of the gas is lower at higher temperature.

3.3.2 HGF operation with dynamic pressure measurements

Each recleaning pulse was recorded with dynamic pressure measurements during the 230 h HGF long duration test. Figure 3.15 shows a 53 h range of the results from time on stream 70 h to 133 h. During the 53 h period, operating parameters

were kept constant and no filter regeneration was conducted. The actual valve opening time that was evaluated by dynamic pressure data of the flush tank is shown in the first graph on the top. One can see that the actual valve opening time was longer than the electric signal and that the difference to the electrical signal was constant.

The four graphs at the bottom of Figure 3.15 show the results from dynamic pressure measurements. The fourth graph from the bottom shows the maximum pressures that were recorded inside the recleaning sectors during back pressure pulses.

The maximum pressure of the recleaning sector with the corresponding valve opened is shown. One can see how the maximum pressure in the recleaning sectors increased between regenerations. This observation corresponded with the result of the pressure difference measurements over the filter candle wall. The maximum pressure in the recleaning sector varies depending on the change in the filter candle wall resistance.

The trend of increasing pressure can be recognized more easily with dynamic pressure data than with standard differential pressure measurements. The time interval needed to recognize the trend was shorter for the dynamic pressure data. A period of 5 h was enough to recognize a trend with dynamic pressure data. Trying to find a trend within 5 h was not possible with differential pressure data of the quality as shown in Figure 3.7 and Figure 3.8 since the fluctuations of the sensors were too high and changes of pressure drop too small. Because pressure changes recorded during recleaning pulses are one order of magnitude higher than changes of pressure recorded during normal filtration operation, the influence of the sensor noise is smaller and therefore the signal has a smaller standard deviation. For that reason dynamic pressure signals show only small fluctuations (± 0.5 hPa) compared to pressure difference signals (± 2 hPa). Better sensor equipment for pressure difference measurements will decrease fluctuations and improve signal quality.

Every six hours small interruptions can be observed followed by a lower maximum pressure in the recleaning sector. The reason for these events was the increase of the flush tank pressure to 0.1 MPa that lasted for 20 min. The higher flush tank pressure removed particles that could not be removed with lower flush tank pressure.

The third graph from the bottom shows the maximum pressure during back pressure pulses in the raw gas sector. Maximum pressure in the raw gas sector de-

creased as the maximum pressure in recleaning sectors increased. Because of the increase of the filter candle wall resistance due to patchy cleaning and depth filtration, the gas flow to the raw gas sector was decreased. Therefore, the maximum pressure reached in the recleaning sectors was higher. Respectively, the maximum pressure in the raw gas sector was lower.
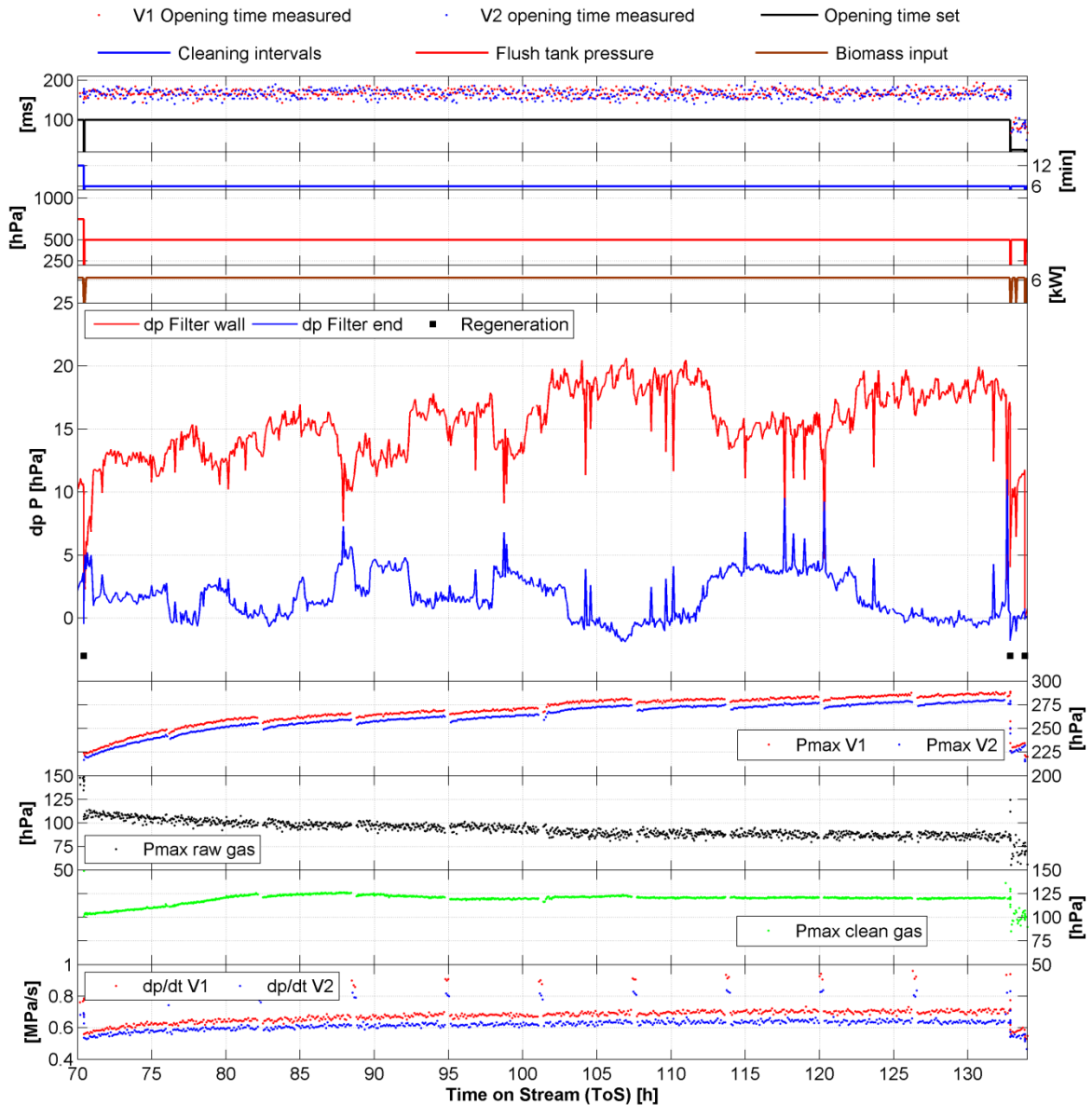
Figure 3.15: *230 h long duration test including dynamic pressure signals. Operation parameters, pressure drops, pressure maxima and pressure increase velocity over time. High pressure recleaning every 6 h for 20 min at 0.1 MPa. Soot blowers every 1 h at 1 MPa. Regenerations with steam and air without biomass input*

The second graph from the bottom shows the maximum pressure in the clean gas sector. The maximum pressure in the clean gas sector increased up to a level of 120 hPa. Higher pressure would not be reached in the clean gas sector because the dynamic pressure switch was limiting the gas flow.

The graph on the bottom shows the pressure increase velocity. The pressure increase velocity depends on the filter and high speed valve design and does not change considerably over time. A correlation with the pressure maxima in the recleaning sectors can be recognized.

More parameters could be defined to describe the filter state though most of the parameters will probably depend on the maximum pressure reached in the recleaning sector.

Looking at single dynamic pressure measurements at time on stream of 70 h (Figure 3.16), after the 53 h period, at time on stream of 133 h before regeneration (Figure 3.17) and at time on stream of 133 h after regeneration (Figure 3.18) one can see that the maximum pressure in the recleaning sector increased over the 53 h period. After regeneration comparable levels of the pressure maximum in the recleaning sectors were reached as at the beginning at time on stream of 70 h. At the end of the 53 h period, the maximum pressure in the clean gas was higher than the maximum pressure in the raw gas. The regeneration cleaned the pores of the filter material and the gas flow to the raw gas sector during back pressure pulses increased again leading to higher maximum pressure in the raw gas and lower maximum pressures in the clean gas sector.

The same comparison was done with dynamic pressure data measured at the beginning and at the end of the 230 h experiment. At the end of the experiment after regeneration an increase of 24 hPa in the maximum pressure in recleaning sector 1 remained.

For long term predictions, it is not useful to compare the new filter candle state with a later filter state. An initial filter operating time is needed in order to get a stable remaining pressure drop after recleaning. It is more meaningful to compare i.e. the signal of time on stream of 70 h with the data at time on stream of 133 h and 230 h. There was basically no increase in pressure maxima from time on stream of 133 h to 230 h and an increase from time on stream of 70 h to 230 h of 9 hPa only. The maximum pressure in the clean gas sector was higher at the end of the experiment than at the beginning. The reason for this increase was a blockage in the clean gas tube downstream of the filter vessel. This finding was confirmed by visual inspection after the experiment was finished.

After the 230 h experiment, the filter vessel was opened for visual inspection. No dust was found in the raw gas sector except behind the two baffle plates. This was expected since that was observed during previous tests. No filter cake was found on the filter candle surfaces. Therefore it can be concluded that no patchy cleaning

occurred during the 230 h experiment. No larger pieces of filter cake were found in the ash discharge during filter operation with wood gas but only small dust particles. During previous experiments, larger pieces of filter cake were found that were about 2 mm thick. For that reason, it has to be anticipated that no proper filter cake was established during recleaning intervals. The absence of patchy cleaning supports this finding. Longer recleaning intervals should be chosen to enable the building of filter cake. If there is not enough time to build a filter cake, the effect of depth filtration is mainly responsible for the increase in pressure drop over the filter candle wall.
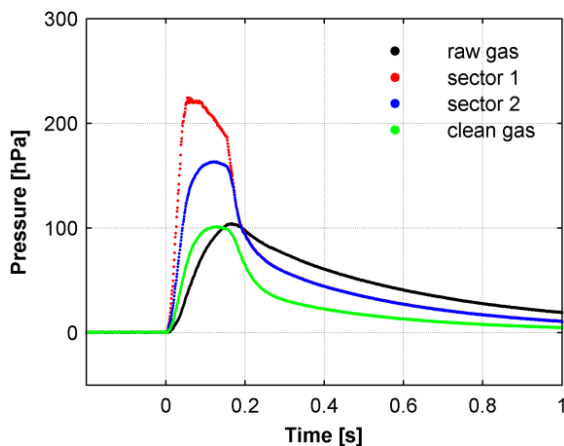
Figure 3.16: *Dynamic pressure signal; filter state: used filters after regeneration, 70 h ToS (Pall DS 10-20), filter temperature: 450 °C, filter gas flow: none, flush tank pressure: 500 hPa, valve opening time set: 100 ms, activated valve: sector 1, Pmax S1: 224 hPa*
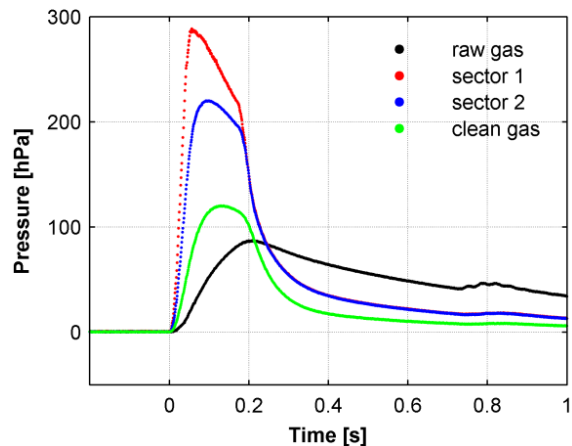
Figure 3.17: *Dynamic pressure signal; filter state: used filters before regeneration 133 h ToS (Pall DS 10-20), filter temperature: 450 °C, filter gas flow: none, flush tank pressure: 500 hPa, valve opening time set: 100 ms, activated valve: sector 1, Pmax S1: 287 hPa*
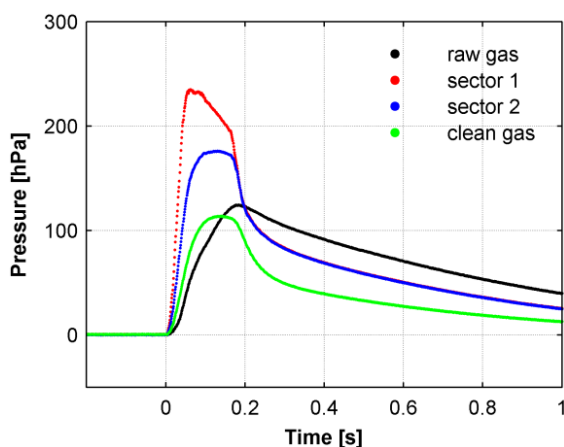
Figure 3.18: *Dynamic pressure signal; filter state: used filters after regeneration 133 h ToS (Pall DS 10-20), Filter temperature: 450 °C, filter gas flow: none, flush tank pressure: 500 hPa, valve opening time set: 100 ms, activated valve: sector 1, Pmax S1: 234 hPa*

3.4 CPP Filter model

3.4.1 Model introduction

A physical model was developed to calculate pressure evolvements in a CPP filter system during back pressure pulses. The model was based on mass conservation and calculated gas flows between sectors and gas accumulation in each sector. Knowing the volumes and the temperatures of each sector and the accumulated amount of gas, pressures in the sectors could be calculated according to ideal gas conditions (Eq. 3.4).

$$pV = nRT \qquad \text{Eq. 3.4}$$

Steady state and isothermal conditions were assumed for the time of 1 calculation step. Gas velocities during back pressure pulses generated by CPP technology are subsonic velocities (Ma < 1). For that reason energy conservation considerations are not taken into account. Gas used for back pressure pulses was N_2 and the gas coming from the gasifier was air or N_2. Regarding model calculations, it was assumed that all gas was N_2. Matlab (MathWorks Version R2012b) was used to model the recleaning pulses. Molar flows, molar balances and according sector pressures were calculated for a time interval of 10^{-5} s.

Pressures of the flush tank, recleaning, raw gas and clean gas sectors were modeled. The development of the back pressure pulse depends on the following input variables: flush tank pressure, valve opening time and filter temperature. Other important parameters are filter permeability, flow coefficient of valves (C_v-value), diameter of the dynamic pressure switch and resistance coefficients. Pressure maxima/minima, pressure increase and decrease were compared to evaluate the quality of the model.

Equations only as complex as necessary were used to describe the experimental results. Complicated equations with many variable parameters were avoided pretending precise solutions that were only parameter fitted to the specific HGF set-up used to produce the experimental data basis. Supporting the scale-up of the HGF is only possible if the model is valid for generic CPP filter designs.

Resistance assumptions are important parameters in fluid dynamics. Values derived under ideal, steady state conditions can be found in literature. Big deviations from literature data can be found under real conditions where often series of resistances follow after another and steady state conditions are not present. To find

the correct values of resistance parameters according to the specific set-up, extensive testing would be necessary. A summary of literature data and applied resistance parameters can be found in the annex in Table A.2.

The filter model presented in this thesis does not consider filter cake growth and detachment because grain ceramic filter candles used for the experiments have a permeability that is too low to measure a change in pressure drop due to the detachment of the filter cake from the filter surface [145]. Using fiber ceramic filter candles with higher permeability improves the chances to measure a change in pressure drop over the filter element due to the detachment of filter cake. The higher permeability of the filter candle wall causes a lower pressure drop and the fraction of the filter cake on the total pressure drop over the filter wall increases.

3.4.2 System boundaries

System boundaries are shown in Figure 3.19. Gas entered the system from the flush tank and from the raw gas inlet. Gas exited the system from the clean gas sector through the exit pipe. Eq. 3.5 shows the mass balance of the filter sectors.
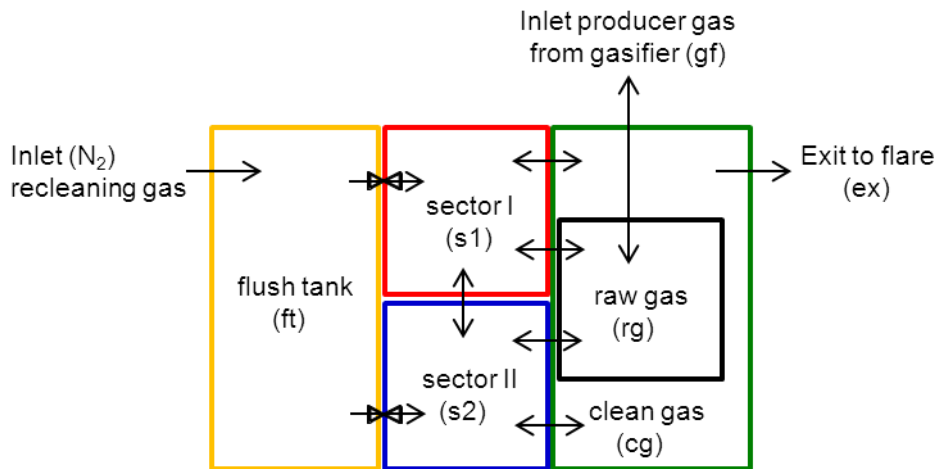
Figure 3.19: System boundaries of CPP filter model

$$0 = \dot{n}_{ftrc} + \dot{n}_{gfrg} - \dot{n}_{acc} - \dot{n}_{cgex} \qquad \text{Eq. 3.5}$$

Gas could flow in the filter vessel from the flush tank (n_{ftrc}) and from the gasifier (n_{gfrg}). The gas coming from the gasifier could be wood gas (during gasifier operation) or N_2 to simulate the gas flow of the operation with wood gas. If no gas flowed from the gasifier to the raw gas sector, i.e. during offline filter operation, the mass flow n_{gfrg} equaled zero. If gas flowed from the raw gas sector to the gasifier, i.e. during recleaning pulses, the mass flow n_{gfrg} became negative. Gas could be accumulated in the filter sectors causing an overpressure in the according sector.

Therefore n_{acc} was the sum of all accumulations in recleaning, raw gas and clean gas sectors. The gas left the system from the clean gas sector through the exit pipe to the flare (n_{cgex}).

3.4.3   Model calculations

The model calculations of back pressure pulses started with the molar flow of N_2 from the flush tank to the recleaning sector. The recleaning sector with the corresponding valve opened was called the activated sector. From the recleaning sector, the gas could flow through filter walls to the raw gas sector, through the filter end to the clean gas sector or from recleaning sector 1 to recleaning sector 2 due to the leakage between the recleaning sectors. All flows were reversible depending on the differential pressures between the sectors except a flow to the flush tank could be excluded once the valve was closed. There was unlimited volume at the end of the exit tube (flare and chimney) at ambient pressure. The calculation steps of the model were the following:

A.   molar flow calculations:

1.	flush tank	→ sector 1	(n_{ftrc})
2.	sector 1	←→ sector 2	(n_{s1s2})
3.	sector 1	←→ raw gas	(n_{s1rg})
4.	sector 2	←→ raw gas	(n_{s2rg})
5.	raw gas	←→ gasifier	(n_{rggf})
6.	sector 1 orifice	←→ clean gas	(n_{or1cg})
7.	sector 2 orifice	←→ clean gas	(n_{or2cg})
8.	sector 1 filter	←→ clean gas	(n_{fi1cg})
9.	sector 2 filter	←→ clean gas	(n_{fi2cg})
10.	clean gas	→ exit	(n_{cgex})

B.   molar accumulations:

1.	flush tank	(n_{ft})
2.	sector 1	(n_{s1})
3.	sector 2	(n_{s2})
4.	raw gas	(n_{rg})
5.	clean gas	(n_{cg})
6.	gasifier	(n_{gf})
7.	exit = 0	(n_{ex})

C. pressure calculations:
1. flush tank (P_{ft})
2. sector 1 (P_{s1})
3. sector 2 (P_{s2})
4. raw gas (P_{rg})
5. clean gas (P_{cg})
6. gasifier (P_{gf})
7. exit = ambient (P_{ex})

Eq. 3.6 was used to calculate the molar flow through the sliding gate valve from the flush tank to recleaning sector 1 or 2. For the sliding gate valve a C_v value of 26 m^3 h^{-1} was provided by the manufacturer.

$$\dot{n}_{ftrc} = 5.14 * 10^{-3} * C_v * \rho_n * \sqrt{\frac{\left(P_{ft} - P_{rc}\right) * P_{rc}}{\rho_n * T_{ft}}} * \frac{1}{M_{N_2}} * \frac{1}{3600} \qquad \text{Eq. 3.6}$$

The isentropic temperature decrease in the flush tank caused by the N$_2$ outflow was calculated according to Eq. 3.7 assuming a value of 1.4 for κ [146].

$$T_{ft_2} = T_{ft_1} * \left(\frac{P_{ft} - dP_{ft}}{P_{ft}}\right)^{\frac{\kappa-1}{\kappa}} \qquad \text{Eq. 3.7}$$

Calculating the pressure drop from the flush tank to the recleaning sectors, it started with the outflow of N$_2$ from the flush tank to the connection tube. The resistance coefficient (α_1) which describes the transition from the flush tank to the connection tube was assumed to be equal to the value of 0.25 [146]. The pressure drop was calculated according to Eq. 3.8.

$$\Delta P = \alpha * \frac{\varrho}{2} * \left(\frac{Q}{A}\right)^2 \qquad \text{Eq. 3.8}$$

The pressure drop over the connection tube from the flush tank to recleaning sector was calculated according to equation Eq. 3.9. Friction coefficients (λ) for Reynold numbers smaller than 2320 were calculated according to Eq. 3.10. The approach from Hermann [146] was used to calculate the friction coefficient for turbulent flow according to Eq. 3.11. The Hermann approach can be used for hydraulic plane tubes and Reynold numbers up to 2*10^6. Eq. 3.12 shows the calculation of Reynolds numbers.

$$\Delta P_{tu} = P_1 - \sqrt{\left(P_1^2 - \lambda * \frac{L_{tu}}{d_{tu}} * \varrho * \left(\frac{Q}{A_{tu}}\right)^2 * 2 * P_1\right)} \qquad \text{Eq. 3.9}$$

$$\lambda_{laminar} = \frac{64}{Re} \qquad \text{Eq. 3.10}$$

$$\lambda_{turbulent} = 0.0054 + \frac{0.396}{Re^{0.3}} \qquad \text{Eq. 3.11}$$

$$Re = \frac{4 * Q}{\pi * d_{tu} * \dfrac{\eta}{\varrho}} \qquad \text{Eq. 3.12}$$

Dynamic viscosity (η) was calculated at filter temperature according to Eq. 3.13 using the Sutherland constant T_S for N_2 of 117 K [146].

$$\eta = \eta_n * \frac{T_n + T_s}{T_{rg} + T_s} * \left(\frac{T_{rg}}{T_n}\right)^{\frac{3}{2}} \qquad \text{Eq. 3.13}$$

Two 90° bends were used for the connection from the flush tank to the filter vessel. The pressure drop caused by the bends was calculated according to Eq. 3.8. The resistance coefficient (α_2) for 90° bends was calculated according to Eq. 3.14 for Reynolds numbers lower than 2320. For turbulent flow, the resistance coefficient was calculated according to Eq. 3.15. The resistance coefficient equations (Eq. 3.14, Eq. 3.15) are curve fitting results of resistance values as found in [146] assuming hydraulic plane tubes.

$$\alpha_{laminar} = 124 * Re^{-0.7} \qquad \text{Eq. 3.14}$$

$$\alpha_{turbulent} = 4.5 * Re^{-0.24} \qquad \text{Eq. 3.15}$$

The branching to sector 1 or sector 2 was neglected and instead one bend was considered. The pressure drop of the tube end, after the high speed valve, where N_2 flows in the recleaning sector, was calculated according to Eq. 3.8 with resistance coefficient (α_3) of 2.0 for laminar flow and 0.85 for turbulent flow [146].

To calculate the flow between recleaning sectors, Eq. 3.16 for circular orifice was used assuming the gap between separation plate and filter vessel wall was not interrupted and of constant height and width. The formula is valid for steady state, isothermal conditions not taking into account compression of the fluid or angular

momentum. The height of the gap (L_{gap}) was equal to the thickness of the separation plate (6 mm) and the width (L_{width}) was assumed to be 0.38 mm. The area between filter vessel wall and separation plate (A_{s1s2}) was accordingly 3 cm^2. The friction factor (λ) was equal to $96*Re^{-1}$ for laminar flow with eccentricity of 1 and $r_{filter\ vessel}* r_{separation\ plate})^{-1} \approx 1$. The resistance of the entrance (α_4) was assumed to be 0.4 and the resistance of the exit (α_5) 0.7 [147].

$$\dot{n}_{s1s2} = A_{s1s2} * \sqrt{2 * \frac{(P_{s1} - P_{s2})}{\rho_{s2} * \left(\alpha_4 + \lambda * \frac{L_{gap}}{2 * L_{width}} + \alpha_5\right)} * \frac{p_{s1}}{R * T_{rc}}} \qquad \text{Eq. 3.16}$$

The dynamic pressure sensor of recleaning sector 1 was connected to the inside of a filter candle whereas in recleaning sector 2, the dynamic pressure sensor was connected to the recleaning section in front of the filter candle entrance. For that reason, it is expected that the pressure measured inside the filter candle is reduced compared to the pressure measured in the section in front of the filter candle entrance. The pressure difference from the section in front of the filter candle entrance to the inside of the filter candle is calculated according to Eq. 3.8 with a resistance coefficient (α_6) of 1.0 [146].

The flow (Q) through the filter elements was calculated based on Dacry's law for cylindrical geometries as shown in Eq. 3.17 [62]. Inertial forces are neglected in this formula as compared to the equation from Ergun [148]. Low gas velocities on the filter candle surface lead to the decision of neglecting inertial forces. A change to the equation from Ergun should be considered if gas velocities are increased due to flush tank pressures higher than 0.1 MPa or due to a reduction of the filter area by patchy cleaning. Eq. 3.18 shows the calculation of the total pressure drop (ΔP_{tot}) which equals the sum of the pressure drop over the filter wall (ΔP_{fi}) and the dust cake (ΔP_{dc}).

A permeability reduction factor (Θ) was introduced to account for a decrease in specific filter permeability K_{fi} due to depth filtration. To account for filter area reduction due to patchy cleaning, a filter area reduction factor (Ω) was introduced. These two factors are equal to a value of 1 for new filter candles.

Eq. 3.19 shows the calculation of the molar flow from the recleaning sectors to the raw gas sector. The same equation was used to calculate the molar flow from the recleaning sectors to the clean gas sector if the filter candle end was a closed end acting as safety filter. Geometric factors (G_{fi}, G_{dc}) account for the cylindrical filter elements (Eq. 3.20, Eq. 3.21).

$$\Delta P = \frac{1}{K} * \eta * \frac{Q}{A} * \frac{d_o}{2} * \log\left(\frac{d_o}{d_i}\right)$$

Eq. 3.17

$$\Delta P_{tot} = \Delta P_{fi} + \Delta P_{dc} = \frac{G_{fi}}{K_{fi} * \Theta} * \eta * \frac{Q}{A_{fi} * \Omega} + \frac{G_{dc}}{K_{dc}} * \eta * \frac{Q}{A_{dc} * \Omega}$$

$$= \left(\frac{G_{fi}}{K_{fi} * \Theta * A_{fi} * \Omega} + \frac{G_{dc}}{K_{dc} * A_{dc} * \Omega}\right) * \eta * Q$$

Eq. 3.18

$$\dot{n}_{rcrg} = \frac{(P_{rc} - P_{rg})}{\eta * \left(\frac{G_{fi}}{K_{fi} * \Theta * A_{fi} * \Omega} + \frac{G_{dc}}{K_{dc} * A_{dc} * \Omega}\right)} * \frac{P_{rg}}{R * T_{rg}}$$

Eq. 3.19

$$G_{fi} = \frac{d_o}{2} * \log\left(\frac{d_o}{d_i}\right)$$

Eq. 3.20

$$G_{dc} = \frac{d_{dc}}{2} * \log\left(\frac{d_{dc}}{d_o}\right)$$

Eq. 3.21

To calculate the flow through the dynamic pressure switch at the end of the filter candle from recleaning sectors 1 and 2 to the clean gas sector, Eq. 3.22 was used describing a Carnot-Diffusor. The resistance α_7 was calculated according to Eq. 3.23. The contraction number ($\psi_1 = 0.61$) can be found in [146] and is depending on the ratio (A_{or}/A_{di}) of the orifice area (A_{or}) and the area given by the inner filter diameter (A_{di}).

$$\dot{n}_{rccg} = A_{or} * \sqrt{2 * \frac{P_{rc} - P_{cg}}{\rho_{cg} * \alpha_7}} * \frac{P_{cg}}{R * T_{cg}}$$

Eq. 3.22

$$\alpha_7 = 1.5 * \left(1 - \frac{(1 - \psi)}{\psi}\right)^2$$

Eq. 3.23

Eq. 3.22 was also used to calculate the molar flow from the raw gas sector to the gasifier and from the clean gas sector to the exit pipe. The resistance coefficient (α_8) which describes the transition from the filter vessel to the raw gas inlet or clean gas exit tube was assumed to be equal to 0.25 [146].

To calculate the flow resistance in the tubes from the raw gas sector to the gasifier (ΔP_{gf}) and from the clean gas sector to the exit (ΔP_{ex}), wall friction of the tube and

installed inertial filter were taken into account ($\Delta P_{tot} = \Delta P_{tu} + \Delta P_{if}$). An inertial filter tube with an inner diameter of 1.4 cm was installed that was needed to protect the gas sampling system from particulate matter. A bend (90°) of the tube from the clean gas sector to the exit was neglected. The pressure drops over the length of tubes (ΔP_{tu}) and inertial filters (ΔP_{if}) were calculated according to Eq. 3.9 to Eq. 3.12.

3.4.4 Comparison experimental and model results

Data of chapter 3.3.1 build the experimental basis of the physical model and allow comparing model results with experimental results. To compare experimental results with model results, the following variables were inputs for the model calculations: HGF temperature, flush tank pressure, valve opening time and filter gas flow.

3.4.4.1 New Pall filter DS 10-20 with dynamic pressure switch
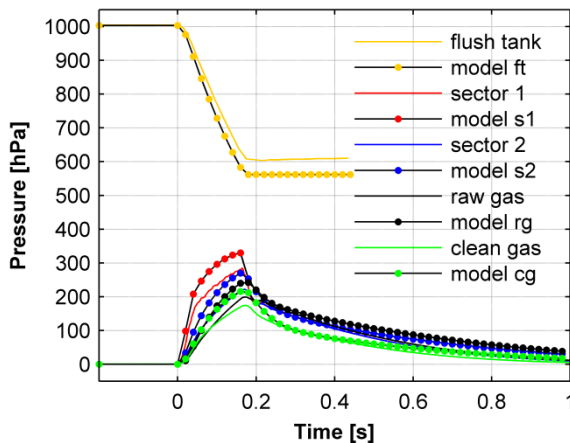
Figure 3.20: Comparison of experimental and model results with C_v-value of 26 m^3 h^{-1}; filter state: new filter candles (Pall DS 10-20), filter end: dynamic pressure switch, filter temperature: ambient, filter gas flow: 8.5 m^3 h^{-1}, flush tank pressure: 1000 hPa, valve opening time set: 100 ms, activated valve: sector 1

Figure 3.20 shows a comparison of experimental and model results. Graphically it can easily be decided whether flush tank minima, pressure increase velocities and pressure maxima are matched by the model calculations or not. Pressure maxima of the model in sector 1 was 49 hPa too high and the flush tank pressure too low by 38 hPa. dp/dt of sector 1 of the experiment was measured to be 4850 hPa s^{-1} and the model results showed 6450 hPa s^{-1}.

Table 3.8 shows a comparison of experimental and model results. The deviation between experimental and model data was calculated according to Eq. 3.24. To interpret a comparison of experimental and model results correctly, it is needed to include results of the flush tank minima and pressure increase velocities as well.

		Opening time set / Flush tank pressure	Offline: 0 m³ h⁻¹			Online 8.5 m³ h⁻¹			Online: 17 m³ h⁻¹		
		[ms] / [hPa]	250	500	1000	250	500	1000	250	500	1000
ac	cold (ambient)	50	6.7	13.0	25.8	3.9	12.0	23.5	4.7	12.6	24.6
		100	6.8	6.7	17.7	3.6	5.9	15.4	4.0	6.1	17.2
	hot (450°C)	50	7.7	13.6	21.3	9.2	13.2	21.3	10.5	16.2	19.4
		100	7.1	13.9	19.1	7.6	13.5	19.1	11.3	15.9	18.3
ft	cold (ambient)	50	1.9	2.1	5.0	1.1	2.8	4.9	1.8	3.0	5.2
		100	2.3	2.2	6.3	2.2	3.6	6.5	4.4	4.0	7.3
	hot (450°C)	50	1.3	3.7	7.6	2.5	3.9	6.6	1.1	4.0	6.3
		100	3.8	1.4	4.2	4.3	0.8	5.0	2.6	0.3	8.1
dp/dt	cold (ambient)	50	5.2	12.8	25.4	7.3	19.1	22.3	7.9	19.2	31.3
		100	3.9	17.8	24.4	8.5	19.7	25.2	8.3	18.5	31.9
	hot (450°C)	50	11.6	33.9	62.2	12.5	34.6	61.8	12.2	38.9	60.8
		100	11.5	35.8	70.4	9.9	34.8	55.5	13.0	38.4	59.5

Table 3.8: *Deviation [%] of experimental and model dat, C_v-value = 26 m³ h⁻¹*

$$Deviation = \left(\frac{Model\ result}{Experimental\ result} - 1\right) * 100 \quad [\%] \qquad \text{Eq. 3.24}$$

The model provided the best fit for flush tank pressures of 250 hPa regarding activated sector, flush tank pressure and pressure increase velocity. Deviations of the minimum flush tank pressure were 0.3 % to 8.1 % and of the activated sector 3.6 % to 25.8 %. The higher the pressure in the flush tank was the higher were deviations of the experimental data. For that reason the model was adjusted according to the pressure set in the flush tank. The parameter most appropriate seemed the C_v-value. C_v-values are measured e.g. according to VDI 2173 [149] at steady state conditions. However, during the back pressure pulse, no steady states conditions were reached at any point in time. Changing the C_v-value summarized deviations of steady state conditions and resistances of the connections tubes and bows which were assumed to have plane surfaces for the model calculations (chapter 3.4.3).

Figure 3.21 shows the sensitivity of the model results regarding the C_v-value. An increase of 20 % of the C_v-value results in a 7.0 % increase of the pressure maximum in the activated sector. A 20 % decrease of the C_v-value reduced the pressure maximum by 9.3 %.
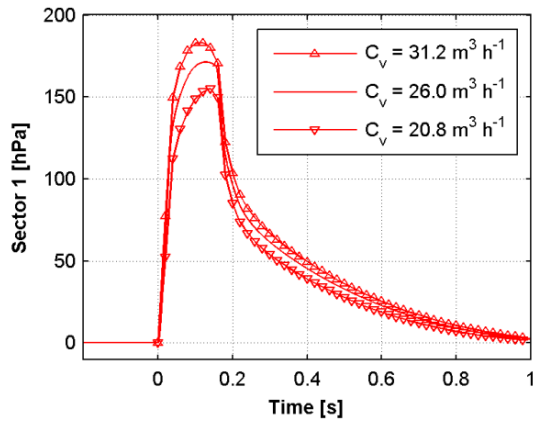
Figure 3.21: Sensitivity of pressure measured in sector 1 to different C_v-values; filter state: new filter candles (Pall DS 10-20), filter end: dynamic pressure switch, filter temperature: ambient, filter gas flow: none, flush tank pressure: 500 hPa, valve opening time set: 100 ms, activated valve: sector 1

Table 3.9 shows the comparison of experimental and model data with optimized C_v-values adapted to the pressure in the flush tank. The optimized C_v-values were 26 m^3 h^{-1} for 250 hPa, 23 m^3 h^{-1} for 500 hPa and 21 m^3 h^{-1} for 1000 hPa. The C_v-values were fitted to get the best result regarding pressure minima in the flush tank (ft) and maximum pressure in the activated recleaning sector (ac). The pressure maxima/minima are shown for all sectors, including pressure increase velocity (dp/dt) and recleaning intensity (rci) (Table 3.9).

The CPP recleaning model was able to match experimental data of Pall 10-20 filter elements with a dynamic pressure switch at the end of the filter candle with an overall average accuracy of 93 % for the activated recleaning sector. For the model result of the maximum pressure in the activated sector to be meaningful, the minimum flush tank pressure has to be as close to the experimental results as possible. The model matched the minimum flush tank pressure by 2.4 % on average.

Experimental results at small gas flow (8.5 m^3 h^{-1}) were matched better by the model than conditions without gas flow (offline) or at high gas flow (17 m^3 h^{-1}). Deviations of the activated sector were in the range of 1.0 % to 11.3 %. At temperature of 450 °C the model results did not fit as well as at ambient temperature. Average deviations of the model results compared to the experimental results were 5.0 % for the activated sector at ambient temperature and 9.1 % at 450 °C. The smallest deviation of 1.0 % was found at flush tank pressures of 500 hPa, ambient temperature and opening time of 100 ms. Highest deviations of the activated sector were found for 250 hPa flush tank pressures at a temperature of 450 °C and gas flow of 17 m^3 h^{-1}.

High deviations from the experimental data can be found in the recleaning intensity because two model parameters were needed to calculate it, i.e. pressure maximum in the activated recleaning sector and the pressure maximum in the raw gas sector have to match in maximum and point in time.

		Opening time set / Flush tank pressure	Offline: 0 m³ h⁻¹			Online 8.5 m³ h⁻¹			Online: 17 m³ h⁻¹		
		[ms] / [hPa]	250	500	1000	250	500	1000	250	500	1000
ac	cold (ambient)	50	6.7	5.9	9.2	3.9	4.7	7.3	4.7	5.2	8.2
		100	6.8	3.1	5.4	3.6	1.5	3.6	4.0	1.0	4.6
	hot (450°C)	50	7.7	8.0	10.6	9.2	7.6	11.0	10.5	10.5	9.4
		100	7.1	8.3	9.0	7.6	7.9	9.1	11.3	10.3	8.5
s1	cold (ambient)	50	9.5	9.4	15.0	6.0	7.9	12.2	6.1	7.6	11.6
		100	7.4	3.9	8.3	2.8	3.0	5.3	1.9	1.8	7.8
	hot (450°C)	50	8.5	11.0	16.8	9.6	9.7	17.4	10.0	12.7	14.0
		100	7.8	9.9	12.1	8.0	8.1	9.1	11.0	10.0	9.2
s2	cold (ambient)	50	8.2	7.9	11.2	5.1	6.7	8.8	5.7	7.0	11.0
		100	6.5	3.3	7.4	2.6	2.2	5.4	3.4	1.0	5.7
	hot (450°C)	50	9.9	12.1	19.9	11.5	10.9	16.7	12.2	13.4	14.5
		100	10.1	11.0	10.5	10.5	9.3	14.3	12.4	10.8	9.8
rg	cold (ambient)	50	6.1	6.7	8.7	5.7	10.5	15.0	7.2	10.5	16.8
		100	7.6	6.7	6.8	5.9	3.0	6.2	2.6	1.8	9.3
	hot (450°C)	50	2.9	7.6	24.5	4.3	5.7	20.4	3.2	9.0	15.8
		100	7.4	3.9	9.0	3.5	5.6	8.1	1.6	1.7	4.5
cg	cold (ambient)	50	9.2	7.7	12.9	4.1	5.9	9.2	2.9	3.8	8.4
		100	8.5	4.1	9.5	1.0	3.3	5.9	1.4	1.8	6.3
	hot (450°C)	50	3.2	12.0	18.7	3.0	8.6	11.3	0.6	3.7	7.6
		100	2.9	12.6	12.4	1.9	5.9	7.4	1.0	0.5	2.8
ft	cold (ambient)	50	1.9	2.0	1.0	1.1	0.7	1.2	1.8	0.7	0.5
		100	2.3	2.9	1.9	2.2	1.5	1.8	4.4	1.5	0.9
	hot (450°C)	50	1.3	1.0	1.8	2.5	1.1	0.9	1.1	0.6	0.5
		100	3.8	3.3	3.5	4.3	4.2	2.6	2.6	3.6	16.8
rci	cold (ambient)	50	22.3	31.5	35.2	4.5	4.0	5.5	5.6	4.4	6.7
		100	22.0	21.3	42.1	5.3	4.6	7.5	5.4	4.2	6.6
	hot (450°C)	50	11.8	10.6	12.1	12.9	11.1	14.4	14.3	14.0	14.5
		100	11.5	10.9	12.0	11.5	11.6	14.5	14.6	14.3	14.4
dp/dt	cold (ambient)	50	5.2	3.3	6.6	7.3	9.1	3.9	7.9	9.3	11.8
		100	3.9	8.0	5.9	8.5	9.7	6.7	8.3	8.6	12.2
	hot (450°C)	50	11.6	24.6	39.6	12.5	25.4	39.3	12.2	29.3	38.4
		100	11.5	26.5	46.3	9.9	25.7	34.5	13.0	28.9	37.3

Table 3.9: *Deviation [%] of experimental and model data. C_v-values = 26 m³ h⁻¹ at 250 hPa, 23 m³ h⁻¹ at 500 hPa, 21 m³ h⁻¹ at 1000 hPa*

The maximum pressure in the raw gas sector deviated by the model results by 7.7 % on average. Deviations up to 46 % were found for the pressure increase

velocities (dp/dt) at flush tank pressures of 1000 hPa and at temperatures of 450 °C. The experiments showed pressure increase velocities around 7100 hPa s^{-1} and the model results around 9800 hPa s^{-1}. The average pressure maximum in the activated recleaning sector was 350 mbar for flush tank pressures of 1000 hPa, temperatures of 450 °C and set opening times of 100 ms. Accordingly, the pressure maximum was reached after 50 ms in case of the pressure increase velocity of the experimental data and after 35 ms in case of the model results. The deviation of 15 ms was still reasonably small despite the 50 % deviation of the pressure increase velocity.

Figure 3.22 shows a comparison of experiment and model at ambient temperature and at flush tank pressures of 250 hPa, Figure 3.23 at 500 hPa and Figure 3.24 at 1000 hPa. Deviations were highest for the highest flush tank pressure of 1000 hPa but the optimized C_v-value of 21 shows a better fit than in Figure 3.20 with a C_v-value of 26 m^3 h^{-1}.

Figure 3.22: Comparison of experimental and model results; filter state: new filter candles (Pall DS 10-20), filter end: dynamic pressure switch, filter temperature: ambient, filter gas flow: 8.5 m^3 h^{-1}, flush tank pressure: 250 hPa, valve opening time set: 100 ms, activated valve: sector 1

Figure 3.23: Comparison of experimental and model results; filter state: new filter candles (Pall DS 10-20), filter end: dynamic pressure switch, filter temperature: ambient, filter gas flow: 8.5 m^3 h^{-1}, flush tank pressure: 500 hPa, valve opening time set: 100 ms, activated valve: sector 1

At a flush tank pressure of 1000 hPa (Figure 3.24) it can be seen that a set opening time of 100 ms was not enough to reach the pressure maximum in the activated sector. At operating condition of 450 °C, a set opening time of 100 ms was enough to reach the maximum pressure in the activated sector as shown in Figure 3.12. Figure 3.25 shows the results of a flush tank pressure of 500 hPa and a filter temperature of 450 °C. While the minimum flush tank pressure of the model matched the minimum of the experimental results quite well, the maximum pressures in the recleaning sectors were too high in the case of the model results. The maximum pressures in the raw gas and clean gas sectors matched very well. To

decrease the pressures in the recleaning sectors, the flow to the raw gas and clean gas sectors should be increased. Filter permeability could be increased and orifice flow resistance decreased to better match the experimental results at elevated temperature. The goal to keep the model straightforward prevented from fitting resistance parameters to specific set-ups and conditions.
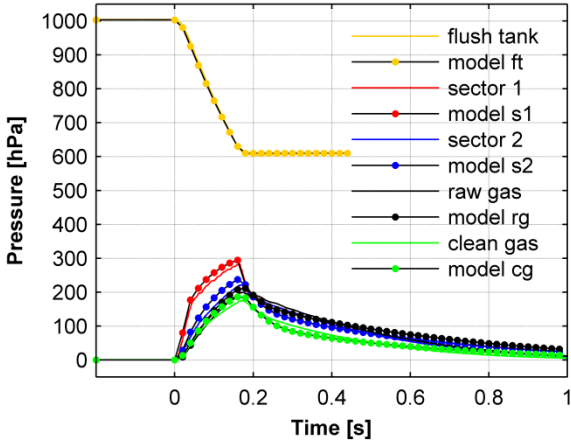
Figure 3.24: *Comparison of experimental and model results. filter state: new filter candles (Pall DS 10-20), filter end: dynamic pressure switch, filter temperature: ambient, filter gas flow: 8.5 m³ h⁻¹, flush tank pressure: 1000 hPa, valve opening time set: 100 ms, activated valve: sector 1*
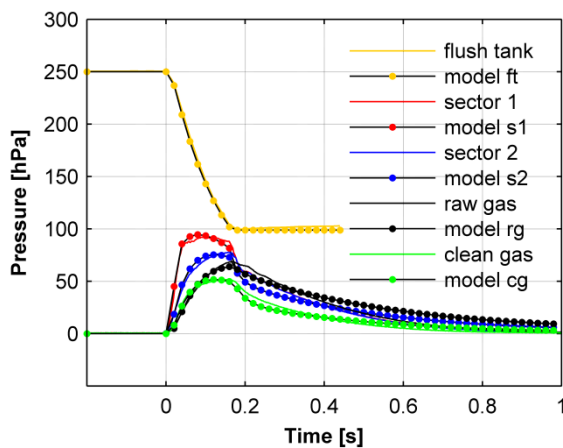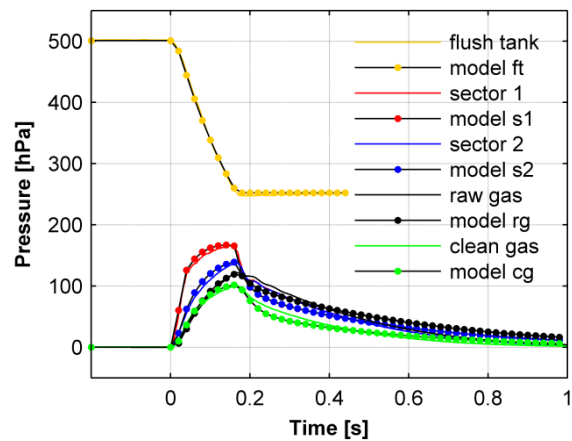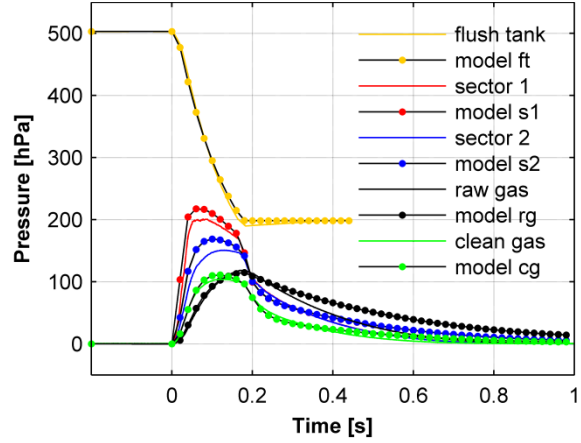
Figure 3.25: *Comparison of experimental and model results. filter state: new filter candles (Pall DS 10-20), filter end: dynamic pressure switch, filter temperature: 450 °C, filter gas flow: 8.5 m³ h⁻¹, flush tank pressure: 500 hPa, valve opening time set: 100 ms, activated valve: sector 1*
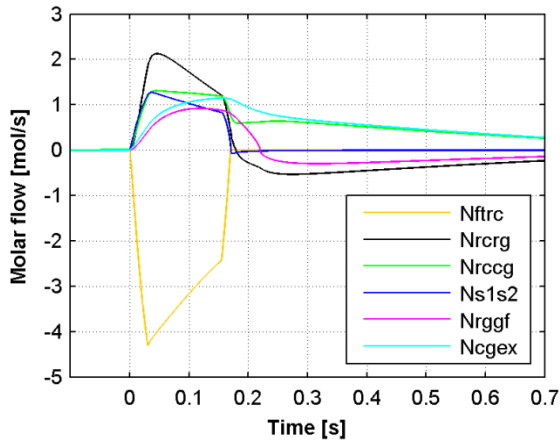
Figure 3.26: *Molar flows between different sectors; filter state: new filter candles (Pall DS 10-20), filter end: dynamic pressure switch, filter temperature: ambient, filter gas flow: none, flush tank pressure: 500 hPa, valve opening time set: 100 ms, activated valve: sector 1*
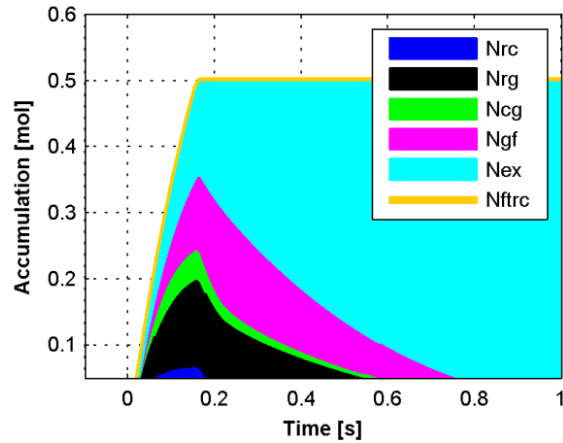
Figure 3.27: *Molar accumulation of the different sectors; filter state: new filter candles (Pall DS 10-20), filter end: dynamic pressure switch, filter temperature: ambient, filter gas flow: none, flush tank pressure: 500 hPa, valve opening time set: 100 ms, activated valve: sector 1*

The molar flows between the different sectors of the HGF as calculated by the model are shown in Figure 3.26. The flow from the flush tank to the recleaning sector is shown as negative flow. A positive flow is shown from the raw gas sector to the gasifier therefore the flow from the gasifier back to the raw gas sector is negative. All flows converged to zero once the high speed valve was closed.

The cumulative sum of moles accumulated in the different HGF sectors is shown in Figure 3.27. The cumulative sum of the flow from the flush tank to the recleaning sector increased until the valve was closed and stayed constant thereafter. All the moles flowing to the HGF system from the flush tank had to be divided to the different sectors. Until the valve closes, the accumulations in all sectors increased. Once the valve was closed, the accumulations decrease until all the gas left the system and accounts for the flow to the exit. The small amount of gas accumulated in the recleaning sector can hardly be discerned at conditions as shown in Figure 3.27. The highest amount of moles could be accumulated in the sector with the biggest volume which was the gasifier besides the exit which had unlimited volume by definition.

3.4.5 HGF simulation results

3.4.5.1 Used filter Pall 10-20 with dynamic pressure switch

Figure 3.28 shows the dynamic pressure signal measured after a 53 h time on stream (ToS) without filter candle regeneration. Model results are shown assuming initial filter conditions (filter permeability: $55*10^{-13}$ m^2). As explained in chapter 3.3.2, depth filtration was found as reason for an observed increase in pressure maxima measured in the activated recleaning sector. Depth filtration reduces pore sizes and therefore permeability of the filter elements.
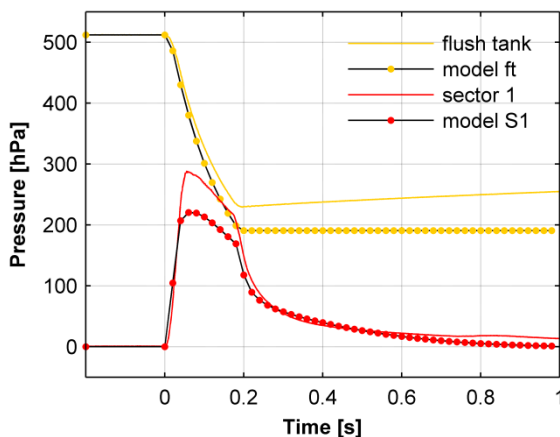
Figure 3.28: *Comparison of experimental and model results after 53 h ToS; filter state: used filters 53 h ToS without regeneration (Pall DS 10-20), filter end: dynamic pressure switch, filter temperature: 450 °C, filter gas flow: 8.5 m^3 h^{-1}, flush tank pressure: 500 hPa, valve opening time set: 100 ms, activated valve: sector 1*

The molar flow from the recleaning sector to the raw gas sector was calculated according to Eq. 3.19. The molar flow depends equally on the filter area and the filter permeability. An increase of the pressure maxima measured in the activated recleaning sector can be caused by filter area reduction and/or pore size reduction. Without visual inspection it is not possible to discern which one of the two filter failures caused the pressure maxima increase. For the model results to

match the experimental results measured after 53 h of wood gas operation, the filter permeability had to be reduced by 70 % (filter permeability: $15*10^{-13}$ m^2).

1248 back pressure pulses were executed during the 53 h. Accordingly, each back pressure pulse reduced the permeability by 0.056 %, if the decrease in permeability was linear. After filter regeneration with air and steam (Figure 3.18) the model results matched the experimental results again with a permeability of new filter candles (filter permeability: $55*10^{-13}$ m^2).

3.4.5.2 Used Pall DS 3-20 with closed end

Figure 3.29 shows a comparison of used Pall DS 3-20 filter elements with safety filter end and simulation results. Simulation results showed pressures in the recleaning sectors and in the flush tank that were too low. The simulation results for pressures in the raw gas and clean gas sectors differed considerably from experimental results. The pressure decrease of sector 1 and 2 after the closing of the valve was slower for the experimental than for the model results.
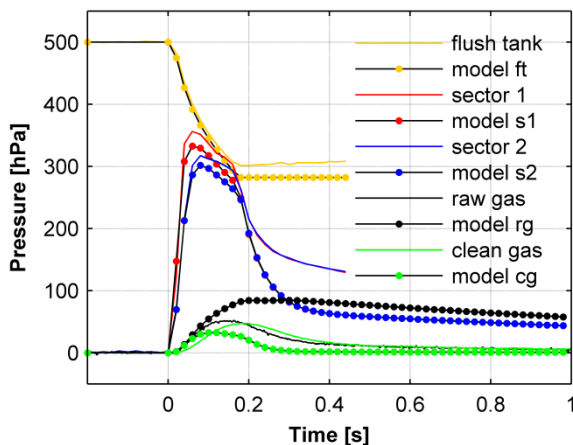
Figure 3.29: Comparison of experimental and model results of Pall DS 3-20 filter material; filter state: used filter candles (Pall, DS 3-20), filter end: safety filter, filter temperature: 450 °C, filter gas flow: none, flush tank pressure: 500 hPa, valve opening time set: 100 ms, activated valve: sector 1

The used filter material and therefore not well defined condition of the filter pores, was a reason for the deviation from simulation results that applied parameters of new filter material. The permeability of the filter material that was exposed to wood gas was reduced. Therefore, the flow to the raw gas sector was reduced and the flow to the clean gas sector increased. The simulation showed the evolvement of the pressures for a new filter candle hence a higher flow to the raw gas sector than to the clean gas sector. To reach the pressure of the experimental result in recleaning sector 1, the permeability had to be decreased by 40 % for the model calculations. The low pressure in the clean gas sector as calculated by the simulation indicates a low gas flow to the clean gas sector. The permeability of the filter material in the clean gas sector was not reduced since there was no exposure to raw gas. An improvement of safety filter end simulations is needed.

3.4.5.3 New TENMAT CS 1150 with closed end

Figure 3.30 shows a comparison of experimental results with TENMAT CS 1150 filter elements and simulation results. Applying the permeability as provided by the manufacturer and standard model assumptions, the simulation was not able to correctly calculate the pressure evolvements.
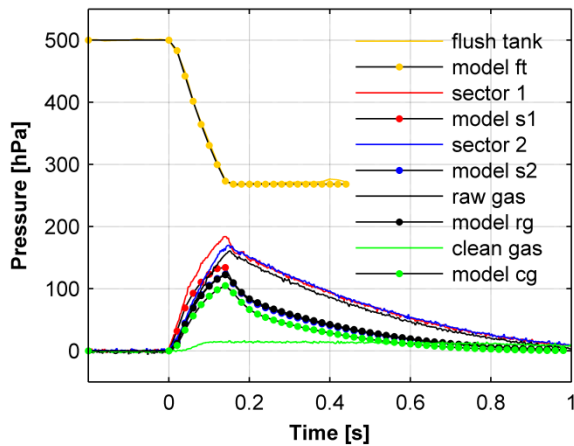
Figure 3.30: *Comparison of experimental and model results of TENMAT filter material; filter state: new filter candles (TENMAT CS 1150), filter end: safety filter, filter temperature: ambient, filter gas flow: none, flush tank pressure: 500 hPa, valve opening time set: 100 ms, activated valve: sector 1*
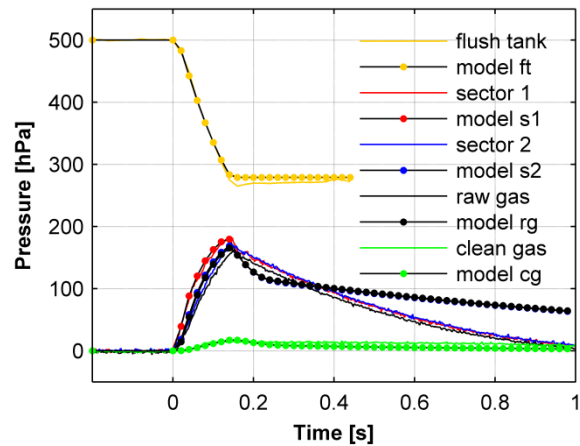
Figure 3.31: *Comparison of experimental and model results of TENMAT filter material with reduced flow through the filter end; filter state: new filter candles (TENMAT CS 1150), filter end: safety filter, filter temperature: ambient, filter gas flow: none, flush tank pressure: 500 hPa, valve opening time: 100 ms, activated valve: sector 1*

Although the pressure minimum of the flush tank was calculated correctly, the pressure maxima in the recleaning sectors and in the raw gas sector were too low. The pressure in the clean gas sector was much too high. The very low pressure as measured in the clean gas sector suggested a filter end that enables only small gas flows. The simulation predicted the maximum pressures in the filter sectors correctly if the gas flow through the filter end was reduced by 94 % (Figure 3.31). As a result, the pressure decrease was too slow after the valve was closed.

Our project partners at Karlsruhe Institute of Technology (KIT) observed a strong dependence of the filter permeability on filtration velocity for fiber ceramic filter elements. Additionally, the TENMAT filter surface and wall thickness was observed visually to be heterogeneous. To correctly reproduce the experimental results it would be needed to modify the flow through the filter end and to adjust the filter permeability according to the filtration velocity.

3.4.5.4 Simulation of new filter conditions

Figure 3.32 shows pressures in recleaning sector 1 at flush tank pressure from 50 hPa to 350 hPa. Pressure maxima that equaled roughly 50 % of the flush tank pressures could be reached. To determine the minimum pressure in the recleaning

sector that is needed to detach the filter cake from the filter candle, a model considering adhesion forces would be needed.
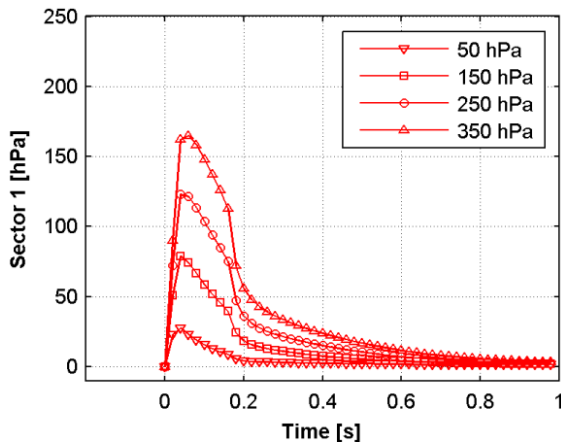
Figure 3.32: Simulation results of recleaning pressures at different flush tank pressures; filter state: new filter candles (Pall DS 10-20), filter end: dynamic pressure switch, filter temperature: 450 °C, filter gas flow: 8.5 m^3 h^{-1}, flush tank pressure: 50 hPa to 350 hPa, valve opening time set: 100 ms, activated valve: sector 1
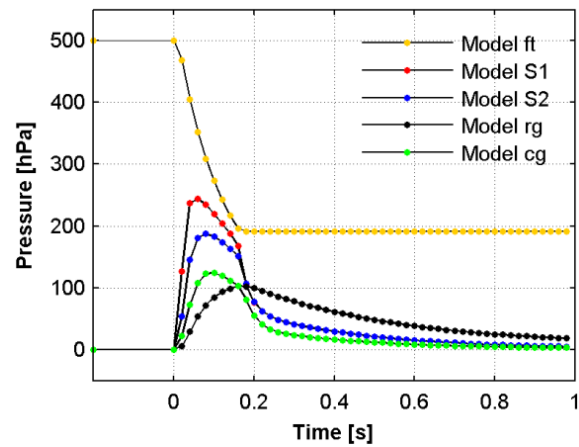
Figure 3.33: Simulation results at temperatures of 850 °C; filter state: new filter candles (Pall DS 10-20), filter end: dynamic pressure switch, filter temperature: 850 °C, filter gas flow: 8.5 m^3 h^{-1}, flush tank pressure: 500 hPa, valve opening time set: 100 ms, activated valve: sector 1

Figure 3.34: Simulation results without leakage between recleaning sector 1 and 2; filter state: new filter candles (Pall DS 10-20), filter end: dynamic pressure switch, filter temperature: 450 °C, filter gas flow: 8.5 m^3 h^{-1}, flush tank pressure: 500 hPa, valve opening time set: 100 ms, activated valve: sector 1

Figure 3.35: Simulation results with safety filter as filter end; filter state: new filter candles (Pall DS 10-20), filter end: safety filter, filter temperature: 450 °C, filter gas flow: 8.5 m^3 h^{-1}, flush tank pressure: 500 hPa, valve opening time set: 100 ms, activated valve: sector 1

Figure 3.33 assumes a filter temperature of 850 °C which is expected to be the maximum temperature that could be reached in a HGF heated solely by the heat of producer gas coming from an allothermal biomass gasifier. The pressure maxima in the activated recleaning sector (≈ 250 hPa) was higher than the maxima reached at 450 °C (≈ 210 hPa) (Figure 3.25) and the maxima reached at ambient temperature (≈ 160 hPa) (Figure 3.23). With the current HGF set-up at PSI it is not possible to operate the filter at temperatures higher than 450 °C.

Figure 3.34 shows simulation results assuming no leakage between recleaning sector 1 and 2. To reach the same pressure maxima (≈ 210 hPa) in the activated recleaning sector without leakage as with leakage (Figure 3.25), the flush tank pressure could be reduced by 33 % to 335 hPa. At a flush tank pressure of 500 hPa the pressure maxima would reach 280 hPa without leakage as compared to 210 hPa with leakage. The pressure in the recleaning sector which was not activated increases slower than the pressure in the raw gas and clean gas sector. The recleaning gas had to flow through the activated recleaning sector first, before it could flow from the raw gas and clean gas sector to the not activated recleaning sector.

The simulation results in Figure 3.35 show the pressure evolvement for filter elements (Pall DS 10-20) with the end acting as safety filter instead of a dynamic pressure switch. Compared to filters with dynamic pressure switch (Figure 3.25), the pressure maxima in the activated recleaning sector was about 6.5 % higher in the case of safety filter end. Because of the reduced gas flow to the clean gas sector, pressure in the clean gas sector was lower and pressure in the raw gas and recleaning sectors higher.

3.4.5.5 Simulation with monolith at filter element exit

Figure 3.36: Simulation results with monolith integrated at the end of the filter candle exit; filter state: new filter candles (Pall DS 10-20), filter end: safety filter, filter temperature: 450 °C, filter gas flow: 8.5 m^3 h^{-1}, flush tank pressure: 500 hPa, valve opening time set: 100 ms, activated valve: sector 1
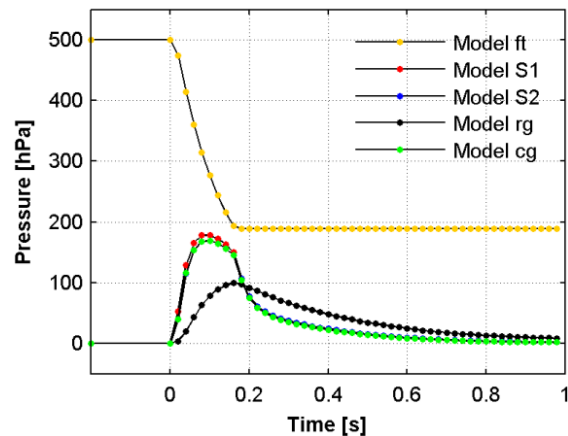
Figure 3.37: Simulation results with monolith integrated at the end of the filter candle exit, filter state: new filter candles (Pall DS 10-20), filter end: safety filter, filter temperature: 450 °C, filter gas flow: 8.5 m^3 h^{-1}, flush tank pressure: 500 hPa, valve opening time set: 100 ms, activated valve: sector 1

The option of a catalytic monolith integrated at the exit of filter elements is presented in chapter 4.6. Figure 3.36 shows simulation results regarding maximum pressure reached in the activated recleaning sector assuming monoliths at the filter candle exit with 400 cpsi and 1200 cpsi and a length of 8 cm. The diameter of the monolith (4 cm) was given by the inner diameter of the filter candle.

The pressure drop over the monolith was calculated according to Eq. 3.25 assuming steady state conditions which were not present during back pressure pulses. The difference in maximum pressure between the 400 cpsi and the 1200 cpsi monolith was only 10 hPa. To reach the same pressure in the activated recleaning sector as with a dynamic pressure switch at the end (Figure 3.25) the pressure in the flush tank would need to be increased by 15 % to 575 hPa. The maximum pressure in the clean gas sector was as high as the pressure in the recleaning sector in case of the 400 cpsi monolith (Figure 3.37). A 30 hPa pressure difference between recleaning and clean gas sector was established for the 1200 cpsi monolith case.

$$\Delta P_{monolith} = \frac{56.92}{Re} * \frac{\rho}{2} * \left(\frac{Q_{ch}}{A_{ch}}\right)^2 * \frac{L_{ch}}{d_{ch}}$$ Eq. 3.25

3.4.5.6 Simulation with foam at filter element exit

Instead of monoliths, catalytically active foams could be installed at the exit of the filter candle (chapter 4.6). Figure 3.38 and Figure 3.39 show simulation results for foam structures with 10 PPI and 65 PPI. The pressure drop was calculated according to Richardson [150]. The simulation with a 65 PPI foam showed similar pressures in all filter sectors as the reference case with the dynamic pressure switch (Figure 3.25).
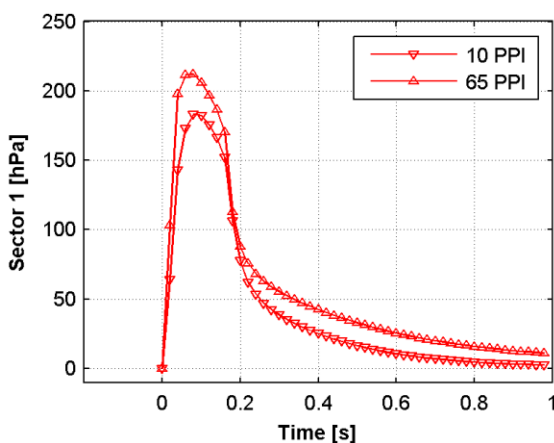
Figure 3.38: Simulation results with foam structures integrated at the end of the filter candle exit; filter state: new filter candles (Pall DS 10-20), filter end: safety filter, filter temperature: 450 °C, filter gas flow: 8.5 m³ h⁻¹, flush tank pressure: 500 hPa, valve opening time set: 100 ms, activated valve: sector 1
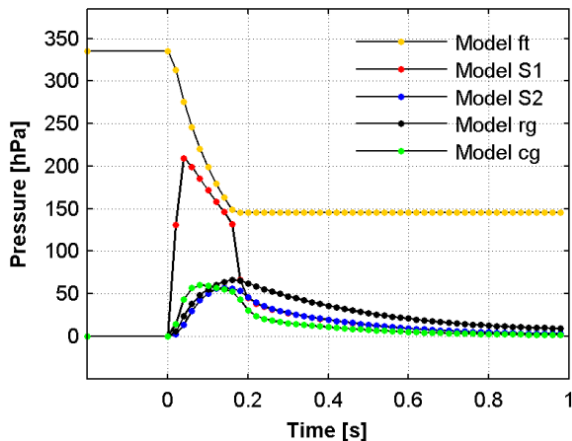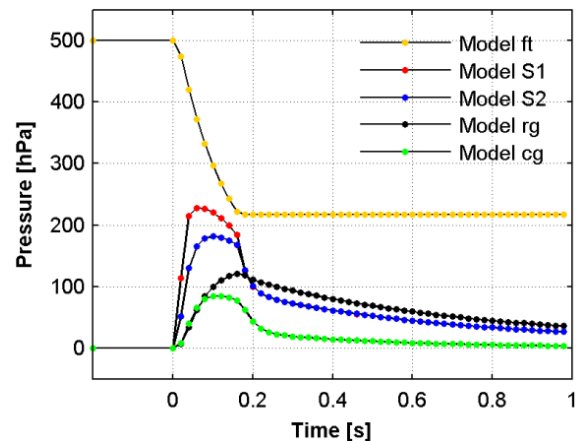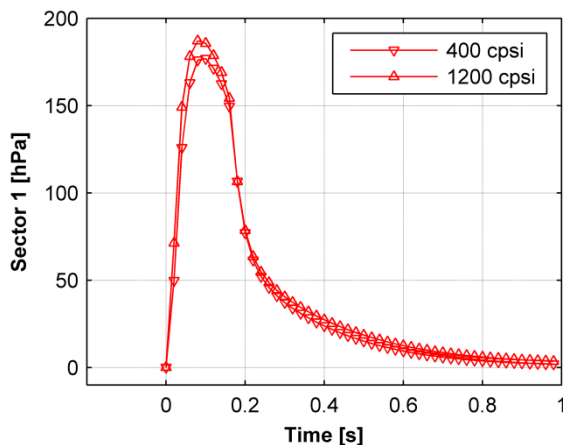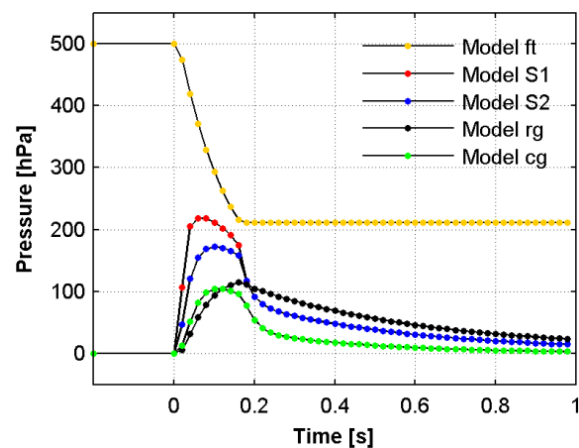
Figure 3.39: Simulation results with a 65 PPI foam structure integrated at the end of the filter candle exit; filter state: new filter candles (Pall DS 10-20), filter end: safety filter, filter temperature: 450 °C, filter gas flow: 8.5 m³ h⁻¹, flush tank pressure: 500 hPa, valve opening time set: 100 ms, activated valve: sector 1

3.5   Conclusion

## 3.5.1   Experimental results

With more than 1800 h time on stream, the concept of HGF operating at 450 °C with filter elements installed in horizontal position and a coupled pressure pulse (CPP) recleaning system was proved to be working for ash produced by gasification of woody biomass. Sustainable filtration could be demonstrated regarding pressure drop over the filter candle wall and filter end for more than 1000 h. The pressure drop over the filter unit could be kept in the range of 7 hPa to 20 hPa for 230 h.

The application of dynamic pressure switches was successful which is shown by the pressure drop over the filter end that was constant at low level and by recleaning intensities that could be reached and were high enough to clean the filter candles. Compared to the experiments implementing a security filter at the end of the filter candle, the differential pressure over the filter candle wall and filter candle end was lower by at least 30 hPa.

Dynamic pressure measurements confirmed the sustainable filter operation. Comparable filter states could be reached after regeneration throughout the experiment regarding pressure maxima in the recleaning sectors. Visual inspection of the filter vessel showed that no filter cake residues (patchy cleaning) remained on the filter candle surface. Therefore the change in filter wall resistance was due to a change in the filter permeability caused by pore size reduction (depth filtration). It can be concluded that the regenerations did counteract pore size reduction due to depth filtration. It is possible that regeneration procedures could be circumvented using steam instead of nitrogen as recleaning medium.

One of the final goals is an HGF operating at 850 °C which enables the filtration of product gases at exit temperatures of e.g. allothermal gasifiers. The application of CPP recleaning systems permits the filtration of sticky dusts at stable conditions as shown in this report where the HGF was operated at 450 °C for more than 1'800 h. The good results of these studies confirm the potential of this filter design and therefore a next generation HGF is planned operating at 850 °C.

3.5.2   Method of dynamic pressure measurements

Data of single recleaning pulses or a time series of recleaning pulses can be used to detect filter failures and changes in filter candle conditions during commission-

ing and operation. It should be considered to execute online evaluations of the data and to implement the result in the operational control. Data can be compared to reference cases and warnings will be prompted if parameters are out of a given range.

For a pilot and demonstration plant or an industrial plant, the method of dynamic pressure measurements is of interest during the commissioning phase since first measurements in the cold filter state can already give indications about the performance of the filter design (i.e. leakages, cleaning intensities, actual valve opening times). During the initial phase, the performance can be observed over time and different operating modes can be documented within a shorter time than with conventional pressure difference measurements. It has to be analyzed carefully, if permanent installation of measurement equipment at an industrial plant is of economic interest.

Looking at data of a single recleaning pulse, leakages or blockages can be detected which are undetectable by standard differential pressure measurement because the high gas flows of the recleaning pulses are needed to generate detectable pressure changes. Knowing about leakages, it can be decided whether the leakage has to be repaired or filter operating parameters have to be adapted accordingly. For example a leakage between recleaning sectors causes a reduction in recleaning intensities which can be resolved by increasing the pressure in the flush tank.

Looking at time series of parameters derived from dynamic pressure data, changes in filter candle resistance can be observed. A time series of 5 h is enough to recognize a trend in the filter candle wall resistance with dynamic pressure data. It takes 2 to 3 times longer with standard differential pressure measurements. However, the reason for changes in the filter candle wall resistance could not be evaluated on the basis of dynamic pressure signals.

To better understand dynamic pressure signals and its influencing parameters, a physical model was developed calculating the mass flows between the sectors. Modeling the mass flows can help to verify leakages, blockages and changes in filter candle wall resistance. Comparison of model with experimental results will enable the verification of the model and the detection of deviations of experimental data with the ideal model results used as reference case.

3.5.3 Physical CPP filter recleaning model

The simulation results of the CPP recleaning model showed that the model is a valuable tool which is able to support up-scaling and filter design considerations of CPP HGF systems. An overall accuracy higher than 90 % for model results compared with experimental results allows the dimensioning of a HGF. Deviations of the pressure maximum in the recleaning sector by 10 % can be compensated without high financial impacts e.g. by adjusting the pressure in the flush tank, the valve opening time or the size of the dynamic pressure switch. If the permeability needs to be adjusted it will be more expensive though still reasonable to exchange the filter elements. If major adjustments on the hard ware (valves, tubes, vessels) are needed, substantial costs have to be expected.

Comparing experimental results of used filter elements with simulation results of new filter elements showed how the model would be able to recognize filter failures caused by leakages, filter permeability reductions or blockages. Since the model is efficient regarding calculation time, it could be reasonable to integrate the model in the process control of a pilot and demonstration unit where the early recognition of filter failures is crucial and advanced analytical equipment is available.

Applying the model to other CPP filter set-ups will further improve and foster the model's capabilities. Similar CPP set-ups can be modeled by adjusting the sector volumes and geometries, lengths and diameters of tubes and filters and characteristics of the high speed valve.

4 Catalytic conversion

The results of a reformer catalyst regarding conversions of tars and sulfur containing hydrocarbons in the presence of steam, H_2S and C_2H_4 are presented in this chapter. Applied kinetics were developed allowing the modeling of this specific noble metal catalyst to simulate different operating conditions. Integration possibilities of the reformer catalyst into the HGF vessel are presented.

4.1 Experimental set-up

4.1.1 Test rig

Figure 4.1 shows the set-up of the reformer test rig consisting of two catalytic reactors, a mixing section in between the reactors and a flare to burn the gas at the end of the process.

Electric heating was used along the catalytic reactors and the mixing tube section to heat the system to desired temperatures and to compensate for heat losses (adiabatic conditions). The whole set-up was insulated to reduce temperature losses. Temperatures were measured downstream of the catalytic partial oxidation (CPO) unit (T1), up- and downstream of the monolithic reformer (T2, T3). Thermocouples (Thermocoax, K-type, 1 mm) were positioned about 5 mm away from the catalytic monolith. The temperature measured after the catalytic monolith (T3) was defined as operating temperature. The maximum temperature that could be reached in the reformer unit was 750 °C during experiments with tar addition.

The system could be operated at atmospheric pressure only. Pressure sensors were installed up- and downstream of the reformer allowing recognizing blockages of monolith channels by soot. During the experiments no blockage could be measured by the installed pressure sensors. Visual inspections of the reformer monolith after experiments confirmed clean monolith channel entrances and exits. Some soot depositions could be observed downstream of the CPO unit by visual inspections. It was assumed that the CPO of methane and air without additional steam caused soot formation.

Syngas was produced in the first reactor by catalytic partial oxidation (CPO) out of methane and air. Thermal input of methane was 2.3 kW and 4.6 kW corresponding to gas hourly space velocities (GHSV) of 9000 h^{-1} and 18'000 h^{-1} related to the

reforming catalyst. The lambda value was set at 0.29. Accordingly, 230 l_n/h of CH_4 and 637 l_n/h of air or twice the amounts were used to produce the syngas. Mass flow controllers (Bronkhorst, F-201C-FA-33-V) were used to regulate the gas flow of methane and air. CPO was operated at a constant temperature. Average temperatures of the syngas downstream of the CPO unit varied between 632 °C to 687 °C depending on the thermal input.
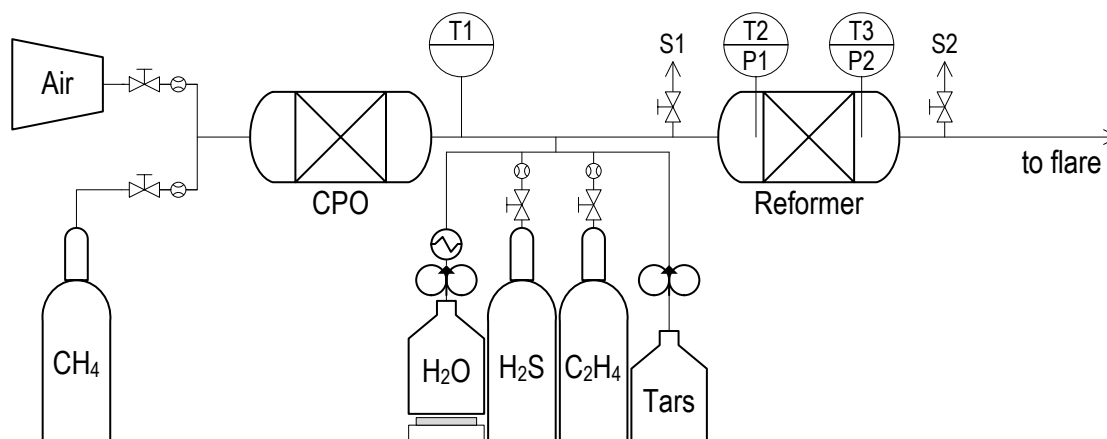
Figure 4.1: *Experimental set up of catalytic reformer unit*

Downstream of the CPO unit, steam, H_2S, C_2H_4, tar model compounds and sulfur containing hydrocarbons were added to the syngas. A syringe pump (Harvard Apparatus, PHD 2000 Infusion) was used to feed tar and sulfur compounds via a fused silica capillary (d_i of 0.5 mm) into the syngas.

Carrier	Ceramic
Chemical nature	Preparation of ceramic carrier, noble metal, Al_2O_3 and CeO_2
Diameter	5.08 cm (2 inch)
Length	7.62 cm (3 inch)
Channels	400 cpsi
Channel width	1.1 mm
Number of channels	1257
Total channel surface area	4214 cm^2
Volume	154.4 cm^3
Mass	115 g

Table 4.1: *Properties of the noble metal catalyst used for the decomposition of sulfur containing hydrocarbons*

H_2S with Ar and C_2H_4 were fed through the silica capillary as well acting as carrier gases for the tar and sulfur model compounds. First H_2S flow was controlled by bubble meter and needle valve and later by mass flow controllers. A gas bottle

with a molar fraction of 99.0 % Ar and 1.0 % H_2S was used as H_2S source. C_2H_4 flow was controlled by mass flow controller. Steam addition was regulated by a peristaltic pump (Verder, 2036 Auto) feeding continuously H_2O to a boiler followed by a super heater before added to the syngas. H_2O flow was recorded by a scale.

Following a 0.5 m long mixing section downstream of the CPO unit, the 400 cpsi, 5.08 cm by 7.62 cm (2 inch by 3 inch) catalytic reformer was installed. The composition of the noble metal catalyst is confidential and unknown to the authors. Catalyst properties are listed in Table 4.1. The same catalyst was used for all experiments.

4.1.2 Syngas

The syngas consisted of H_2, CH_4, H_2O, CO, CO_2 and N_2. Additional steam was added downstream of the CPO unit. Technical problems prevented the precise feed of steam in order to discern two cases of a high and low steam content. Steam added to the syngas was 23 ± 5 vol% for 86 % of the experiments conducted and 22 ± 10 vol% for 100 % of the experiments. GHSV values varied with steam content from 8'000 h^{-1} to 10'500 h^{-1} for the lower and from 17'100 h^{-1} to 23'200 h^{-1} for the higher GHSV.

Syngas composition measured upstream of the reformer unit without the addition of ethene, hydrogen sulfide, tars and sulfur tars can be found in Table 4.2 (average values on a dry and tar free basis). The temperature variation of the CPO unit was not high enough to discern the influence on the syngas composition. Compared to producer gas generated by gasification of wood [143], the syngas used for this study has a low concentration of CO_2.

Methane conversions measured downstream of the reforming catalyst during experiments without the addition of ethene, tar and sulfur were used as reference points. The reference points were used to confirm initial activities of the catalyst and the absence of permanent deactivation.

[vol%]	H_2	CH_4	CO	CO_2	N_2
low GHSV	30.5	1.8	15.5	2.4	45.7
high GHSV	33.4	1.0	16.1	2.6	46.2

Table 4.2: *Syngas composition for low and high GHSV measured upstream of the reformer unit without the addition of ethene, hydrogen sulfide, tars and sulfur tars (average values on a dry and tar free basis)*

4.1.3 Gas matrix

Two cases were introduced for H_2S concentrations. High H_2S concentrations of 100 ppmV and low H_2S concentrations of 20 ppmV represented cases where H_2S sorption material was applied upstream of a HGF unit, respectively not applied in the first case.

Ethene (C_2H_4) and ethyne (C_2H_2) are known to be precursors to build higher hydrocarbons or soot [137, 151, 152]. They can have a negative effect on the catalyst performance due to surface adsorption or soot formation. Ethene concentrations in producer gases vary from 0.1 % to 4.0 % [89, 153, 154]. We decided to add 2 vol% of ethene to the gas matrix during experiments with tars. 16 experiments were conducted at an ethene concentration of 1 vol% during tar and sulfur tar free conditions to investigate ethene decomposition.

Contaminants contained in the producer gases of biomass gasifiers such alkali (Na, K), chlorine (HCl) or nitrogen compounds (HCN, NH_3) were not considered in this study.

4.1.4 Tars and sulfur compounds

Tars and sulfur compounds were added to the syngas with the aim of creating a gas mixture as close to reality as possible. Depending on the kind of biomass feed and gasification technology, tar and sulfur content can vary up to one order of magnitude [143]. Harsh sampling conditions directly downstream of gasifiers often prevent a proper characterization of the producer gas. Particle filters and gas cooling is often needed before tar species can be quenched or measured. Gas cleaning devices upstream of the sampling point have to be carefully considered when comparing literature data regarding tar content of producer gas.

Many definitions of tar exist [155-157] and the variety of tar compounds found in biomass gasifiers is large [157]. Devi et al. [155] suggest five different tar classes. Tar model compounds for this study were chosen to represent the most abundant species, different tar categories and different difficulty to decompose them. The stable aromatic structure was supposed to be difficult to decompose by the catalyst. The more benzene rings a compound contains, the more difficult it is to decompose the molecular structure. This is at least valid for the model compounds benzene and toluene (tar class 3, light aromatic, 1 ring), naphthalene (tar class 4, light PAH compounds, 2 rings), phenanthrene (tar class 4, light PAH compounds, 3 rings) and pyrene (tar class 5, heavy PAH compounds, 4 rings).

The handling of benzene was avoided by the addition of the benzene content to the toluene content. Toluene was used as solvent for the other tars and sulfur compounds. Thiophene (1 ring), benzothiophene (2 rings) and dibenzothiophene (3 rings) were chosen as sulfur model compounds. Again, abundance and chemical stability were the selection criteria of the three sulfur tars. Figure 4.2 shows the tar and sulfur tar components used as model compounds in this studies.
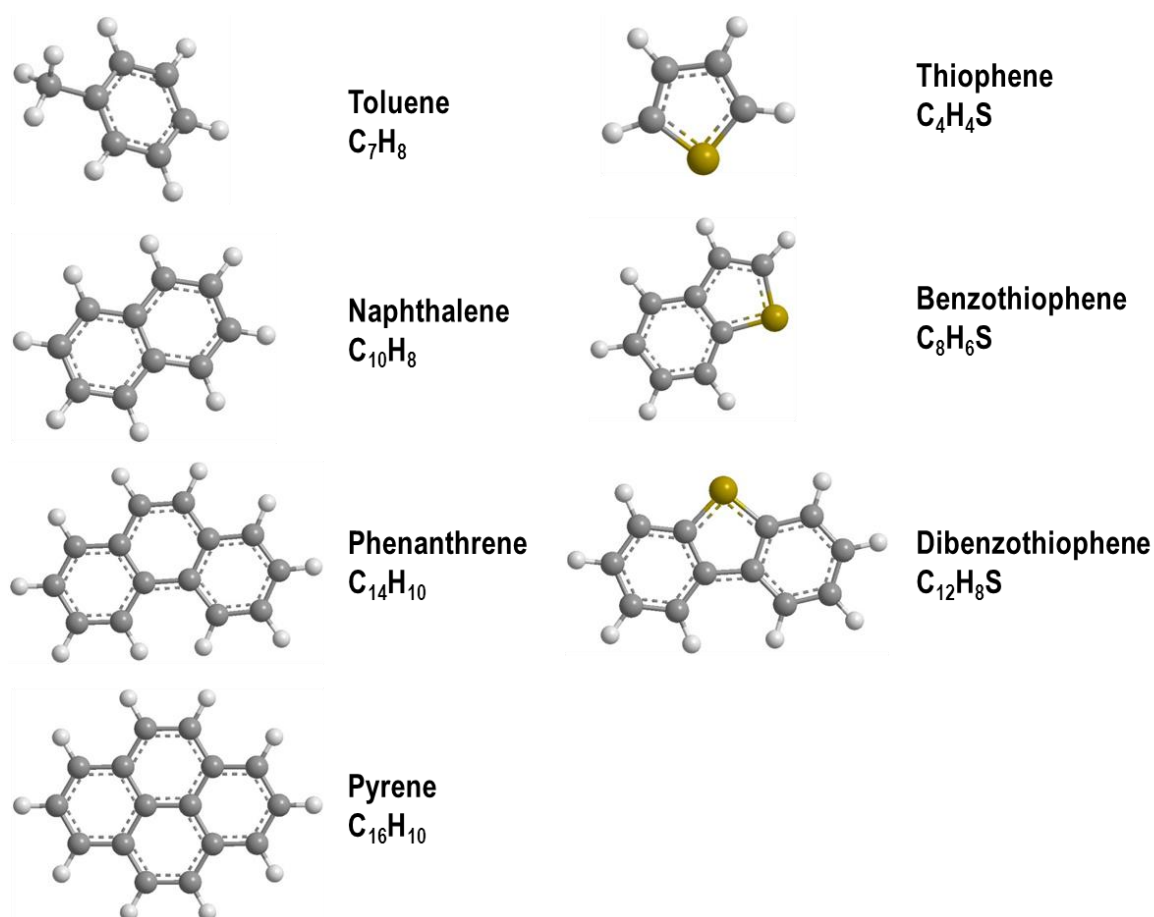
Figure 4.2: *Tar and sulfur tar model compounds used in this study*

Preceding studies did not consider sulfur tars but showed a strong dependence of tar conversions on H_2S [158]. Previous results also showed the dependence of total sulfur amount and the irrelevance of the kind of sulfur species that was added to the gas. Sulfur free experiments would help to better understand the influence of sulfur on tar conversion. Because sulfur free conditions are very unlikely to find in reality, sulfur free experiments were not conducted so far.

Two cases regarding tar and sulfur tar concentrations were discerned. High tar concentrations represented a tar-rich producer gas where no catalytically active material was applied either in the gasifier or filter. Low tar concentrations represented a producer gas with reduced tar concentrations due to applied catalytic

material e.g. as bed material or gasification technologies producing low tar concentrations.

Table 4.3 shows tar and sulfur tar concentrations of different gasifier technologies using wood as biomass input. Sampling points are specified showing the influence of scrubbers. Tar and sulfur tar concentrations of these gasifiers were the basis to decide on the toluene concentration in the syngas and the other tars in relation to toluene content. Toluene concentrations in the producer gas were 800 ppmV for the low and 2000 ppmV for the high tar concentration case.

Gasifier type	Reference	Sampling point		Thiophene	Benzothiophene	Dibenzothiophene	Toluene+Benzene	Naphthalene	Phenanthrene	Pyrene
FB	[23]	after filter	ppmV	0.91	0.14	0.06	966	80		
(without bark)			mg m_n^{-3}	3.4	0.8	0.5	3669	455		
DFB	internal	before gas scrubber,	ppmV	11.4	4.4	bdl ?				
		after filter	mg m_n^{-3}	42.9	26.2	bdl ?				
DFB	[159]	after gas scrubber,	ppmV	7.4	1.3	0.21	402	63	2.5	
		after filter	mg m_n^{-3}	27.8	8	1.7	1526	360	20	
DFB	[94]	before gas scrubber,	ppmV					862	75	
		after filter	mg m_n^{-3}					4930	595	
FB	[98]	before gas scrubber,	ppmV	1.6	0.14		2477	249	49	3.3
		after filter	mg m_n^{-3}	5.9	0.8		9408	1425	390	30
CFB	[134]	before tar reformer,	ppmV				4424	1151	211	41.4
		after filter	mg m_n^{-3}				16806	6582	1675	374

Table 4.3: *Tar content of different gasifier technologies, on a dry basis, using wood as biomass input. (FB = fluidized bed, DFB = dual fluidized bed, CFB = circulating fluidized bed, bdl = below detection limit)*

Concentrations of other tar and sulfur compounds were set in relation to the toluene concentration. Only the dibenzothiophene concentration for the low tar case was increased from 0.8 ppmV to 1 ppmV in order to stay above the limit of quantification of the analytical equipment. The ratio within the tar and sulfur components was kept constant and only the total tar load including sulfur species was varied. The concentration of single tar components would need to be changed if the influence of the single compounds on the catalyst performance would be of interest.

Table 4.4 lists the tar and sulfur tar concentrations that were added to the syngas to test the capabilities of the catalytic reformer.

Tar load		Thiophene	Benzothiophene	Dibenzothiophene	Toluene+Benzene	Naphthalene	Phenanthrene	Pyrene
low	ppmV	8	2	1	800	80	8	4
	mg m_n^{-3}	30	12	7	3039	458	64	36
high	ppmV	20	5	2	2000	200	20	10
	mg m_n^{-3}	75	30	16	7597	1144	159	90

Table 4.4: *Tar and sulfur tar concentrations for high and low tar loads*

4.1.5 Experimental planning

Temperature was expected to have the strongest influence on conversion rates. In order to accurately determine the temperature dependence of the reaction rates, experiments were conducted at three different temperatures. The lowest temperature was set at 600 °C because this was the lowest temperature expected at the exit of a biomass gasifier. The highest temperature was set at 750 °C which corresponds to the operating limits of the materials used for the experimental set up. The third temperature was chosen in the middle of the lowest and highest temperature at 675 °C.

Tar load	Gas temperature	H_2S concentration	GHSV
	[°C]	[ppmV]	$[h^{-1}]$
high	600	20	9'000
low	675	100	18'000
	750		

Table 4.5: *Operating conditions used during experiments*

Table 4.5 lists the operating parameters. 24 different operating conditions were possible according to classical factorial design. 149 experiments were conducted in total. 70 experiments were conducted without sulfur, tar and ethene addition, so called reference experiments. 25 experiments were conducted with C_2H_4 but without the addition of tars and sulfur tars to investigate ethene decomposition reactions. 54 experiments were conducted with the addition of ethene, hydrogen sulfide, tars and sulfur tars to the syngas.

4.1.6 Diagnostics

Two identical sampling systems were used to service the sampling points up- and downstream of the reformer unit in parallel (S1 and S2 in Figure 4.3). Based on

continuous liquid quench technology, it was possible to analyze the dry and tar free producer gas while collecting liquid samples containing water, tar and sulfur containing hydrocarbons.
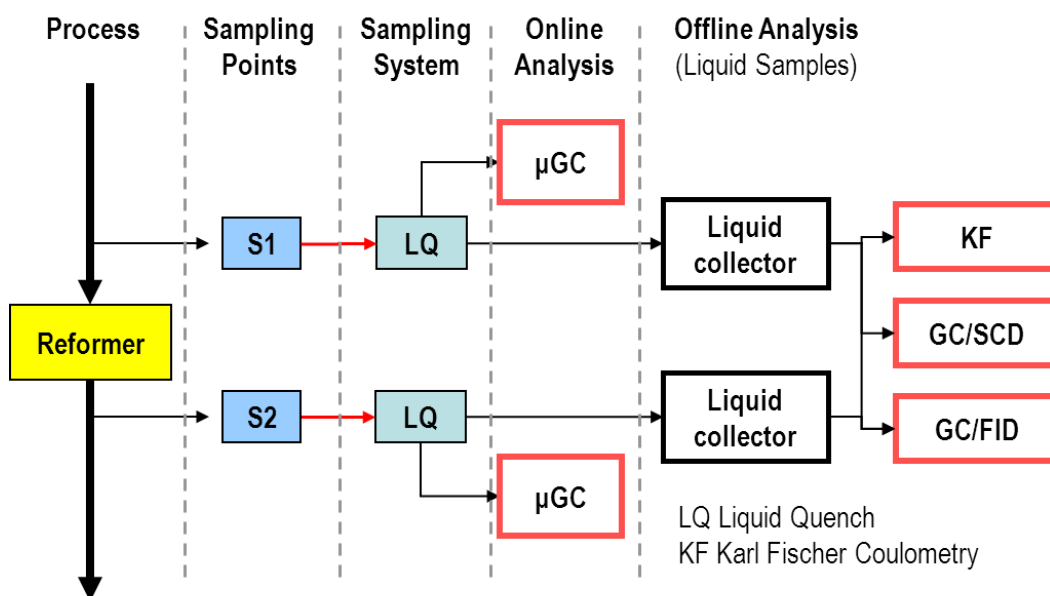
Figure 4.3: *Analytical set-up as used for the catalytic reformer tests*

1-methoxy-2-propanol was used as quenching liquid. The feed of the solvent used as quenching liquid was controlled by a rotary piston pump. The sampled gas flow was controlled by a needle valve and a membrane pump. The ratio of the sampled gas to liquid solvent volume (G/L ratio) was set at 400 to 500 during experiments with tar load. The liquid-gas mixture was cooled to a set temperature of –20 °C in a cooling coil before separation. The sampling system was operated at ambient pressure. The G/L ratio has to be considered when calculating concentrations in the producer gas out of the concentration of condensed compounds in the liquid sample. A detailed description of the sampling system can be found in Rechulski et al. [160, 161]. Liquid samples were collected during steady state conditions for a period of 15 min to 30 min. Accordingly, the liquid samples contained average information about tar, sulfur tar and water content.

A micro gas chromatograph (µGC) was used to analyze the dry and tar free sample gas stream in real time (online). The µGC (Varian CP-4900) consisted of two parallel lines enabling the simultaneous measurement of the gas up- and downstream the reformer unit. Each µGC line contained two porous layer open tubular (PLOT) capillary columns. The molecular sieve (MSA5) column was used to separate He, H_2, O_2, N_2, CO and CH_4. The porous polymer type U column (PPU) enabled the separation of CO_2, C_2H_2, C_2H_4, C_2H_6, C_3H_6, H_2S and COS. Thermal conductivity detectors (TCD) were used to quantify the compounds. Two point calibra-

tions with reference gas mixtures were implemented. The relative standard deviation of µGC quantification was below 2.0 %. The maximum time resolution of the µGC was 3 min. The average of µGC results, measured during the liquid sampling period, was used as permanent gas composition during steady state conditions. The time delay between µGC and liquid sampling system was considered.

Knowing the amount of carbon that was added to the system in form of methane and ethene, molar flows were calculated from the volumetric information of the µGC via carbon balance.

Tar species in the liquid samples were separated with a gas chromatograph (GC, Agilent GC 7890A) and quantified with a flame ionization detector (FID). An Agilent HP-5 (5 % Phenyl Methyl Siloxan) column was used to separate benzene, toluene, naphthalene, phenanthrene and pyrene. Calibration was done with solutions of known tar concentrations in 1-methoxy-2-propanol. The calibration was validated after each ten samples. The average relative standard deviation of GC/FID quantification was below 8.0 %.

Sulfur containing hydrocarbons were separated with a GC (Agilent 7890A) and quantified with a sulfur chemiluminescence detector (SCD, Agilent 355 SCD). An Agilent wall-coated open tubular (WCOT) dimethylpolysiloxane column (CP-Sil 5 CB) was used to separate thiophene, benzothiophene and dibenzothiophene. Calibration was done with 1-methoxy-2-propanol solution of known sulfur compound concentrations. The calibration was repeated after twelve samples. The average relative standard deviation of GC/SCD quantification was below 12.5 %.

The water content in the liquid samples was quantified with a Karl-Fischer coulometer (KF, Metrohm KF-Coulometer 737 series 01). The relative standard deviation of KF coulometry quantification was below 1.5 %. If the water content was not measured by KF coulometry (i.e. 44 out of 149 experiments), the information of the scale was used to determine the water feed rate. The steam content downstream of the reformer was calculated by oxygen balance.

Limits of detection (LOD) of the analytical equipment have to be considered because of the low tar and sulfur tar concentrations in combination with high conversion rates. The maximum detectable conversion (MDC) is limited by the LOD and therefore not 100.00 %. Table 4.6 shows LOD of the GC/SCD and GC/FID for liquid samples and producer gas. The LOD of the liquid samples is independent of the sampling system and valid for each experiment. The LOD of the producer gas depends on the G/L ratio and had to be considered for each experiment. According to the LOD and the G/L ratio, the maximum detectable conversion (MDC) rate

can be determined for each experiment. The ranges of MDC's are presented in Table 4.6. The lowest MDC range showed benzothiophene because it was the least abundant sulfur tar compound in the syngas.

		LOD liquid sample		LOD producer gas	MDC
		µg ml^{-1}	ppmV	ppbV	[%]
GC / SCD	C$_4$H$_4$S	0.1088	0.13	64 - 76	98.26 - 99.56
	C$_8$H$_6$S	0.0809	0.06	30 - 35	97.33 - 99.38
	C$_{12}$H$_8$S	0.1086	0.06	29 - 35	93.77 - 98.72
GC / FID	C$_6$H$_6$	0.0416	0.05	-	-
	C$_7$H$_8$	0.0446	0.05	24 - 28	99.9942 - 99.9983
	C$_{10}$H$_8$	0.0233	0.02	9 - 11	99.9816 - 99.9947
	C$_{14}$H$_{10}$	0.0243	0.01	7 - 8	99.8607 - 99.9596
	C$_{16}$H$_{10}$	0.0259	0.01	6 - 8	99.7208 - 99.9087

Table 4.6: *Limits of detection (LOD) in the liquid sample and in the producer gas and maximum detectable conversions (MDC) of GC/SCD and GC/FID as determined during the experiments conducted in this study*

4.2 Experimental results

Figure 4.4 shows the equilibrium composition of the syngas including gas concentrations measured up- and downstream of the reformer unit during reference experiments.
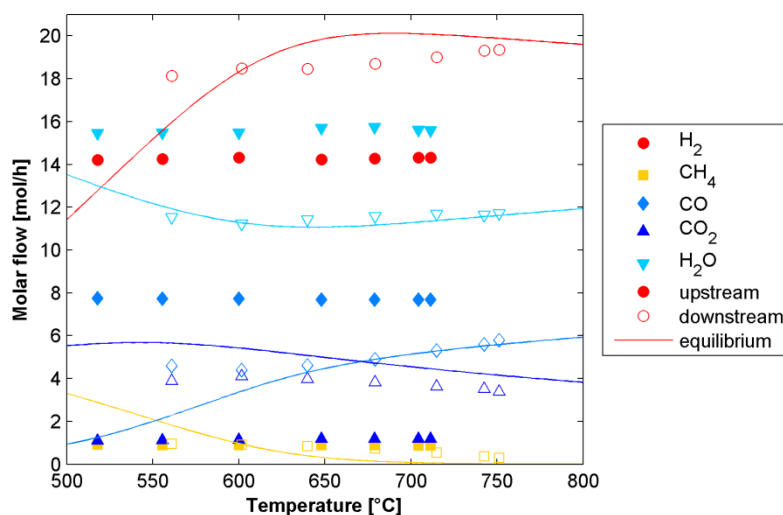
Figure 4.4: *Equilibrium composition of the syngas including gas concentrations measured up- and downstream of the reformer unit during reference experiments*

Equilibrium calculations were conducted with HSC Chemistry 5.1. It can be seen that the reformer catalyst produced a syngas composition closer to equilibrium than the syngas composition upstream of the reformer. H$_2$ reaches almost equilib-

rium composition at highest temperatures of 750 °C. Equilibrium calculations show CH_4 contents smaller than 0.1 % at temperatures higher than 690 °C. CH_4 decomposition started at 680 °C. H_2O reaches equilibrium concentrations at temperatures of 550 °C to 750 °C. CO concentrations downstream of the reformer were close to equilibrium concentration starting at 640 °C. Concentrations of CO_2 measured downstream of the reformer were shifted close to equilibrium concentrations by the catalyst but did not reach equilibrium at any temperature.
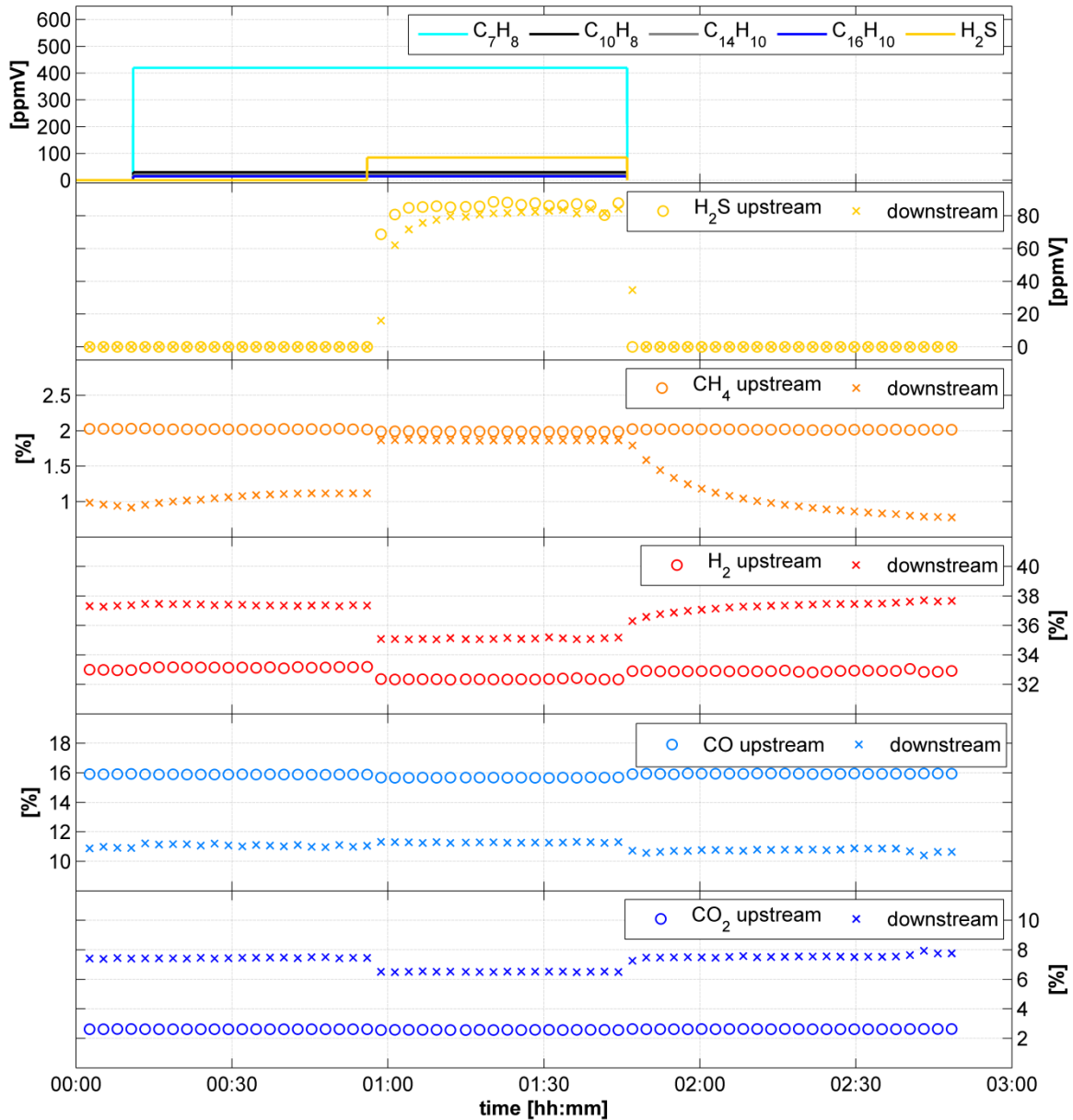
Figure 4.5: *Dependence of methane conversion on the addition of sulfur free tars and H_2S*

Strong dependence on the sulfur content was found for methane conversion. In Figure 4.5 the concentration of H_2, CH_4, CO, CO_2 and H_2S up- and downstream of the reformer is shown over time. The first graph shows the amount of toluene, naphthalene, phenanthrene, pyrene and H_2S added to the tar and sulfur free syn-

gas. During the time where only tars and no sulfur were added to the system, the concentration of CH_4 measured downstream of the reformer was roughly 1 vol% lower than the concentration upstream of the reformer.

Methane concentration downstream of the reformer increased from 1.1 vol% to almost 2 vol% once H_2S was added to the system. After H_2S supply was stopped, CH_4 concentration downstream of the reformer decreased to concentrations lower than measured during the addition of tars. The increase of methane concentration downstream of the reformer during the addition of H_2S was assumed to be caused by adsorption of sulfur on active sites. Desorption of sulfur species on the catalyst surface and recovery of the catalyst activity for CH_4 decomposition started once the H_2S supply was stopped.

Figure 4.6 to Figure 4.14 present the conversions of tars and sulfur tars at temperatures of 600 °C to 760 °C, different GHSV, water content, tar load and H_2S concentrations. An overview of the experimental conditions can be found in Table 4.5. Conversions (X_i) of species (i) were calculated according to Eq. 4.1, where (F_i) represented molar flow.

$$X_i = \frac{F_i^{in} - F_i^{out}}{F_i^{in}} \qquad\qquad \text{Eq. 4.1}$$

Conversions of sulfur containing hydrocarbons (41 % to 99.6 %) were on average higher than conversions of sulfur free tars (0 % to 47 %). High temperature, low GHSV, low steam and sulfur content favored high conversions of tars and sulfur tars. The ranges of conversion for low and high GHSV can be found in Table 4.7.

Conversion [%]		low GHSV	high GHSV
Thiophene	C_4H_4S	60 - 99.6	41 - 99.6
Benzothiophene	C_8H_6S	86 - 99.3	65 - 99.4
Dibenzothiophene	$C_{12}H_8S$	86 - 98.5	17 - 98.8
Benzene	C_6H_6	nd	nd
Toluene	C_7H_8	1 - 47	0 - 23
Naphthalene	$C_{10}H_8$	0 - 11	0 - 9
Phenanthrene	$C_{14}H_{10}$	0 - 30	0 - 17
Pyrene	$C_{16}H_{10}$	0 - 17	0 - 11

Table 4.7: Conversion ranges of tars and sulfur tars at low and high GHSV (nd = not detected)

Conversions of sulfur free tars were in the range of 0 % to almost 50 % (Figure 4.6 to Figure 4.9). Negative conversions (building of tars) were measured in some cases but not illustrated. It is assumed that the building of PAH's was unlikely and

the apparent higher content of tars was measured due to sampling and analytical inaccuracies. Further investigations and improvements of the analytical set up are needed. A dependence of conversion rates on temperature could be observed. Highest conversions were measured for low GHSV. Steam content higher than 25 vol% combined with high GHSV results in conversions lower than 15 %. At lowest temperatures around 620 °C, conversions of tars were lower than 13 % for any experimental conditions. The highest conversions of 47 % could be measured for toluene at temperatures above 700 °C, low GHSV and at toluene content of 800 ppmV. Naphthalene conversions were below 12 % for any temperature and experimental condition. The deviation between measurements was higher than the influence of the operating parameters. For that reason, no clear dependence of the conversion on sulfur content, steam content, GHSV and tar load can be distinguished.

Benzene could be measured downstream but not upstream of the reformer catalyst. It is assumed that the methyl group of toluene was separated from the benzene ring by the catalyst. Therefore benzene was built from toluene. Accordingly the conversion of toluene did not equal the decomposition of the benzene ring. The selectivity of toluene to benzene varied between 0 % and 44 % for temperatures around 620 °C and between 48 % and 100 % for temperatures higher than 680 °C. Benzene formation could also result from decomposition of hydrocarbons that are higher in molecular mass than toluene. Hydrocarbons of lower molecular mass than pyrene, might be formed out of higher molecular hydrocarbons [156, 162].

Conversions of sulfur containing hydrocarbons were on average higher than conversions of tars (Figure 4.10 to Figure 4.12). Zero conversion of sulfur tars could not be observed. Concentrations of sulfur containing hydrocarbons downstream of the reformer were often undetectable with the sampling and analytical system that was used. An apparent full conversion resulted. In Figure 4.10 to Figure 4.12 the highest conversions equaled the limit of detection of the GC/SCD adjusted by the according G/L-ratio of the sampling system (see chapter 4.1.6). Lowest conversions were measured at high GHSV and low temperature for any of the three sulfur species. At temperatures higher than 680 °C, lowest conversions were measured for operating conditions with high GHSV, high amount of steam and H_2S.

Overall, dibenzothiophene showed the lowest conversion of 17 %. Even at lowest temperatures around 620 °C the limit of detection was reached at low GHSV for any of the three sulfur tars. At low GHSV and low H_2S concentration, the LOD of thiophene and benzothiophene was reached at any temperature and therefore the

lowest conversions were equal or higher than 98.4 % for thiophene and 97.5 % for benzothiophene. At low GHSV, conversions were higher than 43 % for dibenzothiophene, 86 % for benzothiophene and 60 % for thiophene. Influence of the amount of tar (high/low) could not be determined.

Figure 4.13 shows the conversion of ethene measured during experiments with tar and sulfur tars added to the syngas. Highest conversion over 90 % was measured at high temperature, low GHSV and low tar load. At high GHSV the conversion was below 75 % at any temperature. At temperatures of 620 °C the maximum conversion was 40 % measured for low GHSV, low tar load and low H_2S concentration. At temperatures higher than 680 °C, the conversion was higher than 20 % for any operating condition.

There are different possibilities of ethene decomposition reactions. Ethene could be hydrogenated to ethane (Eq. 4.2) and ethane could be decomposed to methane (Eq. 4.3) by further reactions with hydrogen. A direct methanation of ethene could be considered as well (Eq. 4.4). Steam reforming of ethene is a third possible reaction (Eq. 4.5). Since gas concentration of methane was not varied, it was not possible to discern the amount of methane produced by the decomposition of ethene and ethane (Eq. 4.3 and Eq. 4.4).

Regarding the reaction pathway from ethene to ethane by hydrogenation and further from ethane to methane by hydrogenation, the concentration of ethane measured downstream of the reformer was smaller than the deviation of ethene concentration. Therefore it could not be determined how much ethene reacted to ethane and further from ethane to methane. The amount of ethane measured downstream of the reforming catalyst corresponded to about 6 % of the converted ethene amount.

$$C_2H_4 + H_2 \rightarrow C_2H_6 \qquad\qquad \text{Eq. 4.2}$$

$$C_2H_6 + H_2 \rightarrow 2CH_4 \qquad\qquad \text{Eq. 4.3}$$

$$C_2H_4 + 2H_2 \rightarrow 2CH_4 \qquad\qquad \text{Eq. 4.4}$$

$$C_2H_4 + 2H_2O \rightarrow 2CO + 4H_2 \qquad\qquad \text{Eq. 4.5}$$
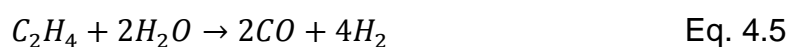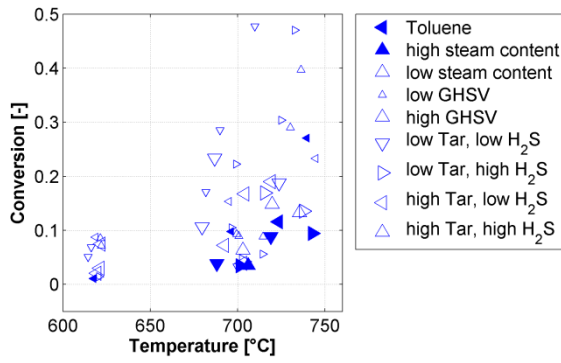
Figure 4.6: Toluene conversion
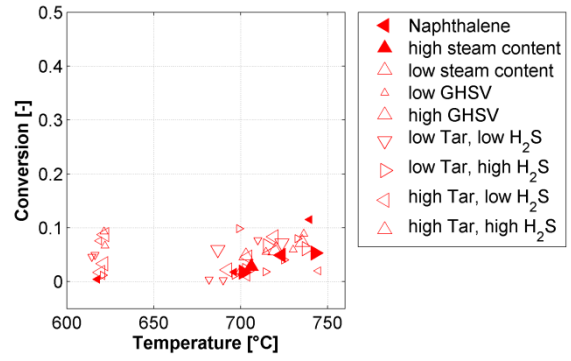
Figure 4.7: Naphthalene conversion
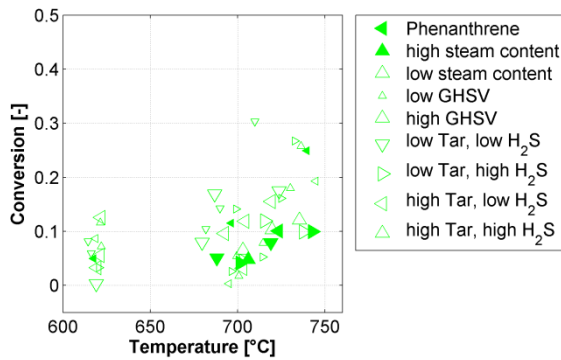
Figure 4.8: Phenanthrene conversion
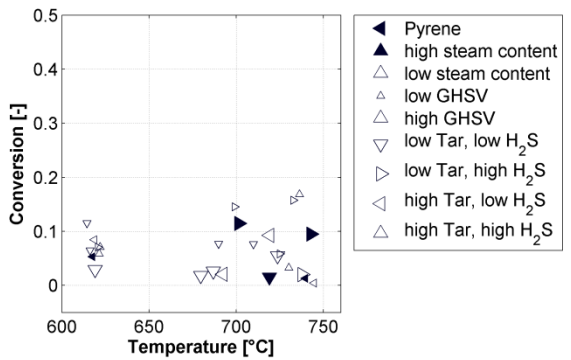
Figure 4.9: Pyrene conversion
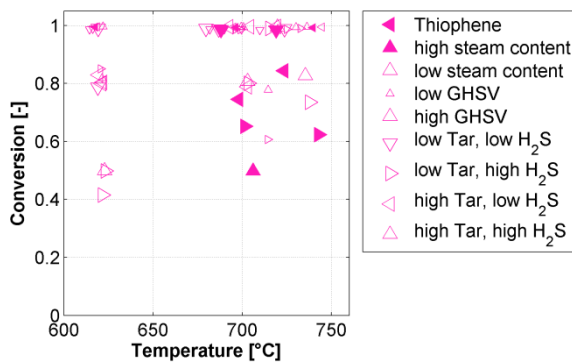
Figure 4.10: Thiophene conversion
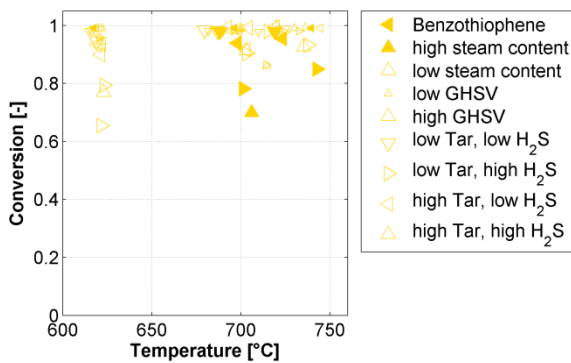
Figure 4.11: Benzothiophene conversion
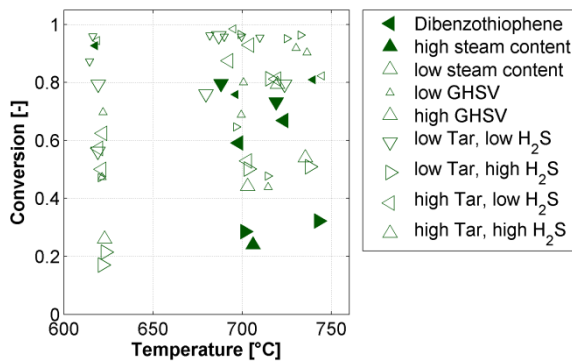
Figure 4.12: Dibenzothiophene conversion
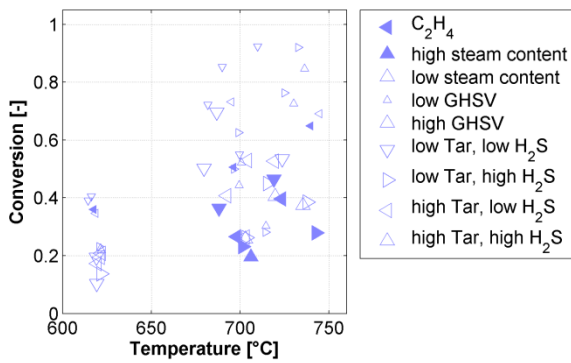
Figure 4.13: Ethene conversion
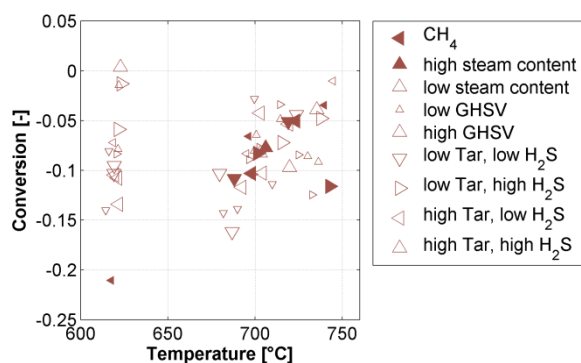
Figure 4.14: Methane conversion

Figure 4.14 shows methane conversion rates measured during experiments with tar and sulfur tars added to the syngas. Negative conversion rates can be observed which means that more methane was measured downstream of the reformer catalyst than upstream i.e. methane was a product formed by decomposition of hydrocarbons. No dependence of the methane formation on temperature, GHSV, water or sulfur content could be recognized. Most of the experiments showed an increase in methane concentration of 0 % to 15 %.

Deactivation of the catalyst was not observed during this study. Reference experiments were used to confirm the activation of the catalyst regarding methane conversion rates. After more than 150 h time on stream with exposure to tars and sulfur, the initial methane conversion rates could still be measured at same operating conditions. As shown in Figure 4.5, reversible adsorption inhibits active sites which reduced methane conversion. During operation without sulfur content for 1 h to 2 h, the initial methane conversion rate could be recovered. Longest experiments lasted up to 8 h. At the beginning of each experimental day, a reference point was measured to confirm the catalyst condition. Overnight, the set up was held at a temperature of 500 °C in air.

4.3 Applied kinetics

4.3.1 Reactor model and reactions

Parameters of pseudo first order, heterogeneous reaction kinetics were estimated with a one dimensional model based on mass conservation. The following assumptions were applied:

- steady state conditions (no time dependence)
- ideal gas behavior
- isothermal conditions (no energy balance to be solved)

- no pressure difference over the reactor
- uniform catalyst surface
- no carbon deposition
- homogenous gas phase reactions do not occur
- plug flow reactor (average bulk concentration and temperature)

Figure 4.15 illustrates the one dimensional reactor model based on mass balance over the length of the monolith. The reaction rate (r) equals the change in molar flow of a species ($d\dot{n}$) over the infinitesimal length of the catalyst (dL_m).

$$-r = \frac{d\dot{n}}{dL_m}$$

$L_m = 0$ cm $\qquad L_m \quad L_m + \Delta L_m \qquad 7.6$ cm
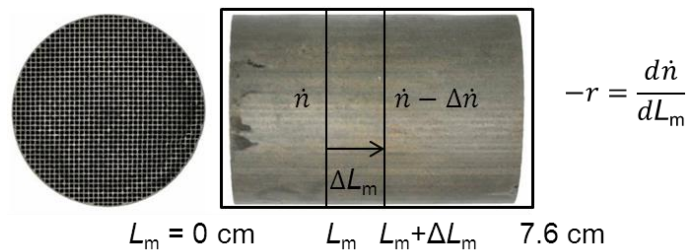
Figure 4.15: *One dimensional reactor model based on mass conservation integrated over the monolith length*

The following reactions were considered (Eq. 4.6 to Eq. 4.9):

$$SRM = CH_4 + H_2O \leftrightarrow CO + 3H_2 \qquad \text{Eq. 4.6}$$

$$WGS = CO + H_2O \leftrightarrow CO_2 + H_2 \qquad \text{Eq. 4.7}$$

$$C_xH_yS_z + x\,H_2O \rightarrow x\,CO + \left(x + \frac{y}{2} - z\right)H_2 + z\,H_2S \qquad \text{Eq. 4.8}$$

$$C_7H_8 + H_2 \rightarrow C_6H_6 + CH_4 \qquad \text{Eq. 4.9}$$
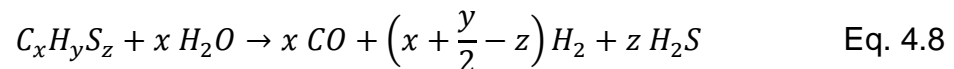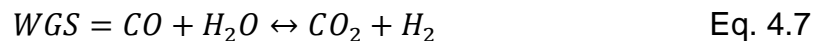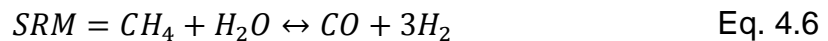
Based on experimental findings in chapter 4.2, the formation of ethane was fixed at 6 % of the reaction rate of ethene decomposition (Eq. 4.2). Contrary to other tar species, toluene was assumed to convert to benzene (Eq. 4.9). Decomposition of benzene was not considered because it could not be discerned with the available data basis.

4.3.2 Mass transfer limitations

To investigate the absence of external and internal mass transport limitations, the Carberry number and the Wheeler-Weisz moduli were calculated. Average concentrations over the length of the reactor and the temperature at the exit of the

reactor were used as inputs. The Carberry number (Ca) equals the relation of the observed reaction rate divided by volume of catalyst ($r_{v,obs}$) to the maximum mass transfer rate (Eq. 4.10). The product of the specific particle area (a'), the mass transfer coefficient (k_f) and the bulk concentration (c_b) equals the maximum mass transfer rate where the surface concentration (c_s) equals zero. In case of a monolith, the specific particle area equals the ratio of the catalytic active area (A_{cat}) and the volume of the monolith material (V_{cat}). The catalytic active area corresponded to the total channel surface (Table 4.1). The mass transfer coefficient depends on the Sherwood number (Sh), the diffusivity (D) and the hydraulic diameter (d_h) as shown in Eq. 4.13. The hydraulic diameter equals the monolith channel width. The Sherwood number was calculated according to Hawthorn [163]. Hawthorn developed a semi-analytical equation for the Sherwood number in square monolith channels (Eq. 4.19) correlated to the Reynolds (Re) (Eq. 4.18) and the Schmidt (Sc) number (Eq. 4.20) where (L_m) equals the monolith length, (u) defines the fluid velocity and (v_f) the kinematic viscosity. The Damköhler number type II (Da_{II}), requiring the knowledge of the intrinsic reaction rate, can be related to the Carberry number as shown in Eq. 4.12.

$$Ca = \frac{r_{v,obs}}{a' k_f c_b} = \frac{c_b - c_s}{c_b} \qquad \text{Eq. 4.10}$$

$$a' = \frac{A_{cat}}{V_{cat}} \qquad \text{Eq. 4.11}$$

$$\eta_e = (1 - Ca)^n = \frac{Ca}{Da_{II}} \qquad \text{Eq. 4.12}$$

$$k_f = \frac{Sh * D}{d_h} \qquad \text{Eq. 4.13}$$

$$Sh = 2.98 * \left(1 + 0.095 * Re * Sc * \frac{d_h}{L_m}\right)^{0.45} \qquad \text{Eq. 4.14}$$

$$Re = \frac{u * d_h}{v_f} \qquad \text{Eq. 4.15}$$

$$Sc = \frac{v_f}{D} \qquad \text{Eq. 4.16}$$

It is assumed that external mass transfer limitations can be excluded if effectiveness factors (η_e) are higher than 95 % (Eq. 4.12). Table 4.8 lists the minimum values observed for external effectiveness factors of tars and sulfur tars assuming first order reaction rates. External mass transfer limitations were not considered for tars and sulfur tars because effectiveness factors were above or close to 95 %. Assuming first order reaction rates, the Carberry number depends merely on the reaction rate constant because concentrations in nominator and denominator offset each other. Higher reaction rate constants lead to higher Carberry numbers and therefore to lower effectiveness factors.

	Effectiveness factor η_e	Wheeler - Weisz moduli Φ
	minimum value	maximum value
	[%]	[%]
C_4H_4S	94.7	10.2
C_8H_6S	93.2	12.8
$C_{12}H_8S$	92.4	14.0
C_7H_8	97.8	4.2
$C_{10}H_8$	98.5	2.8
$C_{14}H_{10}$	96.8	5.9
$C_{16}H_{10}$	99.1	5.4

Table 4.8: *Minimum values of catalyst external effectiveness factors and maximum values of Wheeler-Weisz moduli of conducted experiments used to determine external and internal mass transfer limitations*

Wheeler-Weisz moduli (Φ) were calculated to estimate intra-particle mass transfer limitations according to Eq. 4.17. As a simple expression, the Wheeler-Weisz modulus is the ratio of the observed reaction rate to the diffusion rate. More precise, the product of the observed reaction rate divided by the volume of catalyst ($r_{v,obs}$) and the thickness of the washcoat (L_{wc}) in the power of two divided by the effective Diffusion (D_{eff}) and the bulk concentration (c_b). The Wheeler-Weisz modulus can also be expressed as the product of the internal effectiveness factor (η_i) and the Thiele modulus (ϕ) as shown in Eq. 4.17. The internal effectiveness factor equals the ratio of the observed reaction rate to the reaction rate without internal diffusion limitations. The Thiele modulus equals the square root of the ratio of the reaction rate and the diffusion rate in the particle. The diffusion (D) consists of molecular diffusion (D_m) and Knudsen diffusion (D_k) as shown in Eq. 4.19. Calculations of the molecular and Knudsen diffusion can be found in annex A.5. The effective diffusion (D_{eff}) depends on the void fraction (ε) and the tortuosity factor (τ) of the washcoat (Eq. 4.18). Wheeler-Weisz moduli below 15 % indicate the absence of intra-particle diffusion limitations.

Void fraction, tortuosity factor, washcoat thickness and average pore size had to be estimated because no information was available about the commercial reformer catalyst. The average pore size was needed to calculate the Knudsen diffusivity and was set at 10 nm [164]. The high temperature stability of the catalyst indicates that the Al_2O_3 in the catalyst support is of alpha phase. Therefore, the assumption of 10 nm average pore size is rather a conservative assumption.

Values for ε and τ range between 0.3 to 0.6 and 2 to 5 respectively [165]. Washcoat thicknesses were reported from 10 µm to 150 µm [166]. The void fraction was set at 0.4, the tortuosity factor at 4 and the washcoat thickness at 40 µm. The maximum values of Wheeler-Weisz moduli are shown in Table 4.8. No intra-particle mass transfer limitations could be observed for tars and sulfur tars.

$$\Phi = \eta_i \phi^2 = \frac{r_{v,obs} L_{wc}^2}{D_{eff} c_b}$$

Eq. 4.17

$$D_{eff} = D \frac{\epsilon}{\tau}$$

Eq. 4.18

$$\frac{1}{D} = \frac{1}{D_m} + \frac{1}{D_k}$$

Eq. 4.19

Because only washcoated catalyst carriers are of interest, the catalyst layer thickness will not change considerably in case the catalyst is applied on other structures than the investigated monolith (e.g. monoliths with different cpsi, foams, filters). Therefore the Wheeler-Weisz modulus will be of minor importance compared to the Dahmköhler number type II.

4.3.3 Reaction rates

Reaction rates were described with a general model based on a Langmuir-Hinshelwood-Hougen-Watson (LHHW) approach. The reaction rate of the general model depends on the kinetic factor, driving force and an adsorption term (Eq. 4.20). The kinetic factor was reduced to the rate constant (*k*) of an assumed rate determining step (RDS) which was not further specified. The driving force is independent of the catalyst and represents the chemical affinity of the reaction to reach equilibrium. The adsorption terms build the denominator, causing a reduction of the reaction rate.

$$reaction\ rate = \frac{kinetic\ factor * driving\ force}{(adsorption\ term)^n} \qquad \text{Eq. 4.20}$$

Applying general kinetic models, reaction rate equation Eq. 4.21 was considered for parameter estimation. The nominator of Eq. 4.21 was multiplied by an equilibrium term if reaction rates could be positive or negative according to equilibrium calculations, i.e. SRM and WGS reactions (Eq. 4.6, Eq. 4.7). The denominator (DEN) in Eq. 4.22 equaled the adsorption on active sites. Adsorption of H_2O or sulfur or both was tested. The denominator was tested to be either in the power (n) of 1 or 2.

$$r_i = \frac{k_i * p_i * p_{H_2O}}{DEN} \qquad \text{Eq. 4.21}$$

$$DEN = (1 + K_i * p_i)^n \qquad \text{Eq. 4.22}$$

The rate constant (k_i) and the adsorption constant (K_i) have to be determined. The Arrhenius and van't Hoff equations show the temperature dependence of the rate constant and the adsorption constant (Eq. 4.23 and Eq. 4.24). Modified forms were used applying finite reference temperatures to avoid high correlations of pre-exponential factors and activation energies or heat of adsorptions. The reference temperature was set at 680 °C. The parameters to be estimated were pre-exponential factors (k_0, K_0), activation energy (E_a) and heat of adsorption (ΔH) for each compound (i). Parameters (θ) as shown in Eq. 4.25 to Eq. 4.28 had to be estimated. The exponential functions of the pre-exponential factors avoided chemically meaningless negative values.

$$k_i = e^{\left(\theta_{k,i} + \theta_{Ea,i} * \left(1 - \frac{T_{ref}}{T}\right)\right)} \qquad \text{Eq. 4.23}$$

$$K_i = e^{\left(\theta_{K,i} + \theta_{H,i} * \left(1 - \frac{T_{ref}}{T}\right)\right)} \qquad \text{Eq. 4.24}$$

$$\theta_{k,i} = \ln\left(k_{iT_{ref}}\right) \qquad \text{Eq. 4.25}$$

$$\theta_{K,i} = \ln\left(K_{iT_{ref}}\right) \qquad \text{Eq. 4.26}$$

$$\theta_{Ea,i} = \frac{E_{a,i}}{R * T_{ref}}$$

Eq. 4.27

$$\theta_{H,i} = \frac{\Delta H_i}{R * T_{ref}}$$

Eq. 4.28

4.4 Kinetic model results

4.4.1 Parameter estimation

The software used for kinetic parameter estimation and simulation was Athena Visual Studio version 14.2. Intel Visual Fortran compiler version 11.0 was used to compile the code for the GREGPLUS solver implemented in Athena Visual Studio. The GREGPLUS solver uses a Bayesian estimation approach enabling a simultaneous evaluation of multi response data [167, 168]. The resulting likelihood function describes the probability that the model predicted data actually describe the observed data. The central values of the highest probability density (HPD) calculated with a confidence of 95 % are reported in this study. The upper and lower limits of the 95 % HPD indicate the correctness of the estimation. The normalized parameter covariance matrix shows correlations between the estimated parameters. Ideally the correlation is low, i.e. close to zero. Parity plots and residual plots are provided to visualize the accuracy of predicted values and the absence of systematic deviations. If residual plots show non-random value distributions it is a sign of systematic errors in the model.

Reaction rate law of Eq. 4.21 including the equilibrium term could be applied to estimate the pre-exponential factor and the activation energy for SRM and WGS reactions. The denominator was found to consist only of sulfur adsorption in the power of two. Pre-exponential factor and heat of adsorption of sulfur could be estimated. The model selection was based first on the model ability to estimate the parameters and second on the smallest HPD intervals. Eq. 4.29 and Eq. 4.30 show the reaction rate laws for WGS and SRM as used to estimate pre-exponential factors, activation energy and heat of adsorption.

Parameters of WGS, SRM and sulfur adsorption were estimated together while parameters of tars and sulfur containing hydrocarbons were fixed. Molar flows of H_2, CO, CO_2, CH_4 and H_2O were chosen to be matched.

$$r_{CH_4} = \frac{k_{CH_4} * p_{CH_4} * p_{H_2O} * \left(1 - \dfrac{p_{CO} * p_{H_2}^3}{K_{eq\,SRM} * p_{CH_4} * p_{H_2O}}\right)}{(1 + K_S * p_S)^2}$$

<div align="right">Eq. 4.29</div>

$$r_{WGS} = \frac{k_{WGS} * p_{CO} * p_{H_2O} * \left(1 - \dfrac{p_{CO_2} * p_{H_2}}{K_{eq\,WGS} * p_{CO} * p_{H_2O}}\right)}{(1 + K_S * p_S)^2}$$

<div align="right">Eq. 4.30</div>

Table 4.9 lists the parameters estimated (θ), the according highest posterior density (HPD) intervals, the normalized parameter covariance matrix and the pre-exponential factors, the activation energies and the heat of adsorption. Activation energies estimated for WGS and SRM were (140 ± 37) kJ mol^{-1} and (151 ± 20) kJ mol^{-1}. The heat of adsorption of sulfur was estimated to be (-178 ± 52) kJ mol^{-1}.

	Parameter estimated			95 % HPD interval	Normalized parameter covariance matrix						k_0 [mol s^{-1} kg^{-1} bar^{-1}] E_a [kJ mol^{-1}]	
Water gas shift	$\ln(k_0)$	0.97 ±	0.3	34%	1.00						k_0	2.65
	E_a/RT_{ref}	17.76 ±	4.6	26%	0.69	1.00					E_a	141
Methane	$\ln(k_0)$	-1.14 ±	0.2	15%	0.01	-0.03	1.00				k_0	0.32
	E_a/RT_{ref}	19.10 ±	2.5	13%	0.06	0.13	-0.79	1.00			E_a	151
Sulfur adsorption	$\ln(K_0)$	13.42 ±	0.5	4%	0.61	0.52	0.01	0.02	1.00		k_0	676
	$\Delta H/RT_{ref}$	-22.47 ±	6.6	29%	-0.07	0.01	-0.01	0.07	-0.74	1.00	ΔH	-178

Table 4.9: *Estimated parameters for steam reforming of methane and water gas shift reactions including 95 % HPD intervals and normalized parameter covariance matrix*

Parameters of ethene, tars and sulfur containing hydrocarbons were estimated according to the reaction rate law as shown in Eq. 4.31 and fitted to the decomposition of species (i). The reaction rate (r_i) equals the rate constant (k_i) times the partial pressure of compound (i). Eq. 4.31 is a simple power law and a reduced form of Eq. 4.21 without partial pressure of steam and denominator. The power law is valid for extrapolations within similar operating conditions.

$$r_i = k_i * p_i$$

<div align="right">Eq. 4.31</div>

One reason for the independence of tar and sulfur tar conversions on sulfur content as compared to WGS and SRM could be the existence of different active centers used for tar and sulfur tar conversions. More likely, the applied H$_2$S concentrations of 20 ppmV and 100 ppmV were too high to recognize an influence on conversion rates.

The results of the parameter estimation for ethene, tars and sulfur tars are shown in Table 4.10. For ethene, an activation energy of (50 ± 21) kJ mol^{-1} was estimated. Activation energies of tars were in the range of 24 kJ mol^{-1} to 126 kJ mol^{-1}. Estimations of activation energies for sulfur tars were considerably lower from 7.3 kJ mol^{-1} to 11.5 kJ mol^{-1}.

Wide HPD intervals of activation energies were found for tar and sulfur tar species. One reason for the high HPD intervals could be variations in the operating temperature dependence of some experimental results. Very low conversions as found for naphthalene and pyrene or very high conversions as found for sulfur tars showed a limited influence of the operating temperature and increasing influence of measurement deviations. A weak dependence of the operating temperature on the conversion rates resulted in low activation energies. Measurement deviations caused by the sampling system and the analytical equipment could lead to some experiments showing apparent lower conversions at higher temperatures. Parameter estimation based on data including some variations will show higher HPD intervals than otherwise.

	Parameter estimated			95 % HPD interval	Normalized covariance		k_0 [mol s-1 kg-1 bar-1] E_a [kJ mol-1]	
Ethene	$\ln(k_0)$	-2.49	± 0.1	6%	1.00		k_0	0.08
	E_a/RT_{ref}	6.32	± 2.6	41%	0.65	1.00	E_a	50.1
Toluene	$\ln(k_0)$	-3.83	± 0.3	9%	1.00		k_0	0.02
	E_a/RT_{ref}	14.11	± 6.7	47%	-0.86	1.00	E_a	111.8
Naphthalene	$\ln(k_0)$	-5.13	± 0.4	8%	1.00		k_0	0.01
	E_a/RT_{ref}	4.06	± 6.8	167%	-0.33	1.00	E_a	32.2
Phenanthrene	$\ln(k_0)$	-4.40	± 0.4	10%	1.00		k_0	0.01
	E_a/RT_{ref}	15.86	± 8.2	52%	-0.88	1.00	E_a	125.7
Pyrene	$\ln(k_0)$	-4.23	± 0.3	7%	1.00		k_0	0.01
	E_a/RT_{ref}	3.03	± 3.4	114%	-0.16	1.00	E_a	24.0
Thiophene	$\ln(k_0)$	-1.36	± 0.1	9%	1.00		k_0	0.27
	E_a/RT_{ref}	1.06	± 1.2	111%	-0.47	1.00	E_a	8.7
Benzothiophene	$\ln(k_0)$	-1.24	± 0.1	5%	1.00		k_0	0.29
	E_a/RT_{ref}	0.92	± 0.8	83%	0.17	1.00	E_a	7.3
Dibenzothiophene	$\ln(k_0)$	-2.01	± 0.2	7%	1.00		k_0	0.13
	E_a/RT_{ref}	1.45	± 2.6	176%	0.05	1.00	E_a	11.5

Table 4.10: *Estimated parameters for ethene, tars and sulfur tars including 95 % HPD intervals and normalized parameter covariance matrices*

4.4.2 Parity and residual plots

Figure 4.16 to Figure 4.30 show parity plots of observed and predicted molar flows measured at the exit of the reformer catalyst and according residuals. Observed

and predicted conversions instead of molar flows are shown for sulfur tars because conversion rates were high and corresponding molar flows after the reformer were very small. Therefore conversion values are easier to read the quality of the model predictions.

All predicted molar flows of H_2 deviate less than 25 % from the observed values (Figure 4.16). Two groups of data points can be recognized at lower and higher molar flow corresponding to low and high GHSV. The two groups can be recognized in the parity and residual plots.

Figure 4.16: *Hydrogen: predicted vs. observed molar flow at the exit of the reformer catalyst and residuals vs. observed values*

Figure 4.17: *Methane: predicted vs. observed molar flow at the exit of the reformer catalyst and residuals vs. observed values*

79 % of predicted methane molar flows deviate less than 25 % from observed values (Figure 4.17). The results were less accurate for small flows after the reformer (high conversions) than higher molar flows (small conversions). Lower concentrations cause higher measurement deviations. Methane conversion rates depended strongly on sulfur content as expressed by the adsorption term of the SRM reac-

tion rate (Eq. 4.6). Small methane conversions are expected after the reformer in case of sulfur containing producer gas.

Simulated molar flows of CO predicted the observed molar flows quite well. 97 % of predicted values deviated less than 25 % from observed values (Figure 4.18). High CO molar flows after the reformer correspond with operating conditions at high GHSV and high sulfur content. Lowest molar flows of CO were measured for sulfur free operating conditions at low GHSV.

70 % of predicted CO_2 molar flows deviated less than 25 % from observed values (Figure 4.19). High molar flows after the reformer were better predicted than low molar flows. Observed molar flows below $0.75*10^{-3}$ mol s^{-1} could not be predicted correctly. The predicted values deviate by more than 25 % from the observed values. Low CO_2 molar flows were observed for operating conditions at low GHSV and high sulfur content or low temperature.

Figure 4.18: *Carbon monoxide: predicted vs. observed molar flow at the exit of the reformer catalyst and residuals vs. observed values*

Figure 4.19: *Carbon dioxide: predicted vs. observed molar flow at the exit of the reformer catalyst and residuals vs. observed values*

Predicted molar flows of H_2O were close to observed molar flows. Only two values deviate more than 25 % from observed values (Figure 4.20).

Figure 4.20: *Water: predicted vs. observed molar flow at the exit of the reformer catalyst and residuals vs. observed values*

The simulation did not predict ethene molar flows after the reformer very well. 54 % of predicted values deviated more than 25 % from observed values (Figure 4.21). High and low molar flows could not be predicted correctly. Testing to include sulfur adsorption in the reaction rate equation made the predicted values deviating even more from observed values. Too high molar flows were predicted on average and accordingly the catalyst activity was underestimated.
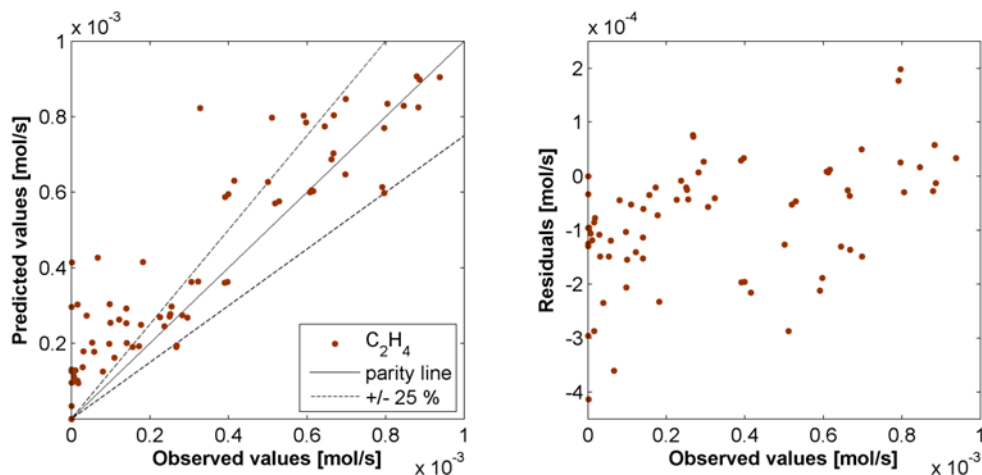
Figure 4.21: *Ethene: predicted vs. observed molar flow at the exit of the reformer catalyst and residuals vs. observed values*

The predicted ethane molar flows were fixed to the predicted molar flows of ethene. Ethane was built at a fixed rate of 6 % of the ethene decomposition rate. Since the predicted values for the ethene molar flow showed high deviations from the observed values, it was not possible to better model the ethane molar flow (Figure 4.22).
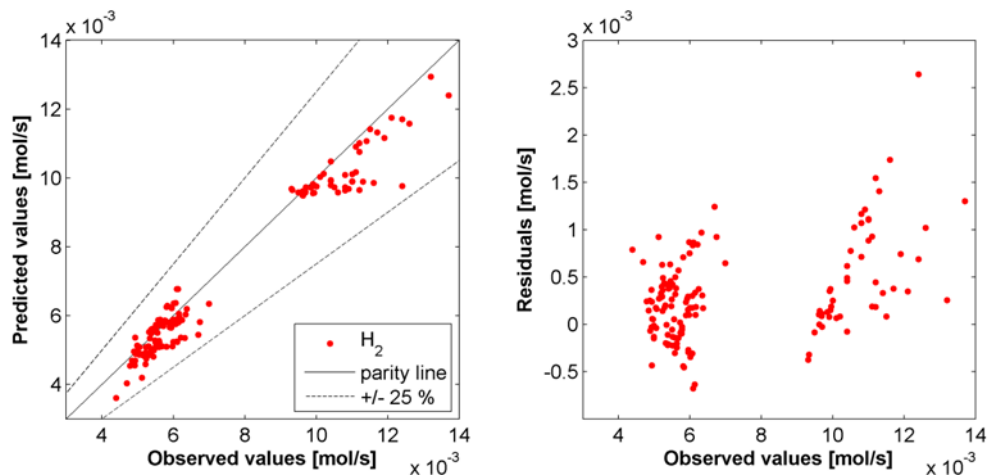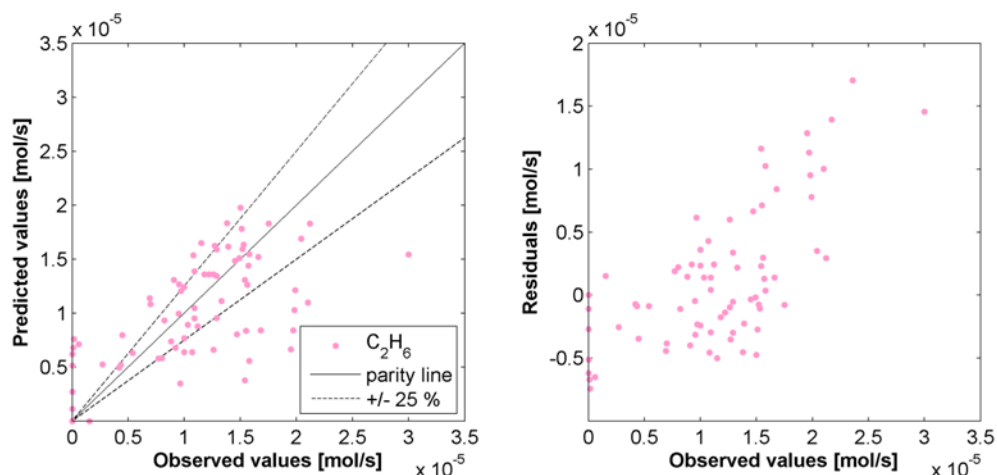
Figure 4.22: *Ethane: predicted vs. observed molar flow at the exit of the reformer catalyst and residuals vs. observed values*

The parameters of tars and sulfur tars were estimated for each individual compound fitted to the decomposition of the single compound. Reaction rates of toluene, naphthalene, phenanthrene and pyrene could be simulated quite well. 79 % of predicted toluene, 94 % of predicted naphthalene, 81 % of predicted phenanthrene and 58 % of predicted pyrene values did not deviate by more than 10 % from observed molar flows (Figure 4.23 to Figure 4.26). Molar flows of pyrene were the most difficult to correctly predict. Very low concentrations of pyrene caused deviations of the measured data which is reflected in the parity plot (Figure 4.26).
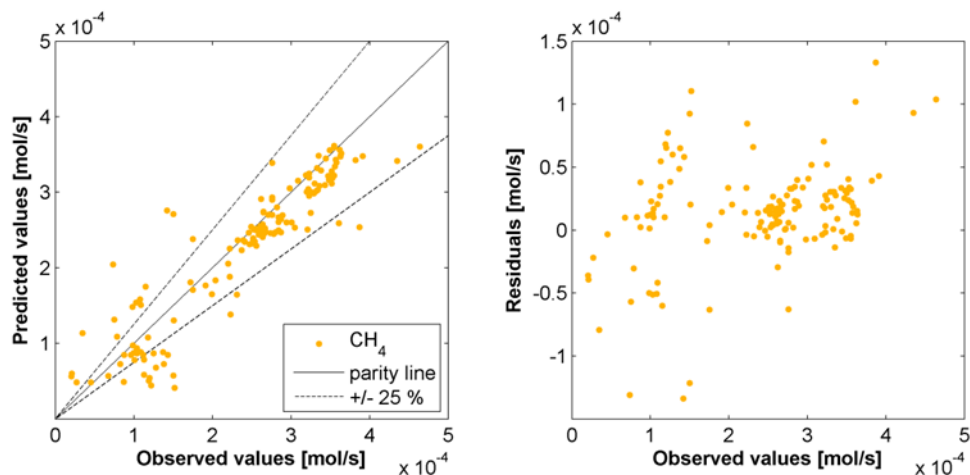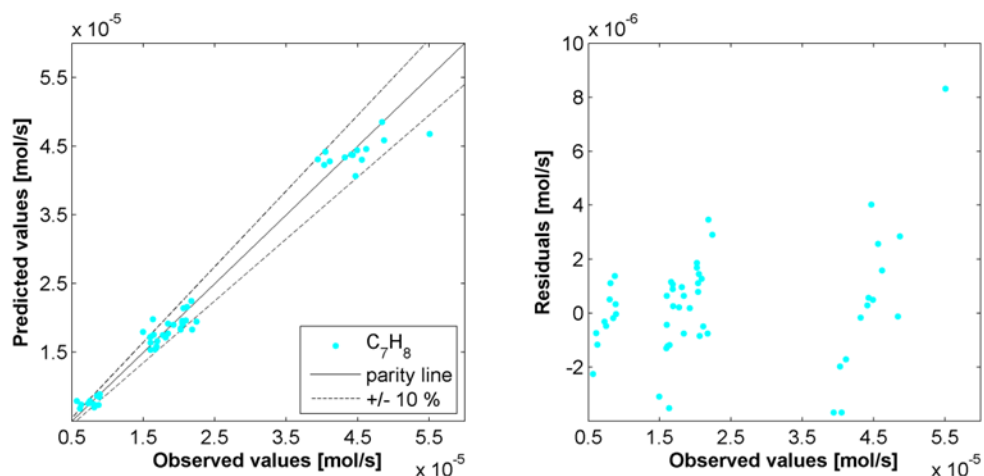

Figure 4.23: *Toluene: predicted vs. observed molar flow at the exit of the reformer catalyst and residuals vs. observed values*

In particular the high molar flows after the reformer (low conversion) could not be simulated very well and the predicted values were too low (overestimating the activity of the catalyst). Three groups of data can be recognized in the parity plots of the four mentioned tars. Lowest molar flows of tars could be observed for operating conditions at low GHSV and low tar load. Highest molar flows of tars could be observed for operating conditions at high GHSV and high tar load. Medium molar

flows of tars consisted of operating conditions at low GHSV combined with high tar load and high GHSV combined with low tar flow. These three groups can also be observed in the residuals plots.
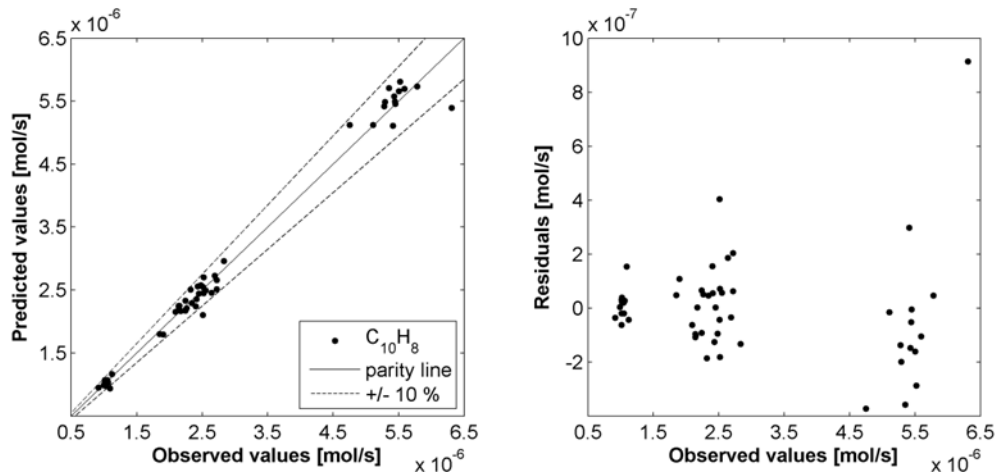
Figure 4.24: *Naphthalene: predicted vs. observed molar flow at the exit of the reformer catalyst and residuals vs. observed values*
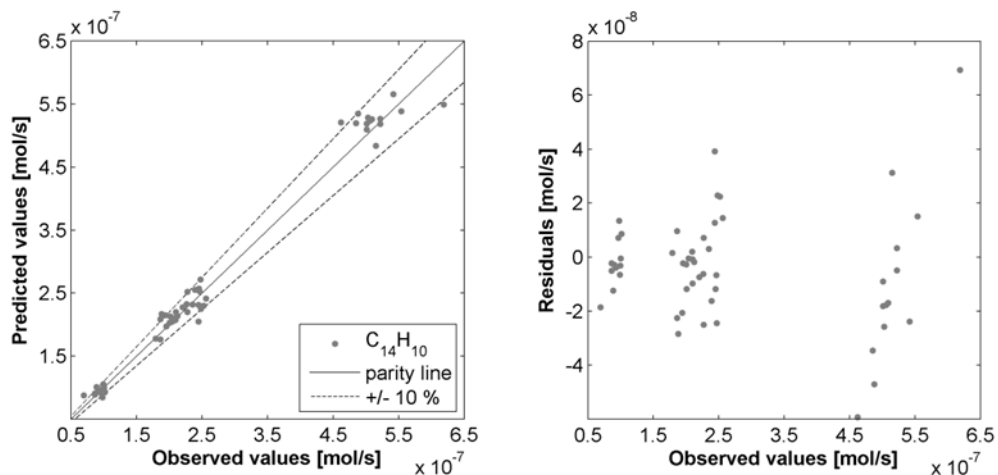
Figure 4.25: *Phenanthrene: predicted vs. observed molar flow at the exit of the reformer catalyst and residuals vs. observed values*
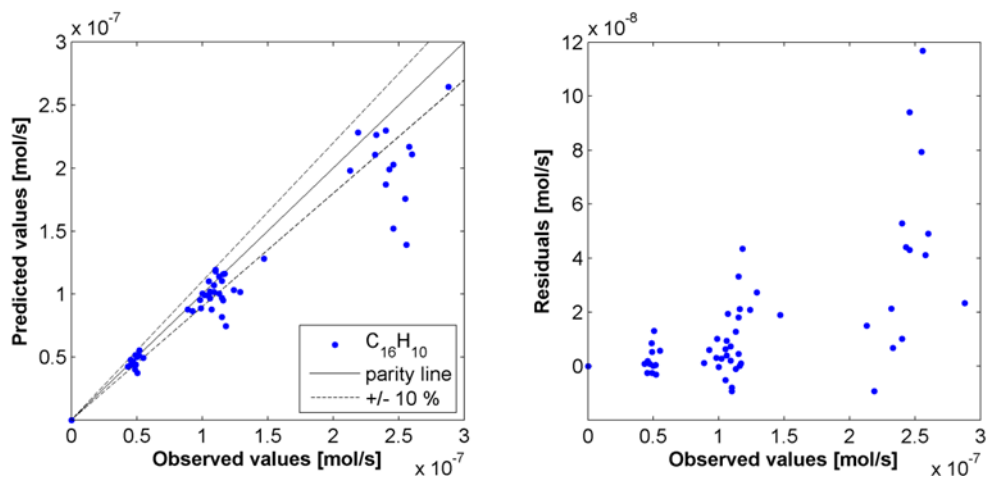
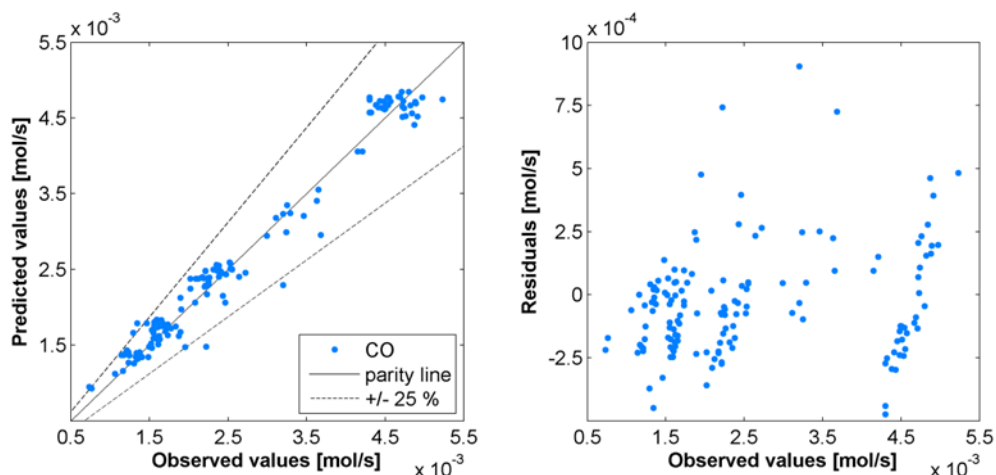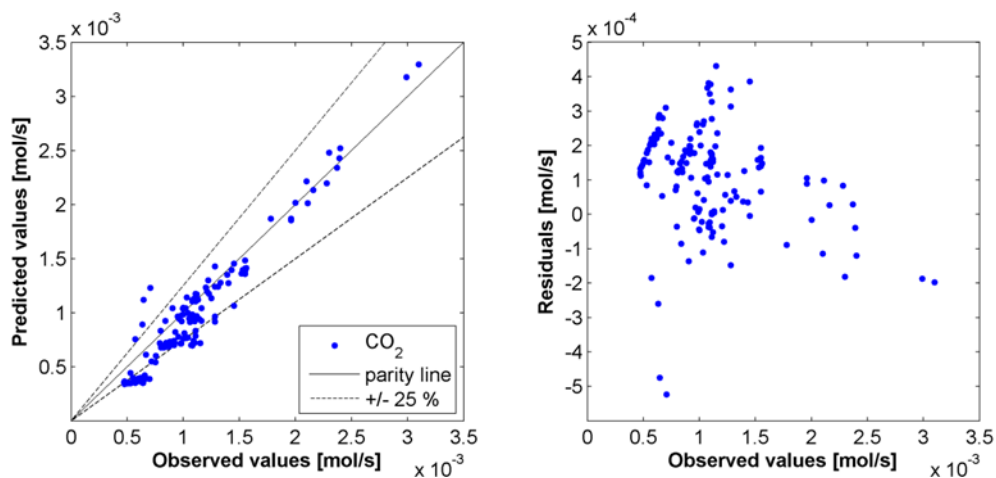***Figure 4.26:*** *Pyrene: predicted vs. observed molar flow at the exit of the reformer catalyst and residuals vs. observed values*
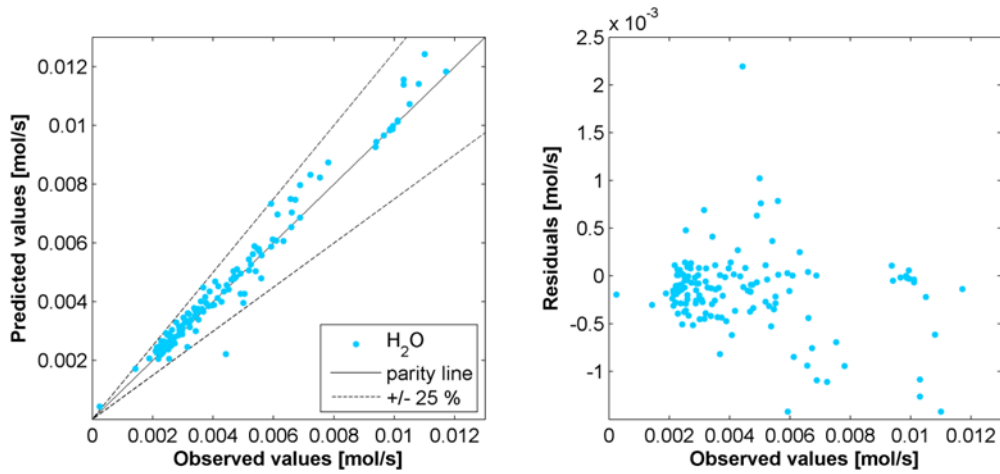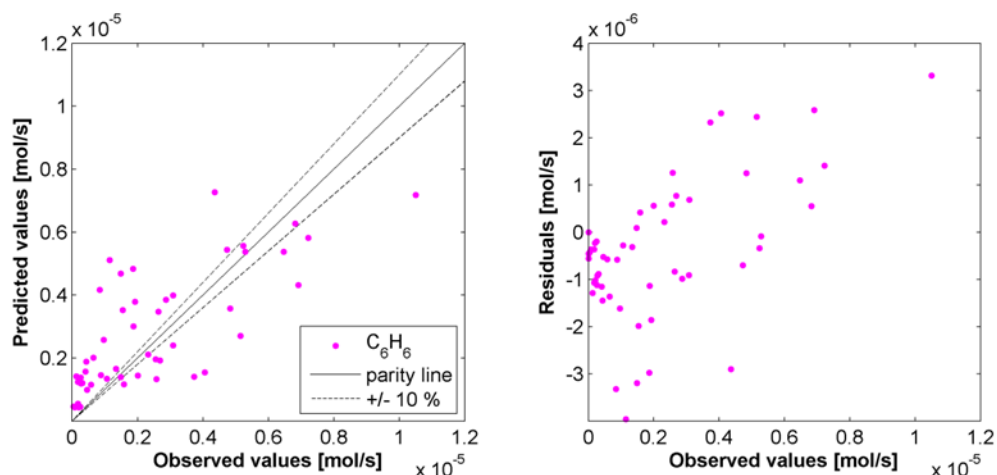
Figure 4.27: *Benzene: predicted vs. observed molar flow at the exit of the reformer catalyst and residuals vs. observed values*

The reaction rate of benzene could not be modeled independently. The rate was fixed to the reaction rate of toluene assuming the creation of one benzene molecule by dealkylation of toluene. The correlation of toluene decomposition with benzene creation seemed to be reasonable though predicted values deviate considerably from observed values (Figure 4.27).
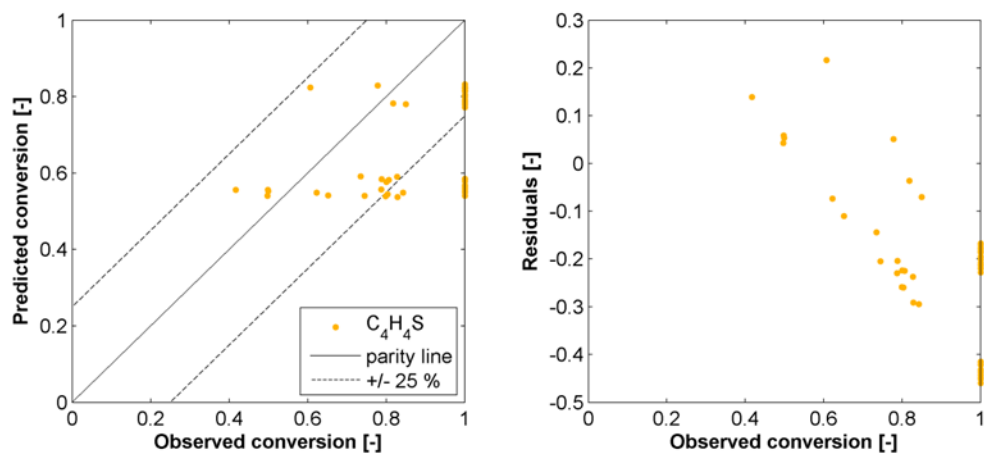
Figure 4.28: *Thiophene: predicted vs. observed conversions over the reformer catalyst and residuals vs. observed conversion*

In the parity plots of the sulfur tars (Figure 4.28 to Figure 4.30), two horizontal lines of data points could be observed, corresponding to operating conditions at high/low GHSV. The same lines could be observed in the residual plots as well. The model suggested conversions between 30 % to 60 % (observed 15 % to 99.9 %) for sulfur tars at high GHSV and conversions of 50 % to 85 % (observed 40 % to 99.9 %) at low GHSV. The range of observed conversions was wider than the range of predicted conversions. Therefore the model underestimated the activity of the catalyst at high conversions and overestimated the activity at low conversions. High conversion rates of sulfur containing hydrocarbons made parameter estimation more difficult. Many experiments had to be excluded from the modeling

data base because conversions where that high that the LOD was reached (experiments with an observed conversion of 1 reached the LOD). Due to excluding the experiments with apparent full conversion, the model was not able to predict observed apparent full conversion correctly, i.e. the model underestimates the catalytic activity.

72 % of predicted conversions of thiophene deviated less than 25 % from the observed conversion (Figure 4.28). The apparent full conversion of operating conditions at low GHSV were predicted to be 75 % to 85 % which was inside the ± 25 % range. Looking at predicted values where observed conversion was below 0.9, most of the predicted values were inside the ± 25 % range.
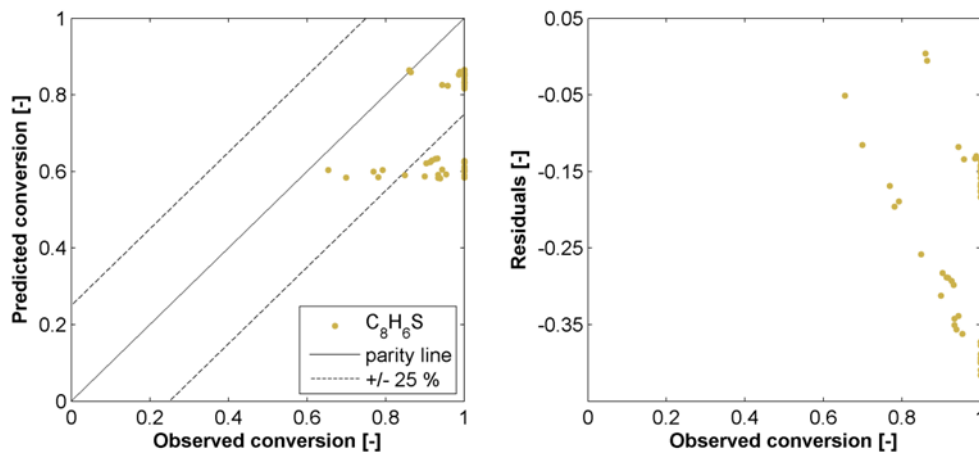
Figure 4.29: *Benzothiophene: predicted vs. observed conversions over the reformer catalyst and residuals vs. observed conversion*
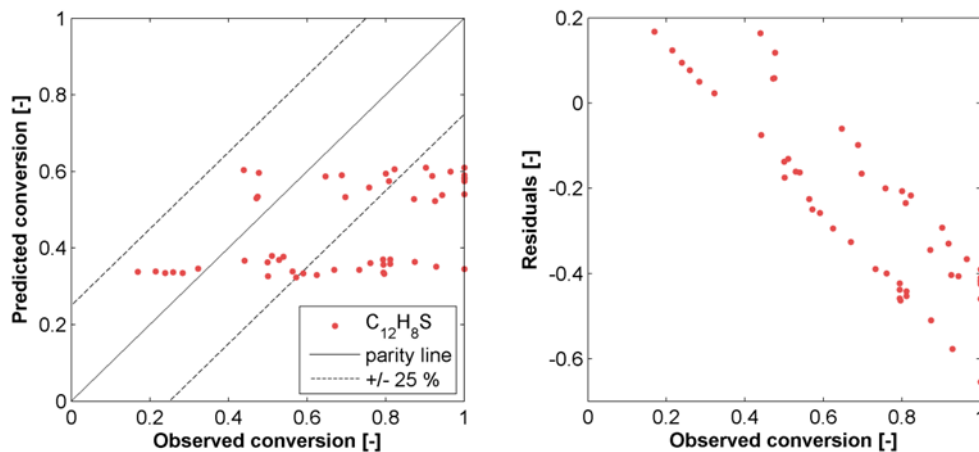
Figure 4.30: *Dibenzothiophene: predicted vs. observed conversions over the reformer catalyst and residuals vs. observed conversion*

57 % of predicted conversions of benzothiophene deviated less than 25 % from the observed conversion (Figure 4.29). The apparent full conversion of low GHSV was predicted to be 81 % to 87 % and deviates by less than 25 % from observed

values. The apparent full conversion of high GHSV was predicted by the model to be 58 % to 64 % reflecting the application of conservatively estimated parameters.

47 % of predicted conversion of dibenzothiophene deviated less than 25 % from the observed conversion (Figure 4.30). The apparent full conversion of the low GHSV was predicted to be 52 % to 61 % and 45 % deviated by less than 25 % from observed. The apparent full conversion of high GHSV was predicted by the model to be 32 % to 38 %.

4.5   Simulation of monolithic reformer reactors

With the parameters estimated in chapter 4.4, conversions over the catalyst length can be calculated at different temperatures (Figure 4.31 and Figure 4.32). A permanent gas matrix closer to a real wood gasifier (e.g. allothermal dual fluidized bed gasifier) was chosen for this simulation, as shown in Table 4.11. H_2S concentration was set at 20 ppmV corresponding to the application of sulfur sorption material upstream of the HGF. Tar load was set according to the lower tar load case (Table 4.4), assuming a gasifier producing small amounts of tars or applying catalyst material in the gasifier. Assuming steam as gasification agent, steam content was set at 30 vol%. Ethene content was set to 1 vol%. The catalyst parameters were kept the same but the length was increased from 7.6 cm to 28 cm. The gas flow of 1.39 m_n^3 h^{-1} (GHSV of 9'000 h^{-1}) was kept the same corresponding to a velocity of 19 cm s^{-1}.

	H_2	CH_4	CO	CO_2	N_2	H_2O	C_2H_4
vol%	27.6	6.9	13.8	17.2	3.4	30.0	1.0

Table 4.11: *Gas composition as used for simulation without tars and sulfur species*

Figure 4.31 shows the simulation results calculated at a temperature of 600 °C. At catalyst length 12.6 cm, the concentration of sulfur tars was below 1 ppmV. 16.5 cm of catalyst were needed to reduce the sulfur tar concentration below 0.5 ppmV and 26.7 cm of catalyst were needed to reduce the sulfur tar concentration below 0.1 ppmV. Ethene concentration was reduced below 0.4 % at the end of 28 cm of catalyst, therefore H_2 and CO concentration increased. CH_4 concentration stayed the same. Toluene concentration decreased by 100 ppmV and benzene concentration increased by the same amount.
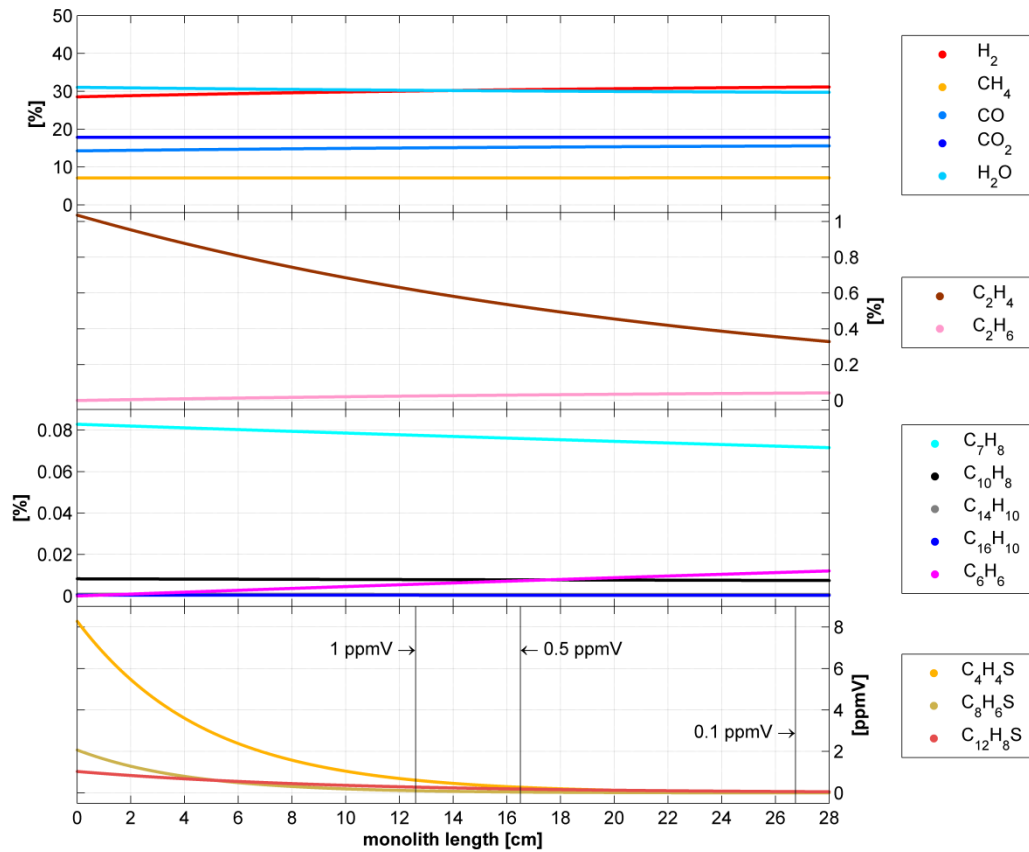
Figure 4.31: *Model results of the change of gas composition over the length of the catalytic monolith at low tar load, low GHSV, 20 ppmV of H_2S and at temperature of 600 °C*
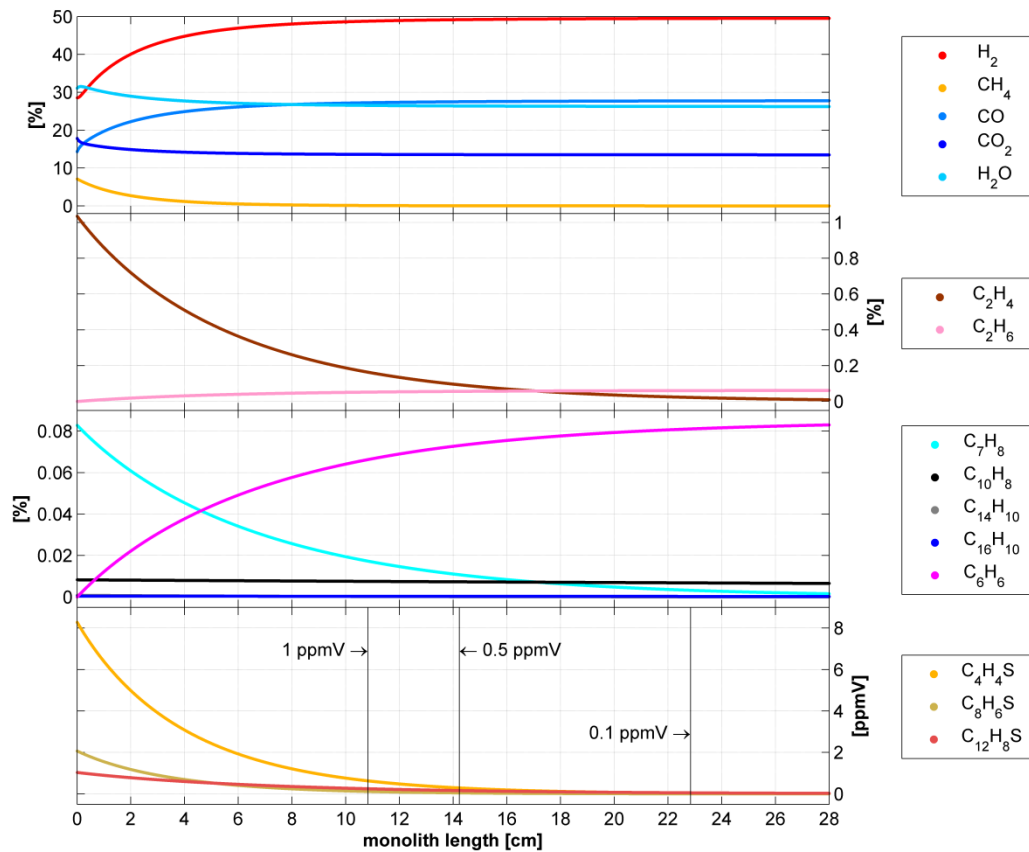
Figure 4.32: *Model results of the change of gas composition over the length of the catalytic monolith at low tar load, low GHSV, 20 ppmV of H_2S and at temperature of 850 °C*

113

Simulation results of an operating temperature of 850 °C are shown in Figure 4.32. 850 °C is expected to be the maximum temperature that could be reached in a HGF heated solely by the heat of producer gas coming from a biomass gasifier. At 10.8 cm the concentration of sulfur tars was below 1 ppmV, at 14.2 cm below 0.5 ppmV and at 22.8 cm below 0.1 ppmV. Toluene, ethene and methane conversion reached 100 % at catalyst length of 28 cm. H_2 concentration increased by more than 20 % mainly due to methane and ethene conversions and WGS. Results with high tar load instead of low tar load can be found in the annex (Figure A.1 and Figure A.2).

The temperature of the producer gas can be increased to the desired temperature by catalytic partial oxidation (CPO) at the cost of heating value. Assuming a producer gas temperature of 600 °C at the exit of the gasifier and a required temperature of 850 °C to reach lower tar concentrations, the producer gas temperature can be increased by adding air in front of the catalyst conducting CPO. Assuming only the CPO of H_2, as shown in Eq. 4.32, 286 kJ mol^{-1} of energy was gained to increase the temperature of the producer gas. An absolute volume fraction of 3.5 % of H_2 needed to be oxidized, calculating with a heat capacity of 40 J mol^{-1} K^{-1} of the producer gas at 600 °C. Accordingly an absolute volume fraction of 1.75 % of oxygen had to be added to the producer gas. The total gas volume increases by adding air (7.95 vol%). The oxidized H_2 equals a reduction in heating value by 5 % (0.15 kW, LHV H_2 = 11.1 MJ m$_n^{-3}$). Since oxidation reactions take place very fast, it is assumed that no additional catalyst material would be needed for CPO.

$$H_2 + 0.5\ O_2 \rightarrow H_2O \qquad -\Delta H_R^0 = 286\ \text{kJ mol}^{-1} \qquad\qquad \text{Eq. 4.32}$$
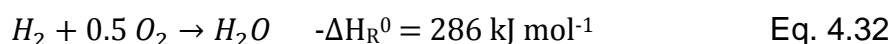
4.6 Reactive hot gas filter

The simulation results of monolithic reformer reactors as presented in chapter 4.5 were used to consider different integration options of the reformer catalyst into HGF designs as presented in Figure 2.9. For the purpose of this study, we assumed a wood gasifier with a thermal input of 1 MW. A gasifier operated under pressure was favored to reduce gas volume. An allothermal gasifier operated at a pressure of 0.5 MPa and an exit temperature of 850 °C was decided to be realistic. Gasifier specifications can be found in Table 4.12.

Horizontal and vertical filter designs were considered for the integration of the reforming catalyst into the reactive HGF. Aiming at a filtration velocity of 2.6 cm s^{-1}

(filtration velocity equals the operating gas volume divided by the filter surface area), two filter designs were developed according to the gas flow of 176.3 $m^3\ h^{-1}$ (Table 4.12). The same filter material was considered for both designs.

Thermal input	[MW]	1.0
Cold gas efficiency	[%]	75
Gasifier exit temperature	[°C]	850
Operating pressure	[MPa]	0.5
Heat value wood gas	[kWh m_n^{-3}]	3.5
Gas flow (V_n)	[$m_n^3\ h^{-1}$]	214
	[$m^3\ h^{-1}$]	176.3

Table 4.12: *Assumptions of 1 MW allothermal wood gasifier*

The horizontal filter design operates with more filter candles of smaller length than the vertical filter design which applies less filter candles of longer size. The filter surface area had to be the same for both designs in order to get the same filtration velocity. Filter specifications for vertical and horizontal filter designs can be found in Table 4.13. The vertical filter design applies 5 filter candles of 2.0 m length and the horizontal filter design applies 20 filter candles of 0.5 m length. With a total gas flow of 214 $m_n^3\ h^{-1}$, the corresponding gas flows per filter candle were 10.7 $m_n^3\ h^{-1}$ for the horizontal design and 42.8 $m_n^3\ h^{-1}$ for the vertical design.

		Horizontal design	Vertical design
Filter diameter (d_o/d_i)	[cm]	6/4	
Filter length	[m]	0.5	2.0
Filter elements	[-]	20	5
Total filter surface area	[m^2]	1.88	
Filter velocity	[cm s^{-1}]	2.6	
Volume of filter material	[m^3]	0.016	

Table 4.13: *Assumptions for hot gas filter of horizontal and vertical design*

With the simulation results presented in chapter 4.5, integration considerations can be conducted. Assuming the identical catalytic layer could be applied to other substrates, the area of the catalytic layer needed for a certain conversion can be calculated according to the length of the monolith. A catalytic active layer area of 1.26 m^2 (L_m = 22.8 cm) has to be provided at 850 °C in order to reach sulfur tar concentrations below 0.1 ppmV at a gas flow of 1.39 $m_n^3\ h^{-1}$ (Figure 4.32). This corresponds to a catalytic active layer area of 0.91 $m^2\ m_n^{-3}$ h. Accordingly, gas flows of 10.7 $m_n^3\ h^{-1}$ and 42.8 $m_n^3\ h^{-1}$ per filter element require a catalytic active layer area of 9.7 m^2 and 38.8 m^2 in order to reach sulfur tar concentrations below 0.1 ppmV at 850 °C.

Considering the integration of a monolith or foam inside a filter element, the diameter is limited by the inner diameter of the filter candle (4 cm). Accordingly a 400 cpsi monolith of 284 cm (342 cm² per cm of monolith length, diameter of 4 cm, channel width of 1.1 mm, number of channels: 779) or a 1200 cpsi monolith of 184 cm (527 cm² per cm of monolith length, diameter of 4 cm, channel width of 0.56 mm, number of channels: 2337) would be needed at the end of a horizontally installed filter candle in order to reach sulfur tar concentrations below 0.1 ppmV by providing a catalytic active layer area of 9.7 m². Any monolith length that is longer than the filter candle itself would increase filter vessel volume and therefore costs massively and is therefore not reasonable to consider.

Considering ceramic foam as catalyst carrier instead with corresponding pores per inch (PPI) cannot reduce the length considerably since inner surface areas of foams and monoliths are comparable [169]. Foams offer advantages if external mass transfer limitations are an issue. Foams with a higher PPI values would increase the pressure drop during filter operation which has to be avoided.

Catalytic active filter candles need to offer catalytic active layer areas of 12'400 m² m⁻³ (total filter material volume of 15'700 cm³). Foam cylinders of 4 cm outer and 2 cm inner diameter placed at the inside of the filter candles need catalytic active layer areas of 20'600 m² m⁻³ (total cylinder material volume of 9'400 cm³). These catalytic active layer areas per m³ of porous material are reasonable compared with values of foams provided by Twigg [170] (80 PPI = 15'800 m² m⁻³).

At the exit of the HGF a 400 cpsi monolith of 0.071 m³ (40 cm x 57 cm) or a 100 cpsi monolith of 0.133 m³ (40 cm x 106 cm) would be needed to provide a total catalytic active layer area of 194.4 m². According to Eq. 4.33, the 400 cpsi monolith generates a pressure drop (ΔP) of 26 hPa while the 100 cpsi monolith causes a pressure drop of 9 hPa.

$$\Delta P = \frac{56.92}{Re} * \frac{\rho}{2} * \left(\frac{Q_{ch}}{A_{ch}}\right)^2 * \frac{L_{ch}}{d_h} \qquad \text{Eq. 4.33}$$

4.7   Discussion

The decision to use a gas mixture containing four different tars and three different sulfur containing hydrocarbons caused some challenges. To obtain realistic data, concentrations were chosen according to conditions as found in producer gas of wood gasifiers. Therefore concentrations of sulfur containing hydrocarbons were low with concentrations upstream of the reformer catalyst from 20 ppmV down to 2 ppmV. Even lower concentrations downstream of the reformer catalyst were demanding to measure correctly. High G/L ratios of the liquid sampling system enabled the detection down to sub-ppmV gas phase concentrations. Thiophene showing the highest LOD can be detected in the gase phase down to 65 ppbV to 75 ppbV depending on operating conditions of the reformer set up and the sampling system. If even lower concentrations have to be detected, sampling system and analytics have to be optimized.

Apparent full conversion, where no molecules of a certain species could be detected downstream of the reformer, was limited by the LOD of the analytical equipment. Decreasing the corresponding LOD in the gas phase could be done by higher gas to liquid ratios (increasing the concentration in the liquid phase). Reducing the LOD of the analytical equipment could perhaps be done by improving the method of the GC to specific components. Otherwise more sensitive equipment is needed.

The required sulfur tar conversion rate is given by process units downstream of the reformer catalyst. In case a fuel cell is used as energy converter (e.g. SOFC), the so called biomass integrated gasification fuel cell (B-IGFC) system, the sulfur content should be below 1 ppmV to assure a sustainable operation of the nickel containing fuel cell catalyst [171]. Assuming a sulfur tar concentration of 11 ppmV in the producer gas, e.g. wood gasification (Table 4.3), and a sulfur target concentration of 0.5 ppmV, the desired conversion rate has to be higher than 95 %. With the current sampling and analytical equipment it was possible to measure thiophene concentrations in the producer gas down to 64 ppbV which is low enough to confirm sulfur concentrations of 0.5 ppmV.

4.8 Conclusion

4.8.1 Experimental results

The noble metal catalyst tested in this study showed high activities for the decomposition of sulfur containing hydrocarbons. Because the catalyst was able to decompose sulfur tars under operating conditions close to a real wood gasification plant, it would be possible to use it for HGC in any process that includes sulfur sensitive catalysts such as B-IGFC, liquid fuel synthesis or methanation processes. H_2S produced by the reforming catalyst could be captured downstream of the reformer in a metal oxide bed.

Operating the tar reforming catalyst at 740 °C and at low GHSV (9000 h^{-1}) would decompose thiophene and benzothiophene. Less than 20 % of dibenzothiophene (< 1 ppmV) would remain in the syngas. It is expected that higher temperatures would decompose even more dibenzothiophene and more of the sulfur free tars. Assuming a real wood gasification plant where the catalyst could be operated at maximum temperature of 740 °C, in such a case lower GHSV, higher temperature or more catalyst would be needed to reach a full conversion of dibenzothiophene.

The conversion of sulfur free tars was significantly lower than the conversion of sulfur tars. Highest conversion of 47 % was measured for toluene. More catalyst would be needed if low tar concentrations are required.

In the presence of sulfur, methane was not decomposed which is an advantage if the producer gas is used for methanation or solid oxide fuel cell (SOFC) applications [81].

4.8.2 Applied kinetics

Applied kinetics for a commercially available noble metal catalyst could be established. First order kinetics could be developed for tars and sulfur tars as well as for ethene. The formation of ethane and benzene was assumed to be at constant rate depending on the decomposition of ethene and toluene respectively. Reaction rate laws of SRM and WGS could be determined including equilibrium term and adsorption of sulfur.

In awareness of relatively high HPD intervals and deviations of predicted to observed values, simulations were conducted. The estimated parameters and model assumptions were on the conservative side, underestimating the catalyst activity. Simulations at operating temperatures of 850 °C showed higher conversions rates

for sulfur free tars, ethene and methane while the temperature dependence of sulfur tars was limited.

Different possibilities were evaluated regarding the integration of catalytic material into HGF units. The option of catalytic active filter elements, additional catalytic foam at the inside of the filter element and a monolith at the exit of the filter vessel were feasible assuming the same catalyst material as applied in the reforming catalyst used in this study. These three options can be applied independently of the horizontal or vertical filter design. The idea of placing a catalytic monolith or foam structure at the filter candle exit of a horizontal filter design was calculated to be unrealistic to implement because the monolith or foam structure would be too long to reach sulfur tar concentrations below 0.1 ppmV.

Process optimization questions arise regarding amount of catalyst, operating temperature, pressure drop, sorption material and performance loss of downstream equipment. The results presented in this study build a basis for the catalytic reformer process unit used in surrogate modeling [172].

5 Conclusion and outlook

5.1 Conclusion
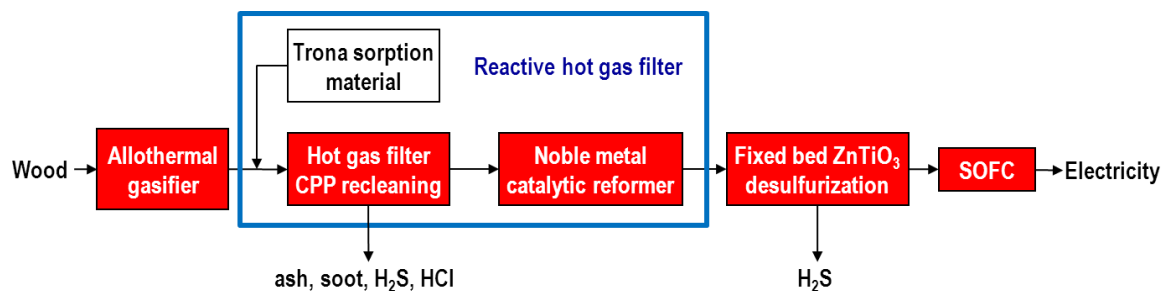
Figure 5.1: *Suggested HGC at 700 °C to 850 °C including reactive HGF for B-IGFC process chain*

Investigations on a reactive hot gas filtration (HGF) system consisting of HGF and catalytic reformer were conducted in order to implement a hot gas cleaning (HGC) process in thermo-chemical conversion processes from biomass to electricity, bio-SNG or liquid fuels.

Stable operation for more than 1000 h could be shown for a HGF system with coupled pressure pulse (CPP) recleaning system operated at 450 °C filtering particulate matter from an updraft wood gasifier.

A noble metal catalyst was found which is able to form H_2S out of sulfur bound in hydrocarbons at temperatures of 600 °C to 850 °C. The conversion to H_2S is needed because so far, high temperature desulfurization by sorption materials works for H_2S only, but not for sulfur tars.

Calculations based on the simulation of the tested reformer catalyst showed that besides other possibilities, an integration of a catalytic monolith at the exit of the HGF vessel is feasible.

Assuming that the presented HGF design works at temperatures of 850 °C, a reactive HGF system combining filter and catalyst, operating at exit temperatures of 850 °C, is possible.

To complete the reactive HGF system, literature suggests e.g. Trona (Na_2CO_3 $NaHCO_3$ $2H_2O$) to be used as high temperature sorption material upstream of the HGF. Bulk H_2S and HCl can be removed by Trona.

The complete HGC process includes a final desulfurization polishing step. Literature indicates that $ZnTiO_3$ can be applied for H_2S removal at high temperatures.

Figure 5.1 shows the suggested HGC including HGF for B-IGFC process chain.

5.2   Outlook

Further research is needed for the finalization of the design of a pilot-scale HGC process chain as suggested in Figure 5.1. It is planned to build a HGF unit operated at temperatures up to 850 °C at a 150 kW thermal input scale. It is not defined yet, if the HGF unit of the pilot plant will be realized in horizontal or vertical design because support for commercialization by industry is not given so far. Further cost clarifications are needed regarding a HGF operated at 850 °C. It has to be shown that higher costs for high temperature filter design can be offset by the higher efficiency of the HGC process.

The maximum temperature for the catalytic reformer tests was limited by the set-up of the test rig to 750 °C. A new test rig is installed enabling investigations on monolithic reactors at temperatures up to 900 °C under same conditions as presented in this thesis (chapter 4.1). Operating temperatures of 850 °C will enable the comparison with the simulation results presented in this thesis (chapter 4.5).

Sorption materials were not experimentally investigated during the course of this thesis. A follow-up project started investigating suitable high temperature sorption materials regarding inorganic impurities such as S, Na, K, P, As, Cd, Se. The sorption capacity of the filter cake regarding trace elements has to be investigated as well. Not included in the HGC as shown in Figure 5.1 is the removal of alkali compounds. Al_2O_3 is reported to remove K and Na from producer gas. A combination of Trona and Al_2O_3 as sorption materials has to be considered or an additional fixed bed reactor downstream of the HGF unit can be installed.

Process optimization questions arise regarding amount of catalyst, operating temperature, pressure drop, sorption material and performance loss of downstream equipment.

- Depending on required conversion rates of sulfur tars and sulfur free tars, the amount of catalyst and the operating temperature have to be set. The option of catalytic partial oxidation has to be considered if hot gas filter temperatures are below the required catalyst temperature.

- The application of catalytic partial oxidation will lower the heating value of the product gas, will increase the gas volume and dilute the gas by adding air.
- Depending on the way catalytic material will be integrated in the hot gas filter, the pressure drop will increase which could lead to higher operating costs.
- The quality and the amount of sorption material used upstream of the hot gas filter will influence the H_2S concentration in the product gas and therefore the catalyst activity. An optimization of the amount of catalyst and sorption material is needed.
- The operating temperature will also influence the performance of the sorption material. The amount of sorption material could influence the temperature of the product gas and the frequency of recleaning pulses of the hot gas filter.
- The financial investments in the hot gas cleaning equipment have to be financially valorized by the increase in the performance and the extension of life time of downstream equipment.

Process chain modeling and optimization should be able to give answers to these optimization questions. The results presented in this study build a basis for the catalytic reformer process unit used in surrogate modeling [172].

5.3   Recommendations for future work

5.3.1   HGF

- Recleaning intervals should be extended to at least 15 min in future experiments. Visual inspection of the filter candles confirmed the absence of patchy cleaning. This leads to the conclusion that 3 min cleaning intervals are too short in order to build a filter cake. Biomass input of 6.6 kW and intervals of 15 min would correspond to a filter load of 12 g m^{-2} which should be within the capabilities of the HGF. Even 24 g m^{-2}, corresponding to intervals of 30 min, should be working though the risk of bridge building between filter candles and filter vessel would increase.
- Recleaning depending on pressure drop over the filter wall should be considered. The sectors would be recleaned once a certain pressure threshold is passed for a given duration.
- Different pressure sensors should be installed with lower deviations to measure the pressure in the filter sectors during operation. This would allow

a better monitoring of the differential pressure increase over the filter wall during build-up of the filter cake.

- The frequency of the dynamic pressure measurements should be increased from 1'000 Hz to 5'000 Hz. This will permit a more precise data evaluation. Moving averages can be calculated without losing valuable information which facilitates easier data evaluation.

- Steam instead of nitrogen can be used as recleaning medium. This could make filter candle regeneration procedures obsolete.

- The influence of the filter material and the filter cake on the producer gas has to be investigated. In particular the influence on tar, sulfur, halide, alkali and trace element concentrations.

- The space behind baffle plates in the raw gas sector of the HGF should be filled with inert material that is stable at 450 °C in order to prevent filling of the void by particulate matter.

5.3.2 CPP Filter model

- Trying to improve the model accuracy by fitting resistance parameters could result in adapting the model to the specific filter design and decreasing the model's ability to calculate correct gas flows of other CPP filter designs. The model could be improved by implementing inertial terms (Ergun equation) for grain ceramic filter candles or simply by adjusting the filter permeability according to the filtration velocity and temperature. To do so, the pressure drop over the filter elements at different filtration velocities and temperatures has to be measured.

5.3.3 Catalytic conversion

- Assuming the catalyst offers one active site, it would make sense to invest more time to better understand the dependencies of WGS and STR of methane reactions to sulfur, steam, CO or C_2H_4. The same dependencies could then be applied to tar and sulfur tar decompositions if the reactions depend on the same active site.

- The results presented in this study could not find a dependence of the reaction rates on steam, CO or C_2H_4 content. The contents did not differ sufficiently, not enough experiments with consistent data were available or no adsorption of the mentioned species took place on the active sites

- The influence of steam concentration on conversion rates can be determined if low and high steam operating conditions are defined. First tests

showed that the lower steam concentration should be around 10 vol% and the higher around 40 vol% in order to find a clear influence.

- H_2S concentrations in the syngas have to be lower than 20 ppmV in order to detect an influence of H_2S on conversion rates as compared to a high H_2S concentration of 100 ppmV.

- Sulfur free experiments would help to better understand the influence of sulfur on tar conversion. As sulfur free conditions are very unlikely to exist in reality, sulfur free experiments were not conducted so far.

- The conversion of ethene has to be further investigated in order to discern between different decomposition pathways. Ethene can be decomposed by hydrogenation to ethane and further to methane, directly to methane or by steam reforming to CO and H_2. Since gas concentration of methane was not varied, it was not possible to discern the decomposition directly to methane or by hydrogenation to ethane. The reaction pathway from ethene to ethane by hydrogenation and further from ethane to methane by hydrogenation was considered. Parameters could not be estimated because the concentration of ethane measured after the reformer was smaller than the deviation of ethene concentration.

- The decomposition of benzene could not be observed in this thesis. Further experiments would be needed to investigate the decomposition of higher molecular hydrocarbons to benzene and the decomposition of benzene to lower molecular hydrocarbons.

- A complete catalyst characterization would include experiments with a monolith consisting of the catalyst support material only. This way it would be possible to differentiate between the influence of the catalyst carrier material and the active catalyst material.

- The data set of 149 experiments provided good confidence of the reproducibility and reliability of the sampling system and analytical system. Repeating experiments of well-defined operating conditions with tars and sulfur tars would complete the series of experiments. It would allow a statistical analysis of the system reproducibility.

- The ratio of the different tar and sulfur tar compounds can to be varied in order to investigate the influence of the single compounds on the conversion rates.

- A deactivation of the catalyst was not considered in this study. An experimental set-up with a higher degree of automation and increased safety measures would be needed enabling long term experiments. During 8 h experiments no catalyst deactivation could be observed.

- A different set-up that can be operated under pressure would also be required to confirm pressure dependencies of the reaction rates. Experiments were conducted at atmospheric pressure for this study. The pressure dependences are reflected in the partial pressures.

- The performance of the catalyst in the presence of other impurities contained in biomass derived producer gases such as NH_3, HCl or trace elements was not investigated so far.

- Connecting the reformer catalyst to the existing updraft wood gasifier downstream of the HGF could give insights to the catalyst performance with real wood gas.

- Apparent full conversion, where no molecules of a certain species could be detected downstream of the reformer, was limited by the LOD of the analytical equipment. Decreasing the corresponding LOD in the gas phase could be done by higher gas to liquid rations (increasing the concentration in the liquid phase). Reducing the LOD of the analytical equipment could maybe be done by improving the method of the GC. Otherwise more sensitive equipment is needed.

A Annex

A.1 Number of dynamic pressure measurements

Opening time set / Flush tank pressure	Offline: 0 m³ h⁻¹			Online 8.5 m³ h⁻¹			Online: 17 m³ h⁻¹		
[ms] / [hPa]	250	500	1000	250	500	1000	250	500	1000
cold (ambient) 25	7	7	6	9	6	8	6	7	6
50	7	7	7	6	10	7	7	7	7
100	7	14	7	8	7	6	6	6	7
200	2	1	0	1	1	1	0	1	1
hot (450°C) 25	8	13	8	2	4	3	2	2	1
50	8	8	7	2	4	2	2	2	2
100	6	8	4	2	5	1	3	2	2
200	2	2	0	2	2	0	3	2	0

Table A.1: *Number of dynamic pressure measurements conducted at different operating conditions*

A.2 Darcy's law for cylindrical elements

The general formula of Darcy's law describing the flow of a fluid through a porous medium is shown in Eq. A.1. The flow of the fluid (Q) equals the product of the permeability (K), the area (A) and the pressure drop (ΔP) divided by the viscosity of the fluid (η) and the thickness of the porous medium (L). Eq. A.2 shows the corresponding formula for the pressure drop calculation.

$$Q = -\frac{K * A * \Delta P}{\eta * L} \qquad\qquad \text{Eq. A.1}$$

$$\Delta P = -\frac{\eta}{K} * u * L \qquad\qquad \text{Eq. A.2}$$

The velocity (u) equals the volumetric flow (Q) divided by the area (A). The surface area at any point of the filter wall between the outter ($r_o = d_o/2$) and the inner ($r_i = d_i/2$) radius equals $2\pi r L_{fi}$. Assuming a constant flow and no changes in gas density, the flow is constant at any radius as shown in Eq. A.3. The corresponding velocity at any point of the filter wall is shown in Eq. A.4.

$$Q = u_0 d_0 \pi L_{fi} = u 2 r \pi L_{fi} \qquad\qquad \text{Eq. A.3}$$

$$u = \frac{u_0 d_0}{2r} \qquad\qquad \text{Eq. A.4}$$

The total pressure drop over the filter wall of cylindrical filter elements was calculated as shown in Eq. A.5.

$$\Delta P = \int_{d_i}^{d_o} \frac{\eta}{K} * \frac{u_0 d_0}{2r} * dr = \frac{\eta}{K} * \frac{u_0 d_0}{2} \int_{d_i}^{d_o} \frac{dr}{r} = \frac{\eta}{K} * \frac{u_0 d_0}{2} * \ln\left(\frac{d_0}{d_i}\right) \quad \text{Eq. A.5}$$

A.3   Parameters of CPP filter model

Gas flow	Parameters	Description	Literature		Set value
ft → rc	α_1	tube entrance	sharp-edged: 0.5 chamfered-edged: 0.25		0.25
	α_2	bend	90 °Bend, R/d = 4	laminar	$124*Re^{-0.7}$ (curve fitted)
			90 °Bend, R/d = 4 hydrolic plane up to k/d of 0.025	turbulent	$4.5*Re^{-0.24}$ hydrolic plane (curve fitted)
	λ_1	tube	$\lambda = \varphi*64/Re$	laminar	$64/Re$
			variety of equations depending on the range of Re	turbulent	$0.0054+0.396/Re^{0.3}$ hydrolic plane
	α_3	tube exit	for circular cross-section: 2.0	laminar	2.0
			0.7912 to 0.8466 depending on Re (hydrolic plane)	turbulent	0.8466
	Cv	valve flow coefficient	26.0		21 at 1000 hPa 22 at 750 hPa 23 at 500 hPa 26 at 250 hPa
s1 → s2	λ_2	circular orifice	$\lambda = Constant/Re$	laminar	$96/Re$
	α4	gap entrance	laminar: 0.3 - 0.5 turbulent: 0.05 - 0.5	laminar	0.4
	α_5	gap exit	laminar: 0.45 - 0.88 turbulent: 0.49 - 0.88		0.7
rc → S2	α_6	tube entrance (Borda collar)	sharp-edged: 3.0 chamfered-edged: 0.6 - 1.0		1.0
rc → rg	K_{fi}	specific filter permeability	$55*10^{-13}\,m^2$ (20°C, air)	DS 10-20	$55*10^{-13}\,m^2$
			$15*10^{-13}\,m^2$ (20°C, air)	DS 3-20	$15*10^{-13}\,m^2$
			$250*10^{-13}\,m^2$	TENMAT	$250*10^{-13}\,m^2$
rc → cg	α_7	orifice (sudden decrease in tube diameter)	Value depending on A2/A1: 0.05 - 1.5		Contratction number 0.61
rg → gf or cg → ex	α_8	tube entrance	sharp-edged: 0.5 chamfered-edged: 0.25		0.25
	λ_3	tube	$\lambda = \varphi*64/Re$	laminar	$64/Re$
			variety of equations depending on the range of Re	turbulent	$0.0054+0.396/Re^{0.3}$ hydrolic plane
	λ_4	intertial filter	$\lambda = \varphi*64/Re$	laminar	$64/Re$
			variety of equations depending on the range of Re	turbulent	$0.0054+0.396/Re^{0.3}$ hydrolic plane

Table A.2: *Parameters values as implemented in the CPP filter model with literature values for comparison*

A.4   Monolith simulation at high tar load
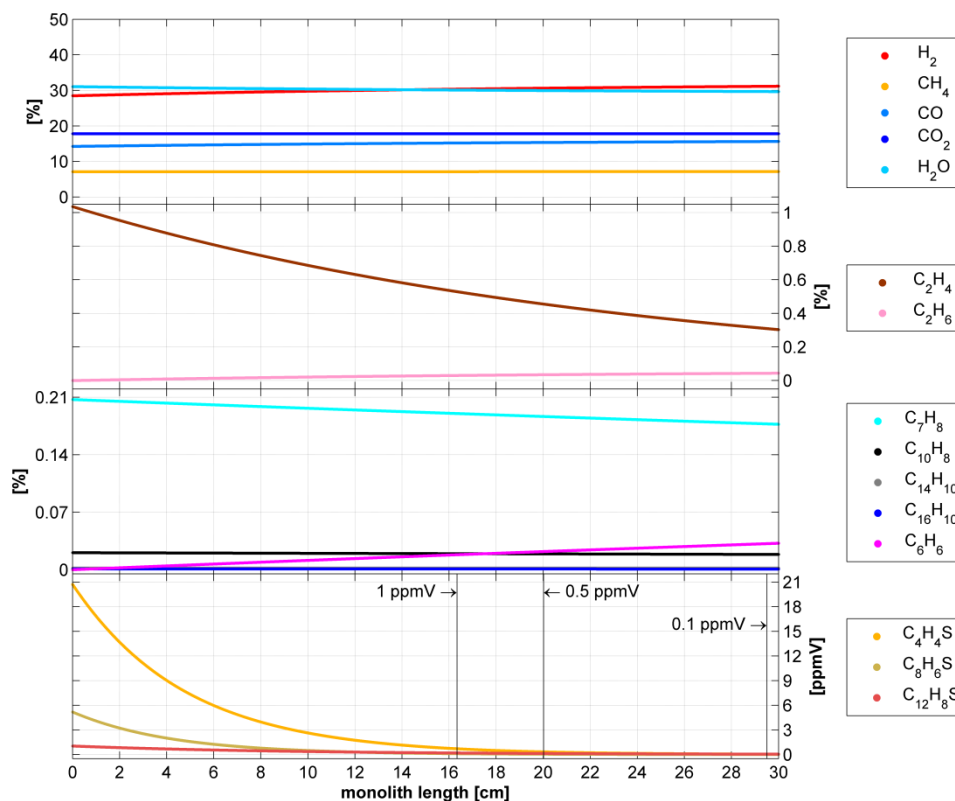
Figure A.1: *Model results of the change of gas composition over the length of the catalytic mono-lith at high tar load, low GHSV, 20 ppmV H_2S and at temperature of 600 °C*
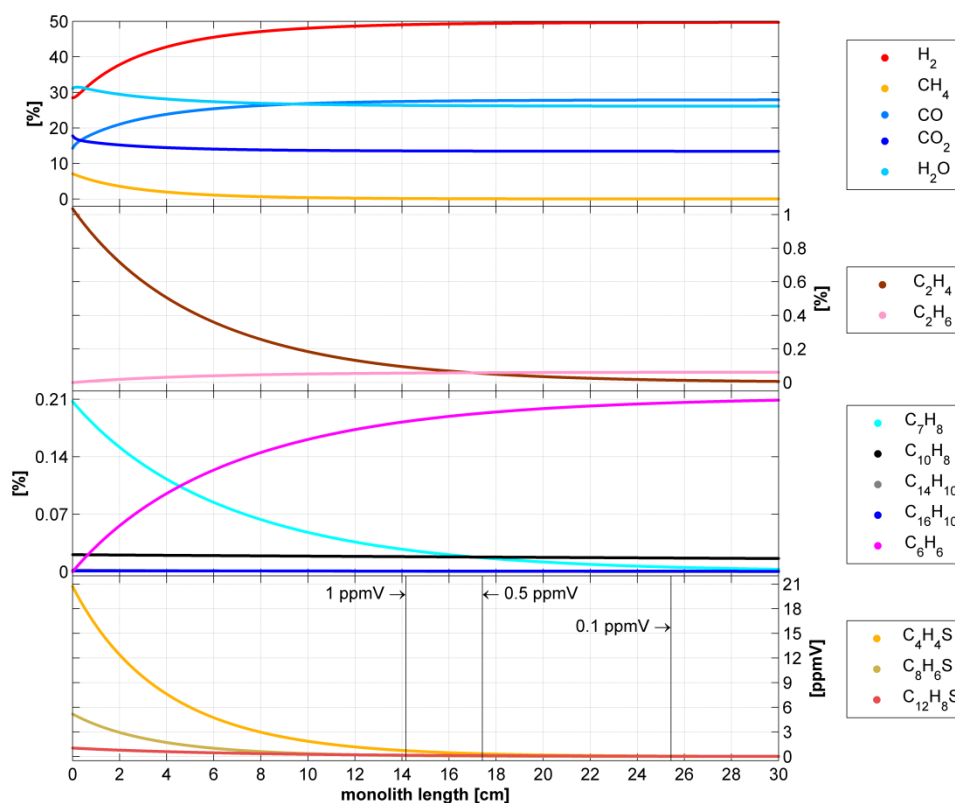
Figure A.2: *Model results of the change of gas composition over the length of the catalytic mono-lith at high tar load, low GHSV, 20 ppmV H_2S and at temperature of 850 °C*

A.5   Thermodynamic properties

Thermodynamic gas properties such as diffusion coefficient, heat capacity and gas viscosity are temperature and gas composition dependent. Therefore the properties were calculated at each monolith length. The van't Hoff equation as shown in Eq. A.6 was used to calculate the equilibrium constants (K_{eq}) of SRM and WGS reactions. The standard reaction enthalpy ($\Delta H_R°$) was calculated according to Eq. A.7. The reference temperature (T_0) equals 25 °C at standard conditions.

$$\frac{\partial \ln(K_{eq})}{\partial T} = \frac{\Delta H_R^0}{RT^2}$$
Eq. A.6

$$\Delta H_R(T) = \Delta H_R^0(T_0) + \int_{T_0}^{T} \nu_i c_{p,i}\, dT$$
Eq. A.7

The heat capacity (c_p) was calculated according to Eq. A.8. The coefficients A to E were provided by the Design Institute for Physical Properties database [173] and shown in Table A.3 for the compounds used during the tests presented in chapter 4.

$$c_{p,i} = A + B\left(\frac{C/T}{sinh(C/T)}\right)^2 + D\left(\frac{E/T}{cosh(E/T)}\right)^2$$
Eq. A.8

[J kmol^{-1} K^{-1}]	A	B	C	D	E	T$_{min}$ [K]	T$_{max}$ [K]
H$_2$	27617.0	9560.0	2466.0	3760.0	567.6	250	1500
CO	29108.0	8773.0	3085.1	8455.3	1538.2	60	1500
CO$_2$	29370.0	34540.0	1428.0	26400.0	588.0	50	5000
CH$_4$	33298.0	79933.0	2086.9	41602.0	992.0	50	1500
H$_2$O	33363.0	26790.0	2610.5	8896.0	1169.0	100	2273

Table A.3: *Coefficients for the calculation of heat capacities including temperature boundaries [173]*

The molecular diffusion coefficient of a species in a gas mixture ($D_{i,mix}$) was calculated according to Eq. A.9 [174] where (x_i) equals the molar fraction. The corresponding binary diffusion coefficients ($D_{i,j}$) were calculated according to Eq. A.10 [175]. Values of the molar mass (M) and the atomic diffusion volume (v) can be found in Table A.4 [175].

$$D_{i,mix} = \frac{1 - x_i}{\sum_j (x_i/D_{i,j})}$$
Eq. A.9

$$D_{i,j} = 0.01013 \left\{ \frac{T^{1.75}\left[(1/M_i) + (1/M_j)\right]^{0.5}}{P\left[(\sum v_i)^{1/3} + (\sum v_j)^{1/3}\right]^2} \right\} \qquad \text{Eq. A.10}$$

	v	M
	[m³ mol⁻¹]	[g mol⁻¹]
H_2	6.12	2.02
CO	18.00	28.01
CO_2	26.70	44.01
CH_4	25.14	16.04
H_2O	13.10	18.02
Ar	16.20	39.95
C_2H_4	41.04	28.05
C_2H_6	45.66	30.07
N_2	18.50	28.13
C_7H_8	111.48	92.14
$C_{10}H_8$	159.18	128.17
$C_{14}H_{10}$	227.40	178.23
$C_{16}H_{10}$	259.20	202.25
H_2S	27.52	34.08
COS	44.91	60.08
C_4H_4S	77.44	84.14
C_8H_6S	127.36	134.20
$C_{12}H_8S$	177.28	184.26

Table A.4: *Atomic diffusion volume and molar mass [175]*

	A	B	C	D	T_{min} [K]	T_{max} [K]
H_2	1.797E-07	0.6850	-0.59	140.0	13.95	3000
CO	1.113E-06	0.5338	94.7	0	68.15	1250
CO_2	2.148E-06	0.4600	290	0	194.67	1500
CH_4	5.255E-07	0.5901	105.67	0	90.69	1000
H_2O	1.710E-08	1.1146	0	0	273.16	1073.15
Ar	9.212E-07	0.6053	83.24	0	83.78	3273.1
C_2H_4	2.079E-06	0.4163	352.7	0	169.41	1000
C_2H_6	2.591E-07	0.6799	98.902	0	90.35	1000
N_2	6.559E-07	0.6081	54.714	0	63.15	1970
C_7H_8	8.727E-07	0.4940	323.79	0	178.18	1000
$C_{10}H_8$	6.432E-07	0.5389	400.16	0	353.43	1000
$C_{14}H_{10}$	4.348E-07	0.5272	238.27	0	372.38	1000
$C_{16}H_{10}$	4.050E-07	0.5278	250.93	0	423.81	1000
H_2S	3.931E-08	1.0134	0	0	250	480
COS	2.240E-05	0.2043	1373	0	134.3	1000

C_4H_4S	1.030E-07	0.5497	569.4	0	234.94	1000
C_8H_6S	6.529E-08	0.8528	71.853	0	304.5	1000
$C_{12}H_8S$	2.899E-08	0.9424	29.598	0	371.82	1000

Table A.5: *Coefficients for the calculation of viscosities including temperature boundaries [173]*

Dynamic viscosities of gas mixtures were calculated according to Eq. A.11 [176] with a binary, dimensionless constant ($\varphi_{i,j}$) according to Eq. A.12 and with gas viscosities of single components calculated according to Eq. A.13. Coefficients *A* to *D* were applied as shown in Table A.5 [173].

$$\eta_{mix} = \sum_i \frac{x_i \eta_i}{\sum_j (x_j \varphi_{i,j})} \qquad \text{Eq. A.11}$$

$$\varphi_{i,j} = \frac{\left[1 + (\eta_i/\eta_j)^{0.5} (M_j/M_i)^{0.25}\right]^2}{\left[8(1 + M_i/M_j)\right]^{0.5}} \qquad \text{Eq. A.12}$$

$$\eta_i = \frac{AT^B}{1 + (C/T) + (D/T^2)} \qquad \text{Eq. A.13}$$

Notation

Latin symbols

A	Area	[m^2]
a'	Specific surface area	[m^{-1}]
c	Concentration	[mol m^{-3}]
Ca	Carberry number	[-]
C_v	Flow coefficient of valve	[m^3 h^{-1}]
D	Diffusion	[m^2 s^{-1}]
d	Diameter	[m]
d_h	Hydraulic diameter	[m]
d_i	Inner diameter	[m]
d_o	Outer diameter	[m]
D	Diffusion	[m^2 s^{-1}]
Da_{II}	Dahmköhler number type II	[-]
D_k	Knudsen diffusion	[m^2 s^{-1}]
D_m	Molecular diffusion	[m^2 s^{-1}]
E_a	Apparent activation energy	[kJ mol^{-1}]
F	Molar flow	[mol s^{-1}]
G/L	Gas to liquid ratio (volume)	[-]
$GHSV$	Gas hourly space velocity	[h^{-1}]
ΔH	Heat of adsorption	[kJ mol^{-1}]
ΔH_R^0	Standard reaction enthalpy	[kJ mol^{-1}]
K	Adsorption constant	[Pa^{-1}]
K	Specific permeability	[m^2]
k	Rate constant	[s^{-1}]
K_0	Pre-exponential factor for adsorption constant (K)	[mol s^{-1} kg^{-1} bar^{-1}]
k_0	Pre-exponential factor for rate constant (k)	[mol s^{-1} kg^{-1} bar^{-1}]
k_f	Mass transfer coefficient	[m s^{-1}]
G	Geometric factor	[m]
L	Length	[m]
L_{wc}	Washcoat thickness (characteristic length)	[m]
M	Molar mass	[g mol^{-1}]
Ma	Mach	[-]
n	Number of moles	[mol]
$\dot{n}$	Molar flow	[mol s^{-1}]
N	Molar flow	[mol s^{-1}]

ΔP	Pressure drop	[Pa]
P	Pressure	[Pa]
p	Partial pressure	[Pa]
Q	Volume flow	[m^3 s^{-1}]
R	Gas constant (R = 8.314)	[J mol^{-1} K^{-1}]
r	Radius	[m]
r	Reaction rate	[mol s^{-1} kg$_{cat}^{-1}$]
Re	Reynolds number	[-]
Sc	Schmidt number	[-]
Sh	Sherwood number	[-]
T	Temperature	[K]
T_s	Sutherland constant	[K]
t	Time	[s]
t_0	Start time, t = 0 s	[s]
t_{close}	Point in time when valve completely closed	[s]
t_{hold}	Duration of valve completely open	[s]
t_{open}	Point in time when valve completely open	[s]
ToS	Time on stream	[h]
u	Velocity	[m s^{-1}]
V	Volume	[m^3]
v	Atomic diffusion volume	[m^3 mol^{-1}]
X	Conversion	[-]
x	Molar fraction	[-]

Greek symbols

α	Resistance coefficient	[-]
ε	Void fraction	[-]
η	Efficiency, effectiveness factor	[-]
η	Dynamic viscosity	[Pa s]
Θ	Permeability reduction factor	[-]
θ_E	Parameter for activation energy	[-]
θ_H	Parameter for heat of adsorption	[-]
θ_K	Kinetic parameter for adsorption constant	[mol s^{-1} kg^{-1} bar^{-1}]
θ_k	Kinetic parameter for rate constant	[mol s^{-1} kg^{-1} bar^{-1}]
κ	Isentropic exponent	[-]
λ	Friction factor	[-]
v	Kinematic viscosity	[m^2 s^{-1}]
ρ	Density	[kg m^{-3}]

τ	Tortuosity factor	[-]
Φ	Wheeler-Weisz modulus	[-]
ϕ	Thiele modulus	[-]
φ	Binary constant	[-]
Ψ	Contraction number	[-]
Ω	Filter area reduction factor	[-]

Superscripts

0	Standard conditions (T = 298.15 K, P = 101'325 Pa)
in	Inflow
n	Exponent
out	Outflow

Subscripts

0	Initial condition
ac	Activated sector
acc	Accumulation
b	Bulk
cat	Catalyst
ch	Channel
cg	Clean gas sector
cgex	Clean gas sector to filter exit
dc	Dust cake
di	Inner filter diameter
e	Electric
e	External
eq	Equilibrium
ex	Filter exit
eff	Effective
f	Fluid
fi	Filter
ft	Flush tank
ftrc	Flush tank to recleaning sector
gf	Gasifier
gfrg	Gasifier to raw gas sector
i	Incremental number
i	Inner

i	Internal
j	Incremental number
if	Inertial filter
m	monolith
max	Maximum
min	Minimum
mix	Mixture
n	Norm conditions (T_n = 273.15 K, P_n = 100'000 Pa)
o	Outer
or	Orifice
obs	Observed value
rc	Recleaning sector
rci	Recleaning intensity
ref	Reference
rg	Raw gas sector
s	Surface
s1	Sector 1
s2	Sector 2
tot	Total
tu	Tube
th	Thermal
v	Per volume
wc	Washcoat
x	Incremental number
y	Incremental number
z	Incremental number

Abbreviations

AC	Alternating current
AFC	Alkaline fuel cell
bdl	Below detection limit
BFB	Bubbling fluidized bed
B-IGFC	Biomass - integrated gasification fuel cell system
Bio-	Biomass
Bio-SNG	Biomass derived - synthetic natural gas
CC	Combined cycle
CFB	Circulating fluidized bed
CHP	Combined heat and power

CPO	Catalytic partial oxidation
CPP	Coupled pressure pulse
cpsi	Channels per square inch
DEN	Denominator
DFB	Dual fluidized bed
DOE	Department of Energy (U.S.)
dtf	dry tar free
Eq.	Equation
FB	Fluidized bed
FCC	Fluid catalytic cracking
FICFB	Fast internal circulating fluidized bed
FID	Flame ionization detector
FT	Fischer - Tropsch
GC	Gas chromatograph
µGC	Micro gas chromatograph
GC/FID	Gas chromatography with flame ionization detector
GC/SCD	Gas chromatograph sulfur chemiluminescence detector
HGC	Hot gas cleaning
HGF	Hot gas filtration
HPD	Highest probability density
HPR	Heat pipe reformer
IGFC	Integrated gasification fuel cell system
KF	Karl - Fischer
KIT	Karlsruhe Institute of Technology
LHHW	Langmuir-Hinshelwood-Hougen-Watson
LHV	Lower heating value
LOD	Limit of detection
LQ	Liquid quench
MCFC	Molten carbonate fuel cell
MDC	Maximum detectable conversion
nd	not detected
NETL	National energy technology laboratory
NGCC	Natural gas combined cycle
ORC	Organic Rankine cycle
PAFC	Phosphoric acid fuel cell
PAH	Poly aromatic hydrocarbon
PEMFC	Polymer electrolyte membrane fuel cell
PPI	Pores per inch
PSI	Paul Scherrer Institut
RDS	Rate determining step

RME	Rapeseed methyl ester
S	Sector
S	Sampling point
SCD	Sulfur chemiluminescence detector
SECA	Solid state energy conversion alliance
SNG	Synthetic natural gas
SOFC	Solid oxide fuel cells
SRM	Steam reforming of methane
TCD	Thermal conductivity detector
V	Valve
VDI	Verein Deutscher Ingenieure
WGS	Water gas shift

RME   Rapeseed methyl ester

References

[1] Nagel FP, Schildhauer TJ, Biollaz SMA. Biomass-integrated gasification fuel cell systems - Part 1: Definition of systems and technical analysis. International Journal of Hydrogen Energy 2009;34:6809

[2] Commission E. European Commission. EUROPE 2020, A strategy for smart, sustainable and inclusive growth. Communication from the Commission, Bruxelles, Belgium, 2010.; 2010.

[3] BFE BfE. Bundesamt für Energie BFE. Energiestrategie 2050: Erstes Massnahmenpaket. Schweizerische Eidgenossenschaft, Bern, Switzerland, 2011.; 2012.

[4] BFE BfE. Bundesamt für Energie BFE. Schweizerische Gesamtenergiestatistik 2011. Schweizerische Eidgenossenschaft, Bern, Switzerland, 2011.; 2012.

[5] BFE BfE. Bundesamt für Energie BFE. Grundlagen für die Energiestrategie des Bundesrates, Aktualisierung der Energieperspektiven 2035 (energiewirtschaftliche Modelle). Schweizerische Eidgenossenschaft, Bern, Switzerland, 2011.; 2011.

[6] BAFU BfU. Bundesamt für Umwelt BAFU. Jahrbuch Wald und Holz 2012. Schweizerische Eidgenossenschaft, Bern, Switzerland, 2012.; 2012.

[7] Andersson G, Boulouchos K, Bretschger L. Energiezukunft Schweiz 2011, ETH Zurich, Switzerland. 2011.

[8] Schweiz ET. Energie Trialog Schweiz. Energie-Strategie 2050, Impulse für die schweizerische Energiepolitik. Grundlagenbericht. Zurich, Switzerland. 2010.; 2010.

[9] Biollaz SMA. Biomass: Options for technical use. Renewable Energy Technologies I - Chapter 12. ETH Zurich; 2012.

[10] Leibold H, Hornung A, Seifert H. HTHP syngas cleaning concept of two stage biomass gasification for FT synthesis. Powder Technology 2008;180:265.

[11] Bridgwater AV. The technical and economic feasibility of biomass gasification for power generation. Fuel 1995;74:631.

[12] Kumar A, Jones DD, Hanna MA. Thermochemical Biomass Gasification: A Review of the Current Status of the Technology. Energies 2009;2:556.

[13] Ruiz Ja, Juárez MC, Morales MP, Muñoz P, Mendívil Ma. Biomass gasification for electricity generation: Review of current technology barriers. Renewable and Sustainable Energy Reviews 2013;18:174.

[14] REPOTEC - Renewable Power Technologies Umwelttechnik GmbH, Güssing, Austria.

[15] Hofbauer H, Rauch R, Bosch K, Reinhard K, Christian A. Biomass CHP Plant Güssing – A Success Story. Expert Meeting on Pyrolysis and Gasification of Biomass and Waste. Strasbourg, France; 2002.

[16]   hs energieanlagen GmbH F, Germany; http://www.hsenergie.eu. hs energieanlagen GmbH, Freising, Germany.

[17]   agnion technologies GmbH H, Germany; http://www.agnion.de. agnion technologies GmbH, Hettenshausen, Germany.

[18]   Dou B, Wang C, Chen H, Song Y, Xie B, Xu Y, et al. Research progress of hot gas filtration, desulphurization and HCl removal in coal-derived fuel gas: A review. Chemical Engineering Research and Design 2012:1.

[19]   Meng X, de Jong W, Pal R, Verkooijen AHM. In bed and downstream hot gas desulphurization during solid fuel gasification: A review. Fuel Processing Technology 2010;91:964.

[20]   Aravind PV, de Jong W. Evaluation of high temperature gas cleaning options for biomass gasification product gas for Solid Oxide Fuel Cells. Progress in Energy and Combustion Science 2012;38:737.

[21]   Pall Filtersystems GmbH C, Germany; http://www.pall.com/main/fuels-and-chemicals. Pall Filtersystems GmbH, Crailsheim, Germany.

[22]   Martin RA, Gardner B, Guan X, Hendrix H. Power Systems Development Facility: High Temperature, High Pressure Filtration in Gasification Operation. 5th International Symposium on Gas Cleaning at High Temperatures. Morgantown, USA; 2002, p. 1.

[23]   Kaufman-Rechulski MD. Catalysts for High Temperature Gas Cleaning in the Production of Synthetic Natural Gas from Biomass. EPFL; 2012, p. 270.

[24]   Pigeaud A, Maru H, Wilemski G, Helble J. Trace Element Emissions, Semi-annual report.: U.S. Department of Energy, Office of Fossil Energy, Morgantown, USA.; 1995.

[25]   Bao J, Krishnan GN, Jayaweera P, Lau K-H, Sanjurjo A. Effect of various coal contaminants on the performance of solid oxide fuel cells: Part II. ppm and sub-ppm level testing. Journal of Power Sources 2009;193:617.

[26]   Bao J, Krishnan GN, Jayaweera P, Perez-Mariano J, Sanjurjo A. Effect of various coal contaminants on the performance of solid oxide fuel cells: Part I. Accelerated testing. Journal of Power Sources 2009;193:607.

[27]   Bao J, Krishnan GN, Jayaweera P, Sanjurjo A. Effect of various coal gas contaminants on the performance of solid oxide fuel cells: Part III. Synergistic effects. Journal of Power Sources 2010;195:1316.

[28]   Marina OA, Pederson L, Gemmen R, Gerdes K, Finklea H, Celik I. Overview of SOFC Anode Interactions with Coal Gas Impurities. ECS Transactions 2010;26:363.

[29]   Gerdes K, Grol E, Keairns D, Newby R. Integrated Gasification Fuel Cell Performance and Cost Assessment. NETL: U.S. Department of Energy, National Energy Technology Laboratory; 2009.

[30]   Prantauer M, Hofmann A, Kreutner G, Huber MB. Tar reduction mechanisms on a non-catalytic hot gas filter in a biomass gasification plant. 19th European Biomass Conference and Exhibition. Berlin,Germany: ETA-Florence Renewable Energies; 2011, p. p. 1060.

[31] El-rub ZA. Biomass Char as an In-situ Catalyst for Tar Removal in Gasification Systems. Twente University, Enschede, The Netherlands; 2008.

[32] Dou B, Shen W, Gao J, Sha X. Adsorption of alkali metal vapor from high-temperature coal-derived gas by solid sorbents. Fuel Processing Technology 2003;82:51.

[33] Corella J, Toledo JM, Molina G. Performance of CaO and MgO for the hot gas clean up in gasification of a chlorine-containing (RDF) feedstock. Bioresource technology 2008;99:7539.

[34] Leibold H. Trockene Synthesegasreinigung bei hohen Temperaturen. Kolloquium Sustainable BioEconomy. Forschungszentrum Karlsruhe, Germany; 2008.

[35] Seifert H, Kolb T, Leibold H. Syngas aus Biomasse – Flugstromvergasung und Gasreinigung. 41 Kraftwerkstechnisches Kolloquium. Dresden, Germany; 2009.

[36] Tran K-Q, Iisa K, Steenari B-M, Lindqvist O. A kinetic study of gaseous alkali capture by kaolin in the fixed bed reactor equipped with an alkali detector. Fuel 2005;84:169.

[37] Turn SQ, Kinoshita CM, Ishimura DM, Hiraki TT, Zhou J, Masutani SM. An experimental investigation of alkali removal from biomass producer gas using a fixed bed sf solid sorbent. Industrial & Engineering Chemistry Research 2001;40:1960.

[38] Air products and Chemicals, Inc., Eastman Chemical Company. Removal of trace contaminants from coal-derived synthesis gas, Topical Report.: U.S. Department of Energy, National Energy Technology Laboratory, Morgantown, USA.; 2003.

[39] Leibold H, Mai R, Linek A, Zimmerlin B, Seifert H. Dry High Temperature Sorption of HCl and H2S with Natural Carbonates; GCHT-7, June 23-25, Newcastle, Australia 7th International Symposium & Exhibition, Gas Cleaning at High Temperatures (GCHT-7). Newcastle, Australia; 2008.

[40] VDI/DIN-Handbuch Reinhaltung der Luft Band 6, Filtering separators - High temperature gas filtration, VDI 3677 Blatt 3, Draft Version. Düsseldorf; 2010.

[41] Heidenreich S, Haag W, Mai R, Leibold H, Seifert H. Untersuchungen zur Abreinigungsleistung verschiedener Rückpulssysteme für Oberflächenfilter aus starren Filtermedien. Chemie Ingenieur Technik 2003;75:1280.

[42] Leubner H, Riebel U. Pulse Jet Cleaning of Textile and Rigid Filter Media–Characteristic Parameters. Chemical Engineering & Technology 2004;27:652.

[43] Sharma SD, Dolan M, Park D, Morpeth L, Ilyushechkin A, McLennan K, et al. A critical review of syngas cleaning technologies — fundamental limitations and practical problems. Powder Technology 2008;180:115.

[44] Mai R, Kreft D, Leibold H, Seifert H. Coupled Pressure Pulse (CPP) Recleaning of Ceramic Filter Candles Components and System Performance. 5th European Conference on Industrial Furnaces and Boilers (INFUB). Porto, Portugal; 2000.

[45]   Heidenreich S, Haag W, Mai R, Leibold H, Seifert H. Investigations on the Regeneration Intensity of Different Back-Pulse Systems for Surface Filters of Rigid Filter Media. Chemical Engineering & Technology 2004;27:502.

[46]   Mai R, Leibold H, Seifert H, Heidenreich S, Walch A. Coupled Pressure Pulse (CPP) Recleaning System for Ceramic Hot-Gas Filters with an Integrated Safety Filter. Chemical Engineering & Technology 2003;26:577.

[47]   Heidenreich S. Hot gas filtration – A review. Fuel 2013;104:83.

[48]   Mai R. Das Horizontalkonzept für die Hochtemperatur-Hochdruck-Filtration. Jahrestreffen der ProcessNet-Fachausschüsse Gasreinigung und Hochtemperaturtechnik. Frankfurt, Germany; 2011.

[49]   Leibold H. Trockene HT Synthesegasreinigung. 1 Nürnberger Fach-Kolloquium, Methanisierung und Second Generation Fuels. Nürnberg, Germany; 2012.

[50]   Simeone E, Nacken M, Haag W, Heidenreich S, de Jong W. Filtration performance at high temperatures and analysis of ceramic filter elements during biomass gasification. Biomass and Bioenergy 2011;35:87.

[51]   Simeone E, Siedlecki M, Nacken M, Heidenreich S, De Jong W. High temperature gas filtration with ceramic candles and ashes characterisation during steam–oxygen blown gasification of biomass. Fuel 2011.

[52]   Chuah TG, Seville JPK. Measuring and Modeling the Performance of Rigid Ceramic Filters. AJChE 2002;2:87.

[53]   Christ A, Renz U. Numerical Simulation of Single Ceramic Filter Element Cleaning. PARTEC; 1995, p. 728.

[54]   Li H, Ji Z, Wu X, Choi J-H. Numerical analysis of flow field in the hot gas filter vessel during the pulse cleaning process. Powder Technology 2007;173:82.

[55]   Mai R, Fronhöfer M. Recleaning of Filter Candles by Fast Pressure Decrease on the Raw Gas Side. PARTEC; 1995, p. 301.

[56]   Gamwo IK, Halow JS, Ahmadi G. Nonisothermal Simulation of Flows in the Hot-Gas Filter Vessel at Wilsonville. Particulate Science and Technology 2002;20:45.

[57]   Mazaheri AR, Ahmadi G, Gamwo IK. Hot-gas flow and particle transport and deposition in a candle filter vessel. Advanced Powder Technology 2003;14:111.

[58]   Tanthapanichakoon W, Charinpanitkul T, Jintaworn W, Laksameearunotai J, Amornkitbamrung M, Fukui T, et al. CFD investigation of high-temperature gas filtration using twin ceramic candles. Powder Technology 2008;180:2110.

[59]   Ahmadi G, Smith DH. Analysis of steady-state filtration and backpulse process in a hot-gas filter vessel. Aerosol Science and Technology 2002;36:665.

[60]   Koch M, Krammer G. The Permeability Distribution (PD) Method for Filter Media Characterization. Aerosol Science and Technology 2008;42:433.

[61]   Christ A, Renz U. Numerical Simulation of Filter Cake Build-up on Surface Filters. PARTEC; 1995, p. 169.

[62]   Chuah TG, Seville JPK. Numerical Simulation of Dust Cake Build-up in Rigid Ceramic Filters. Industrial & Engineering Chemistry 2004;10:321.

[63]   Dittler A, Ferer MV, Mathur P, Djuranovic P, Kasper G, Smith DH. Patchy cleaning of rigid gas filters - transient regeneration phenomena comparison of modelling to experiment. Powder Technology 2002;124:55.

[64]   Dittler A, Kasper G. Measurement of Local Frequencies of Filter Regeneration and their Effect on Successive Operating Cycles. 5th International Symposium on Gas Cleaning at High Temperatures. Morgantown, USA; 2002.

[65]   Döring N, Meyer J, Kasper G. The influence of cake residence time on the stable operation of a high-temperature gas filter. Chemical Engineering Science 2009;64:2483.

[66]   Duo W, Kirkby NF, Seville JPK, Clift R. Patchy cleaning of rigid gas filters - I. A probabilistic model. Chemical Engineering Science 1997;52:141.

[67]   Duo W, Seville JPK, Kirkby NF, Biichele H, Cheung CK. Patchy cleaning of rigid gas filters - II. Experiments and model validation. Chemical Engineering Science 1997;52:153.

[68]   Theliander H, Fathi-Najafi M. Simulation of the Build-up of a Filter Cake. Filtech Europa 95. Karlsruhe, Germany; 1995.

[69]   Stöcklmayer C, Höflinger W. Simulation of the filtration behaviour of dust filters. Simulation Practice and Theory 1998;6:281.

[70]   Tiller FM, Kirby JM, Nguyen HL. Approximate Theory for Radial Filtration/Consolidation. Journal of Geotechnical Engineering 1996:797.

[71]   Neiva ACB, Goldstein L. A procedure for calculating pressure drop during the build-up of dust filter cakes. Chemical Engineering and Processing 2003;42:495.

[72]   Rudnick SN, First MW. Specific Resistance of Filter Dust Cakes: Comparison of Theory and Experiments. 3rd Symposium on Fabric Filters for Particle Collection. Tuscon, USA; 1977, p. 251.

[73]   Schmidt E. Experimental Investigations into the Compression of Dust Cakes Deposited on Filter Media. Filtration & Separation 1995:789.

[74]   Schmidt E. Theoretical Investigations into the Compression of Dust Cakes Deposited on Filter Media. Filtration & Separation 1997:365.

[75]   Hata M, Furuuchi M, Kanaoka C. Analysis of pulse-jet cleaning of dust cake from ceramic filter element. 5th International Symposium on Gas Cleaning at High Temperature. Morgantown, USA; 2002.

[76]   Laux S. Druckstossabreinigung keramischer Filterelemente zur Heissgasfiltration, Dissertation. RWTH Aachen; 1994, p. 132.

[77]   Berbner S. Zur Druckstossregenerierung keramischer Filterelemente bei der Heissgasreinigung. Universität Karlsruhe (Technische Hochschule); 1995, p. 74.

[78] Huque Z, Mei D, Zhou J. Characterization and Failure Analysis of Ceramic Filters Utilized For Emission Control During Coal Gasification. Final Technical Report: DOE; 1998.

[79] Mai R, Heidenreich S, Leibold H, Seifert H, Haag W. Operation Behavior of a Multi-Candle Filter with Coupled Pressure Pulse Recleaning during Normal Operation and in the Case of a Filter Candle Failure. 5th International Symposium on Gas Cleaning at High Temperature; 2002.

[80] Heidenreich S, Walch A, Mai R, Haag W, Scheibner B, Leibold H, et al. Ceramic Hot Gas Filter with Integrated Failsafe System. 5th International Symposium on Gas Cleaning at High Temperatures. Morgantown, USA; 2002.

[81] Nagel FP, Ghosh S, Pitta C, Schildhauer TJ, Biollaz SMA. Biomass integrated gasification fuel cell systems–Concept development and experimental results. Biomass and Bioenergy 2011;35:354.

[82] Draelants DJ, Zhao H, Baron GV. Preparation of Catalytic Filters by the Urea Method and Its Application for Benzene Cracking in H2S-Containing Biomass Gasification Gas. Industrial & Engineering Chemistry Research 2001;40:3309.

[83] Engelen K, Zhang Y, Draelants DJ, Baron GV. A novel catalytic filter for tar removal from biomass gasification gas: Improvement of the catalytic activity in presence of H2S. Chemical Engineering Science 2003;58:665.

[84] Ma L, Verelst H, Baron GV. Integrated high temperature gas cleaning: Tar removal in biomass gasification with a catalytic filter. Catal Today 2005;105:729.

[85] Nacken M, Ma L, Heidenreich S, Baron GV. Catalytic Activity in Naphthalene Reforming of Two Types of Catalytic Filters for Hot Gas Cleaning of Biomass-Derived Syngas. Industrial & Engineering Chemistry Research 2010;49:5536.

[86] Nacken M, Ma L, Heidenreich S, Verpoort F, Baron GV. Development of a catalytic ceramic foam for efficient tar reforming of a catalytic filter for hot gas cleaning of biomass-derived syngas. Applied Catalysis B: Environmental 2012;125:111.

[87] Rapagnà S, Gallucci K, Di Marcello M, Foscolo PU, Nacken M, Heidenreich S, et al. First Al2O3 based catalytic filter candles operating in the fluidized bed gasifier freeboard. Fuel 2012;97:718.

[88] Rönkkönen H, Simell P, Niemelä M, Krause O. Precious metal catalysts in the clean-up of biomass gasification gas part 2: Performance and sulfur tolerance of rhodium based catalysts. Fuel Processing Technology 2011;92:1881.

[89] Rönkkönen H, Simell P, Reinikainen M, Krause O, Niemelä MV. Catalytic clean-up of gasification gas with precious metal catalysts – A novel catalytic reformer development. Fuel 2010;89:3272.

[90] Rönkkönen H, Simell P, Reinikainen M, Niemelä M, Krause O. Precious metal catalysts in the clean-up of biomass gasification gas Part 1: Monometallic catalysts and their impact on gasification gas composition. Fuel Processing Technology 2011;92:1457.

[91] Toledo JM, Corella J, Molina G. Catalytic Hot Gas Cleaning with Monoliths in Biomass Gasification in Fluidized Beds. 4. Performance of an Advanced, Second-Generation, Two-Layers-Based Monolithic Reactor. Industrial & Engineering Chemistry Research 2006;45:1389.

[92] Tomishige K, Miyazawa T, Asadullah M, Ito S-i, Kunimori K. Catalyst performance in reforming of tar derived from biomass over noble metal catalysts. Green Chemistry 2003;5:399.

[93] Zhao H, Draelants DJ, Baron GV. Performance of a Nickel-Activated Candle Filter for Naphthalene Cracking in Synthetic Biomass Gasification Gas. Industrial & Engineering Chemistry Research 2000;39:3195.

[94] Pfeifer C, Hofbauer H. Development of catalytic tar decomposition downstream from a dual fluidized bed biomass steam gasifier. Powder Technology 2008;180:9.

[95] Rönkkönen H, Rikkinen E, Linnekoski J, Simell P, Reinikainen M, Krause O. Effect of gasification gas components on naphthalene decomposition over ZrO2. Catal Today 2009;147:S230.

[96] Furusawa T, Tsutsumi A. Comparison of Co/MgO and Ni/MgO catalysts for the steam reforming of naphthalene as a model compound of tar derived from biomass gasification. Applied Catalysis A: General 2005;278:207.

[97] Furusawa T, Saito K, Kori Y, Miura Y, Sato M, Suzuki N. Steam reforming of naphthalene/benzene with various types of Pt- and Ni-based catalysts for hydrogen production. Fuel 2013;103:111.

[98] Cui H, Turn SQ, Keffer V, Evans D, Tran T, Foley M. Contaminant Estimates and Removal in Product Gas from Biomass Steam Gasification. Energy & Fuels 2010;24:1222.

[99] Nacken M, Ma L, Heidenreich S, Baron GV. Performance of a catalytically activated ceramic hot gas filter for catalytic tar removal from biomass gasification gas. Applied Catalysis B: Environmental 2009;88:292.

[100] Rapagna S, Gallucci K, Di Marcello M, Foscolo PU, Nacken M, Heidenreich S. In Situ Catalytic Ceramic Candle Filtration for Tar Reforming and Particulate Abatement in a Fluidized-Bed Biomass Gasifier. Energy & Fuels 2009;23:3804.

[101] Rapagna S, Gallucci K, Di Marcello M, Matt M, Nacken M, Heidenreich S, et al. Gas cleaning, gas conditioning and tar abatement by means of a catalytic filter candle in a biomass fluidized-bed gasifier. Bioresource technology 2010;101:7134.

[102] Corella J, Toledo JM, Padilla R. Catalytic hot gas cleaning with monoliths in biomass gasification in fluidized beds. 1. Their effectiveness for tar elimination. Industrial & Engineering Chemistry Research 2004;43:2433.

[103] Corella J, Toledo JM, Padilla R. Catalytic hot gas cleaning with monoliths in biomass gasification in fluidized beds. 2. Modeling of the monolithic reactor. Industrial & Engineering Chemistry Research 2004;43:8207.

[104] Corella J, Toledo JM, Padilla R. Catalytic hot gas cleaning with monoliths in biomass gasification in fluidized beds. 3. Their effectiveness for ammonia elimination. Industrial & Engineering Chemistry Research 2005;44:2036.

[105] Toledo JM, Corella J, Molina G. Catalytic hot gas cleaning with monoliths in biomass gasification in fluidized beds. 4. Performance of an advanced, second-generation, two-layers-based monolithic reactor. Industrial & Engineering Chemistry Research 2006;45:1389.

[106] Gallmetzer G, Ackermann P, Schweiger A, Kienberger T, Gröbl T, Walter H, et al. The agnion Heatpipe-Reformer—operating experiences and evaluation of fuel conversion and syngas composition. Biomass Conversion and Biorefinery 2012:207.

[107] Kurkela E, Kurkela M. Advanced Biomass Gasification for High-Efficiency Power. VTT Research notes 2511 2009;Publishable Final Activity Report of BiGPower Project.

[108] Rönkkönen H, Simell P, Reinikainen M, Krause O. The Effect of Sulfur on ZrO2-Based Biomass Gasification Gas Clean-Up Catalysts. Topics in Catalysis 2009;52:1070.

[109] Viinikainen T, Rönkkönen H, Bradshaw H, Stephenson H, Airaksinen S, Reinikainen M, et al. Acidic and basic surface sites of zirconia-based biomass gasification gas clean-up catalysts. Applied Catalysis A: General 2009;362:169.

[110] Leppin D, Basu A. Novel Bio-Syngas Cleanup Process. Presentation to ICPS09. Gas Technology Institute, Chicago USA; 2009.

[111] Horvath A. Operating Experience with Biomass Gasifiers, Needs to Improve Gasification Plant Operation. IEA Task 33 Workshop. Breda, Netherlands; 2009.

[112] Varga C, Koppatz S, Pfeifer C, Hofbauer H. Hot gas cleaning of biomass derived syngas by catalytic filter candles. 18th European Biomass Conference. Lyon, France: ETA-Florence Renewable Energies; 2010, p. 762.

[113] Zuercher S, Pabst K, Schaub G. Ceramic foams as structured catalyst inserts in gas–particle filters for gas reactions—Effect of backmixing. Applied Catalysis A: General 2009;357:85.

[114] Biollaz SMA, Jenne M, Schildhauer TJ, Nagel FP. Method and Plant for converting solid biomass into electricity. 2008, p. 30.

[115] Heidenreich S, Nacken M, Hackel M, Schaub G. Catalytic filter elements for combined particle separation and nitrogen oxides removal from gas streams. Powder Technology 2008;180:86.

[116] UNIQUE, EC 7th Framework Programm, Theme: Energy.

[117] CHRISGAS - Fuels from Biomass, EC 6th Framework Programm.

[118] Simeone E, Hölsken E, Nacken M, Heidenreich S, De Jong W. Study of the Behaviour of a Catalytic Ceramic Candle Filter in a Lab-Scale Unit at High Temperatures. Int J Chem React Eng 2010;8.

[119] Simeone E, Pal R, Nacken M, Heidenreich S, Verkooijen AHM. Tar removal in a catalytic ceramic candle filter unit at high temperatures. 18th European Biomass Conference and Exhibition. Lyon, France: ETA-Florence Renewable Energies; 2010, p. 1.

[120] EG&G Technical Services Inc. Fuel Cell Handbook. 7th ed; 2004.

[121] Rabis A, Rodriguez P, Schmidt TJ. Electrocatalysis for Polymer Electrolyte Fuel Cells: Recent Achievements and Future Challenges. ACS Catalysis 2012;2:864.

[122] Hexis AG W, Schweiz, www.hexis.com. Hexis AG, Winterthur, Schweiz.

[123] Biollaz SMA, Hottinger P, Pitta C, Karl J. Results from a 1200 hour test of a tubular SOFC with woodgas. 17th European Biomass Conference and Exhibition. Hamburg, Germany: ETA-Florence Renewable Energies; 2009.

[124] Office of Fossil Energy, Fuel Cell Program - Annual Report 2012. U.S. DOE, NETL, Solide State Energy Conversion Alliance (SECA); 2012.

[125] White B. DOE Solide Oxide Fuel Cell Programm Status. U.S. Department of Energy, National Energy Technology Laboratory; 2012.

[126] Hossein G-A. Progress in SECA Coal-Based Program. 12 th Annual SECA Workshop. Pittsburgh, USA; 2011.

[127] Cayan FN, Zhi M, Pakalapati SR, Celik IB, Wu N, Gemmen R. Effects of coal syngas impurities on anodes of solid oxide fuel cells. Journal of Power Sources 2008;185:595.

[128] Hernández SP, Scarpa F, Fino D, Conti R. Biogas purification for MCFC application. International Journal of Hydrogen Energy 2011;36:8112.

[129] Li TS, Xu C, Chen T, Miao H, Wang WG. Chlorine contaminants poisoning of solid oxide fuel cells. Journal of Solid State Electrochemistry 2010;15:1077.

[130] Nagel FP, Schildhauer TJ, Sfeir J, Schuler A, Biollaz SMA. The impact of sulfur on the performance of a solid oxide fuel cell (SOFC) system operated with hydrocarboneous fuel gas. Journal of Power Sources 2009;189:1127.

[131] Thijssen J. Solid Oxide Fuel Cells and Critical Materials : A Review of Implications. U.S. Department of Energy, National Energy Technology Laboratory; 2011.

[132] Xu C, Zondlo JW, Finklea HO, Demircan O, Gong M, Liu X. The effect of phosphine in syngas on Ni-YSZ anode-supported solid oxide fuel cells. Journal of Power Sources 2009;193:739.

[133] Hauth M, Lerch W, König K, Karl J. Impact of naphthalene on the performance of SOFCs during operation with synthetic wood gas. Journal of Power Sources 2011;196:7144.

[134] Hofmann P, Panopoulos KD, Aravind PV, Siedlecki M, Schweiger A, Karl J, et al. Operation of solid oxide fuel cell on biomass product gas with tar levels >10 g Nm-3. International Journal of Hydrogen Energy 2009;34:9203.

[135] Mermelstein J, Millan M, Brandon NP. The interaction of biomass gasification syngas components with tar in a solid oxide fuel cell and operational conditions to mitigate carbon deposition on nickel-gadolinium doped ceria anodes. Journal of Power Sources 2011;196:5027.

[136] Nagel FP, Jenne M, Biollaz SMA, Stucki S. Link-up of a 1kW-SOFC with an updraft-wood gasifier via hot gas processing. 15th European Biomass

Conference & Exhibition. Berlin, Germany: ETA-Florence Renewable Energies; 2007.

[137] Villano SM, Hoffmann J, Carstensen H-H, Dean AM. Selective removal of ethylene, a deposit precursor, from a "dirty" synthesis gas stream via gas-phase partial oxidation. The journal of physical chemistry A 2010;114:6502.

[138] Frank N, Saule M, Karl J. BioCellus - Biomass Fuel Cell Utility System, D810 Project summary. D810 Project summary. STREP Sustainable Energy Systems: Technische Universität München; 2008.

[139] Martini S, Kleinhappl M, Hofbauer H. High temperature gas treatment for the operation of a solid oxide fuel cell (SOFC). 17th European biomass conference & exhibition. Hamburg, Germany: ETA-Florence Renewable Energies; 2009.

[140] Frank N, Saule M, Karl J, Schweiger A, Hohenwarter U. Performance of Tubular SOFCs on Syngas from Wood Gasification. 15th European Biomass Conference & Exhibition. Berlin, Germany: ETA-Florence Renewable Energies; 2007.

[141] Karellas S, Karl J, Kakaras E. An innovative biomass gasification process and its coupling with microturbine and fuel cell systems. Energy 2008;33:284.

[142] Hofmann P, Schweiger A, Fryda L, Panopoulos KD, Hohenwarter U, Bentzen JD, et al. High temperature electrolyte supported Ni-GDC/YSZ/LSM SOFC operation on two-stage Viking gasifier product gas. Journal of Power Sources 2007;173:357.

[143] Nagel FP. Electricity from wood through the combination of gasification and solid oxide fuel cells, Systems analysis and Proof-of-concept. ETH Zurich; 2008, p. 328.

[144] TENMAT LTD M, England; www.tenmat.com/Content/HotGasFiltration. TENMAT LTD, Manchester, England.

[145] Mai R, Leibold H, Seifert H. Regeneration von starren Filterelementen mittels Druckimpuls und Rückspülen - Einfluss des Staubschichtwider-standes auf das Abreinigungsverhalten. VDI-GVC-Fachausschusssitzung Gasreinigung. Würzburg, Germany; 2006.

[146] Bohl W, Elmendorf W. Technische Strömungslehre. Würzburg: Vogel; 2008.

[147] Stampa B. Experimentelle Untersuchungen an axial durchströmten Ringspalten. Clausthal-Zellerfeld : Bönecke: TU Braunschweig; 1971, p. 157.

[148] Ergun S. Fluid flow through packed columns. Chemical Engineering Progress 1952;48:89.

[149] Fluidic characteristic quantities of control valves and their determination. VDI/VDE Handbuch Mess- und Automatisierungstechnik, Band 3: Automatisierungstechnik, VDI 2173 2007.

[150] Richardson JT, Peng Y, Remue D. Properties of ceramic foam catalyst supports : pressure drop. Applied Catalysis A: General 2000;204:19.

[151] Bennett BAV, McEnally CS, Pfefferle LD, Smooke MD, Colket MB. Computational and experimental study of axisymmetric coflow partially premixed ethylene/air flames. Combustion and Flame 2001;127:2004.

[152] Dong GL, Huttinger KJ. Consideration of reaction mechanisms leading to pyrolytic carbon of different textures. Carbon 2002;40:2515.

[153] Corella J, Aznar MP, Caballero MA, Gil J. Biomass gasifcation in atmospheric and bubbling fluidized bed : Effect of the type of gasifying agent on the product distribution. Biomass and Bioenergy 1999;17:389.

[154] Thunman H, Seemann MC. First experiences with the new chalmers gasifier. Proceedings of the 20th International Conference on Fluidized Bed Combustion: Springer Berlin Heidelberg; 2010, p. 659.

[155] Devi L, Ptasinski KJ, Janssen FJJG. Decomposition of Naphthalene as a Biomass Tar over Pretreated Olivine: Effect of Gas Composition, Kinetic Approach, and Reaction Scheme. Industrial & Engineering Chemistry Research 2005;44:9096.

[156] Li C, Suzuki K. Tar property, analysis, reforming mechanism and model for biomass gasification—An overview. Renewable and Sustainable Energy Reviews 2009;13:594.

[157] Milne TA, Evans RJ. Biomass Gasifier " Tars ": Their Nature , Formation , and Conversion. National Renewable Energy Laboratory; 1998.

[158] Rhyner U, Schildhauer TJ, Biollaz SMA. Catalytic Conversion of Tars in a Monolith in the Presence of H2S at 750°C. 19th European Biomass Conference & Exhibition. Berlin, Germany: ETA-Florence Renewable Energies; 2011.

[159] Bihr S, Rechulski M, Schneebeli J, Biollaz SMA. Sulphur diagnostics in product gases at high and very low concentrations: A contribution to a future "sulphur protocol". In: Florence E, editor. 18th European Biomass Conference and Exhibition. Lyon, France: ETA-Florence Renewable Energies; 2010.

[160] Kaufman-Rechulski MD, Schneebeli J, Geiger S, Schildhauer TJ, Biollaz SMa, Ludwig C. Liquid-Quench Sampling System for the Analysis of Gas Streams from Biomass Gasification Processes. Part 1: Sampling Noncondensable Compounds. Energy & Fuels 2012;26:7308.

[161] Kaufman-Rechulski MD, Schneebeli J, Geiger S, Schildhauer TJ, Biollaz SMa, Ludwig C. Liquid-Quench Sampling System for the Analysis of Gas Streams from Biomass Gasification Processes. Part 2: Sampling Condensable Compounds. Energy & Fuels 2012;26:6358.

[162] Norinaga K, Sakurai Y, Sato R, Hayashi J-i. Numerical simulation of thermal conversion of aromatic hydrocarbons in the presence of hydrogen and steam using a detailed chemical kinetic model. Chemical Engineering Journal 2011;178:282.

[163] Hawthorn RD. Afterburner catalysts-effects of heat and mass transfer between gas and catalyst surface. AIChE Symposium Series 1974;70:428.

[164] Hayes RE, Kolaczkowskib ST, Li PKC, Awdry S. Evaluating the effective diffusivity of methane in the washcoat of a honeycomb monolith. Appl Catal B-Environ 2000;25:93.

[165] van Santen RA, van Leeuwen PWNM, Moulijn JA, Averill BA. Catalysis: An integrated approach. 2nd, revised and enlarged ed. Amsterdam: Elsevier; 1999.

[166] Hayes RE, Liu B, Moxom R, Votsmeier M. The effect of washcoat geometry on mass transfer in monolith reactors. Chemical Engineering Science 2004;59:3169.

[167] Stewart WE, Caracotsios M. Computer-aided modeling of reactive systems. Hoboken, N.J.: Wiley-Interscience : AIChE; 2008.

[168] Stewart WE, Caracotsios M, Sorensen JP. Parameter-Estimation from Multiresponse Data. Aiche Journal 1992;38:641.

[169] Schildhauer TJ, Pangarkar K, van Ommen JR, Nijenhuis J, Moulijn JA, Kapteijn F. Heat transport in structured packings with two-phase co-current downflow. Chemical Engineering Journal 2012;185-186:250.

[170] Twigg MV, Richardson JT. Preparation and properties of ceramic foam catalyst supports. Studies in Surface Science and Catalysis 1995;91:345.

[171] Ratcliff CM, Bain R. Fuel Cell Integration – A Study of the Impacts of Gas Quality and Impurities Milestone Completion Report. NREL 2001.

[172] Gassner M, Marechal F. Thermo-economic process model for thermochemical production of Synthetic Natural Gas (SNG) from lignocellulosic biomass. Biomass Bioenerg 2009;33:1587.

[173] DIPPR Project 801. Design Institute for Physical Properties; 2005.

[174] Wilke CR, Lee CY. Estimation of Diffusion Coefficients for Gases and Vapors. Industrial & Engineering Chemistry 1955;47:1253.

[175] Fuller EN, Schettler PD, Giddings JC. New method for prediction of binary gas-phase diffusion coefficients. Industrial & Engineering Chemistry 1966;58:18.

[176] Wilke CR. A viscosity equation for gas mixtures. The Journal of Physical Chemistry 1950;18:517.

Curriculum Vitae

Personal data:

First name: Urs

Family name: Rhyner

Date of birth: 30.03.1978

Nationality: Swiss

Education:

Jun 2009 - Mar 2013   Paul Scherrer Institut (PSI), Villigen
                       General Energy Department, Doctorate studies

Nov 2004 - Feb 2005   Massachusetts Institute of Technology (MIT), USA
                       Department of Material Science and Engineering: Diploma thesis

Oct 2003 - Oct 2004   Swiss Federal Institute of Technology (ETH) Zurich
                       Diploma/MSc in Material Science completed in March 2005

Oct 2001 - Aug 2002   Ecole Polytechnique Fédéral de Lausanne (EPFL)
                       Department of Material Science: Exchange year

Oct 1999 - Sep 2001   Swiss Federal Institute of Technology (ETH) Zurich
                       Department of Material Science: 1. and 2. intermediate diploma

Sep 1991 - May 1998   Gymnasium Stiftsschule Einsiedeln
                       Matura Type B (Latin, History)

Work experience:

Dec 2008 - May 2009   Nomura Bank Switzerland, Zurich
                       Capital Markets, Structured Solutions Group: Development of fixed income derivative
                       solutions for Swiss institutional clients

May 2005 - Oct 2008   Lehman Brothers International, Zurich
                       Capital Markets, Fixed Income Sales: Structuring and marketing of fixed income deriv-
                       atives and alternative investments for Swiss institutional clients

Other activities:

Jul 2010 - current   Communal Councilor
                       Minister of Finance of Feusisberg SZ

List of publications:

Rhyner U, Mai R, Leibold H, Biollaz SMA. Dynamic pressure measurements of a hot gas filter as a diagnostic tool to assess the time dependent performance. Biomass and Bioenergy, 2013, vol. 53, p. 72-80.

Conference proceedings:

Rhyner U, Biollaz SMA, Regler J, Leibold H, Mai R. 1150 h Hot Gas Filter Experiment for B-IGFC Process. 19th European Biomass Conference and Exhibition. Berlin,Germany; 2011, p. 991-95

Rhyner U, Rueda O, Mai R, Leibold H, Biollaz SMA. Dynamic pressure measurements of a hot gas filter as a diagnostic tool to assess the time dependent performance. 20th European Biomass Conference and Exhibition. Milan, Italy; 2012, p. 837-43

Rhyner U, Edinger P, Schildhauer TJ, Biollaz SMA. Warm and hot gas cleaning up to 850 °C for high efficient biomass conversion processes. International Conference on Polygeneration Strategies – ICPS13. Vienna, Austria; 2013

Oral presentations:

Rhyner U, Biollaz SMA, Regler J, Leibold H, Mai R. 1150h Hot Gas Filter Experiment for B-IGFC Process. 19th European Biomass Conference and Exhibition. Berlin, Germany; 2011, p. 991-95

Rhyner U, Schildhauer TJ, Biollaz SMA. Catalytic Conversion of Tars in a Monolith in the Presence of H_2S at 750°C. 19th European Biomass Conference & Exhibition. Berlin, Germany; 2011

Rhyner U, Regler J, Mai R, Leibold H, Biollaz SMA. Heissgasfiltration eines Produktgases aus der Gegenstromvergasung für die Brennstoffzellenanwendung. Jahrestreffen der ProcessNet-Fachausschüsse "Gasreinigung" und "Hochtemperaturtechnik" 2011. Frankfurt, Germany; 2011

Rhyner U, Rueda O, Mai R, Leibold H, Biollaz SMA. Dynamic pressure measurements of a hot gas filter as a diagnostic tool to assess the time dependent performance. 20th European Biomass Conference and Exhibition. Milan, Italy; 2012, p. 837-3

Rechulski M, König C, Rhyner U, Schneebeli J, Schildhauer TJ, Biollaz SMA. Sulfur diagnostics in product gases from biomass at high and very low concentrations: A status report 2012. 20th European Biomass Conference and Exhibition. Milan, Italy; 2012

Conference posters:

Rhyner U, Edinger P, Rechulski M, Schneebeli J, Schildhauer TJ, Biollaz SMA. PSI's Diagnostics Toolbox for Online and Offline Tar Analysis: Status 2011. International Conference on Thermochemical Biomass Conversion Science, TC Biomass 2011. Chicago, USA; 2011

Rhyner U, Schildhauer TJ, Biollaz SMA. Hot gas cleaning up to 850 °C for efficient biomass conversion processes. 20th European Biomass Conference and Exhibition. Milan, Italy; 2012